Chapter 6

Particle identification

6.1 RICH

Particle identification (PID) is a fundamental requirement for LHCb. It is essential for the goals of the experiment to separate pions from kaons in selected B hadron decays. At large polar angles the momentum spectrum is softer while at small polar angles the momentum spectrum is harder; hence the particle identification system consistes of two RICH detectors to cover the full momentum range. The upstream detector, RICH 1, covers the low momentum charged particle range $\sim$1–60 GeV/c using aerogel and C_4F_{10} radiators, while the downstream detector, RICH 2, covers the high momentum range from $\sim$15 GeV/c up to and beyond 100 GeV/c using a CF_4 radiator (see figure 6.1). RICH 1 has a wide acceptance covering the full LHCb acceptance from $\pm$25 mrad to $\pm$300 mrad (horizontal) and $\pm$250 mrad (vertical) and is located upstream of the magnet to detect the low momentum particles. RICH 2 is located downstream of the magnet and has a limited angular acceptance of $\sim \pm$15 mrad to $\pm$120 mrad (horizontal) and $\pm$100 mrad (vertical) but covers the region where high momentum particles are produced. In both RICH detectors the focusing of the Cherenkov light is accomplished using a combination of spherical and flat mirrors to reflect the image out of the spectrometer acceptance. In the RICH 1 the optical layout is vertical whereas in RICH 2 is horizontal. Hybrid Photon Detectors (HPDs) are used to detect the Cherenkov photons in the wavelength range 200–600 nm. The HPDs are surrounded by external iron shields and are placed in MuMetal cylinders to permit operation in magnetic fields up to 50 mT. The RICH detector system including its electronics, monitoring, control, and the performance are described below.

6.1.1 RICH 1

The RICH 1 detector [2, 87] is located upstream of the LHCb dipole magnet, between the VELO and the Trigger Tracker, see figure 2.1. RICH 1 contains aerogel and fluorobutane (C_4F_{10}) gas radiators, providing PID from approximately $1--60$ GeV/c for particles inside the acceptance. A schematic, 3D model and photo of the RICH 1 detector is shown in figure 6.2. It is aligned to the LHCb coordinate axes and occupies the region $990 < z < 2165$ mm. The z-axis follows the beamline which is inclined at 3.6 mrad to the horizontal. The overall design has to respect the following constraints:

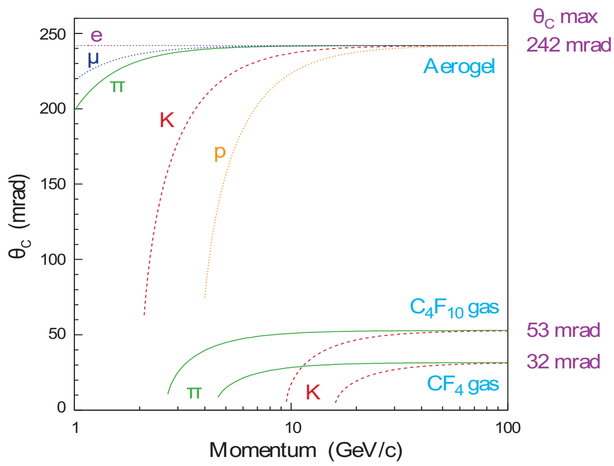

Figure 6.1: Cherenkov angle versus particle momentum for the RICH radiators.

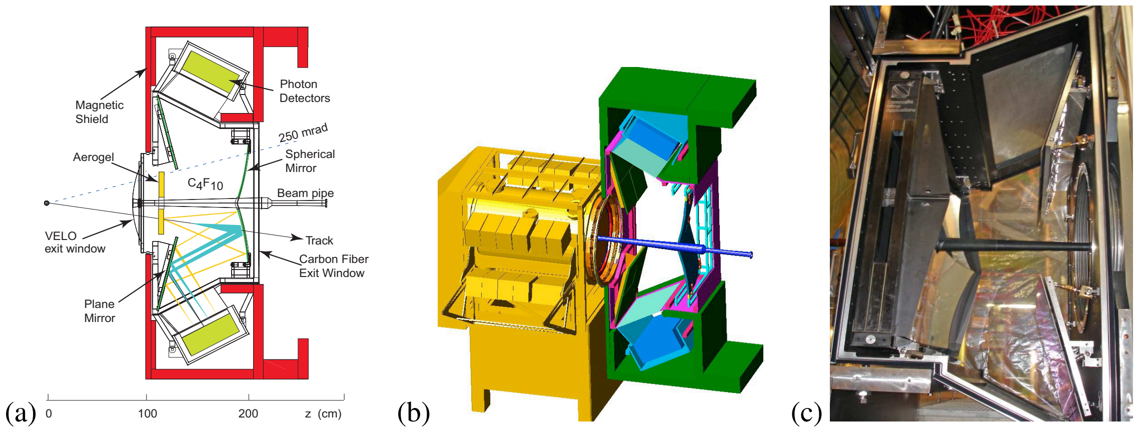

Figure 6.2: (a) Side view schematic layout of the RICH 1 detector. (b) Cut-away 3D model of the RICH 1 detector, shown attached by its gas-tight seal to the VELO tank. (c) Photo of the RICH1 gas enclosure containing the flat and spherical mirrors. Note that in (a) and (b) the interaction point is on the left, while in (c) is on the right.

- minimizing the material budget within the particle acceptance of RICH 1 calls for lightweight spherical mirrors with all other components of the optical system located outside the acceptance. The total radiation length of RICH 1, including the radiators, is $\sim$8% X_0.
- the low angle acceptance of RICH 1 is limited by the 25 mrad section of the LHCb beryllium beampipe (see figure 3.1) which passes through the detector. The installation of the beampipe and the provision of access for its bakeout have motivated several features of the RICH 1 design.
- the HPDs of the RICH detectors, described in section 6.1.5, need to be shielded from the fringe field of the LHCb dipole. Local shields of high-permeability alloy are not by themselves sufficient so large iron shield boxes are also used.

The HPDs are located outside of the LHCb acceptance, above and below the beamline, in a region where the iron shield can be accommodated. Additional planar (flat) mirrors are required to reflect the image from the tilted spherical mirrors onto the photon detector planes.

Optical system

The parameters of the RICH 1 optical layout have been optimized with the aid of simulation. Charged particle tracks, originating from the interaction point (IP) are followed through the RICH 1 radiators. Cherenkov photons are generated uniformly along the length of each track in the aerogel and gas radiators, using the appropriate refractive indices for photons within the wavelength acceptance of the HPD photocathodes. These photons are ray-traced through the optical system and their impact points on the planes of HPDs are recorded. The Cherenkov angle at emission is then reconstructed for each photon in turn, assuming that the emission point is midway along the track trajectory through the radiator. As the true emission point is randomly distributed along the track, the tilted mirror geometry causes the reconstructed Cherenkov angle to differ from its true value and results in a smearing of the reconstructed angle. The RMS of the resulting distribution is referred to as the emission point error. The RICH 1 optical system is designed such that the emission point error is not larger than other sources of finite angular resolution, such as the HPD pixel size and the chromatic dispersion of the radiator.

In addition to the emission point error, the optical layout determines the required area of coverage of the two HPD planes. The optimization procedure required close to 100% geometrical acceptance for photons emitted by the gas radiator, while a compromise dictated by the cost, and not affecting significantly the final expected performance, reduced the acceptance for the aerogel photons to 68%. The parameters of the optics are constrained by limited space and the tilt of the spherical mirrors must ensure that the flat mirrors lie outside the acceptance of the charged particle trackers. The location of the photon detector planes is also determined by the performance of the magnetic shield boxes. To avoid loss of efficiency, the HPD planes must be in a region where the field does not exceed 3 mT and be tilted to ensure that, on average, Cherenkov photons strike the HPDs at close to normal incidence.

The parameters resulting from the optimization procedure have been adopted for the engineering design of RICH 1. The spherical mirrors have radius of curvature 2700 mm with centres of curvature at $x, y, z = 0, \pm 838, -664$ mm, which define the mirror tilt. This results in an emission point error of 0.67 mrad for the gas radiator, a value that is negligible compared with other sources of error for the aerogel. The flat mirrors are tilted at an angle 0.250 rad with respect to the y-axis, with horizontal edges lying closest to the beam line located at $y, z = \pm 350, 1310$ mm. The two HPD planes are centered at $x, y, z = 0, \pm 1187, 1502$ mm and tilted at an angle 1.091 rad with respect to the y-axis. They are each covered with 7 rows of 14 HPDs, hexagonally close packed, with centres separated by 89.5 mm. This results in two detector planes of 1302 mm$\times$ 555 mm each.

Spherical mirrors

The spherical mirrors are located within the LHCb acceptance and are traversed by charged particles and photons. Glass mirrors and their associated supports would contribute about 8% X_0, so a carbon fibre reinforced polymer (CFRP) substrate, with the mirror support outside the acceptance,

2008 JINST 3 S08005

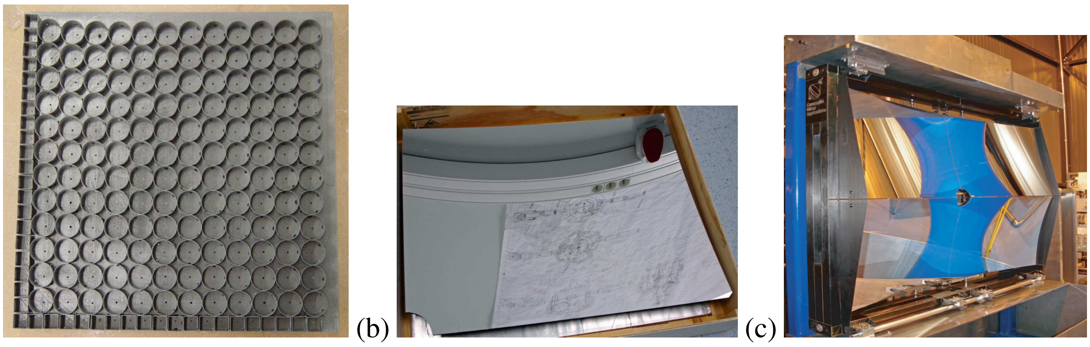
(a) (b) (c)

Figure 6.3: Photo of (a) the internal structure of the RICH 1 carbon fibre (CFRP) mirror; (b) a CFRP mirror; (c) the spherical mirror array viewed from the front, mounted onto its CFRP support frame.

is adopted to keep the material budget below 2% X_0. The two tilted spherical mirror surfaces, one above the beryllium beampipe, the other below, are each composed of two CFRP mirrors, making four mirror quadrants in total [88]. Each mirror has dimensions 830 mm$\times$ 630 mm when projected onto the $x-y$ plane. The mirror construction is from two CFRP[1] sheets, moulded over a polished glass mandrel to a spherical surface of 2700 mm radius and separated by a reinforcing matrix of CFRP cylinders, configured as shown in figure 6.3a. The box elements at the two outer edges provide stiffness for the three-point mounting brackets that attach the mirror to a CFRP frame (see figure 6.3c). Each mirror has a circular cut-out of radius 62.5 mm to provide a nominal 10 mm clearance from the beampipe (see figure 6.3b). The overall structure has an areal density of 6 kg m^{-2}, thus contributing about 1.5% X_0 to the material budget of RICH 1.

The geometrical quality of a spherical mirror is characterized by the variation in the mean radius R of each mirror and the parameter D_0, the diameter of the image in which is contained 95% of the light from a point source placed at the centre of curvature. Provided $D_0 < 2.5$ mm and $\Delta R/R < 1\%$, the geometry of the mirrors provides a negligible contribution to the reconstructed Cherenkov angle precision. The manufacturing and subsequent quality assurance ensures that the mirrors satisfy these specifications.

The mirror assembly is made from two CFRP half frames. Each carries an upper and a lower quadrant. The half frames are divided in this way to allow insertion into the RICH 1 gas enclosure (described further on in this section) from either side of the beampipe, following which the frames are clamped to form a rigid structure around the periphery. The CFRP frame is mounted on rails and supported by an optical alignment rig. Upper and lower mirror pairs are aligned to a common centre of curvature and the CFRP frame is surveyed. This frame is then installed in the gas enclosure using an identical rail system, where the frame can again be surveyed and adjusted if necessary. Simulations [89] have shown that provided all mirror segments are aligned to a precision of about 1 mrad, the alignment can be further corrected using data from reconstructed Cherenkov ring images.

The mirrors are coated using a deposition of Al(80nm)+MgF_2(160nm). The reflectivity that can be achieved on the CFRP substrate is the same as that on a glass support, as shown by curve V in figure 6.6 and described in section 6.1.4.

[1] Fibres: Toray M46J; Matrix: Bryte Technologies, EX-1515 cyanate ester resin; Manufacturer: Composite Mirror Applications Inc.,Tucson, USA.

2008 JINST 3 S08005

Flat mirrors

The flat mirrors are assembled into two planes, one above and one below the beamline. They are located outside of the acceptance, so glass substrates can be used. Each plane comprises eight rectangular mirrors with dimensions 380 mm $\times$ 347.5 mm, fabricated using 6.5 mm thick Simax[2] glass. As for the spherical mirrors, the flat mirror geometry is characterized through the parameters R and D_0. All mirrors have $|R| > 600$ m and $D_0 < 2.5$ mm. Assuming the deviations from surface sphericity are randomly distributed, this value of D_0 contributes < 0.2 mrad to the single photon Cherenkov angle precision. The mirrors are coated using the same ($Al+SiO_2+HfO_2$) process used for the RICH 2 mirrors (section 6.1.2). Each of the eight mirror segments is connected to a three-point adjustment system via a polycarbonate flange, described in section 6.1.2. The adjustment mechanism is bolted to a rigid plate that is suspended from rails. The eight mirror segments are adjusted in angle to form a single plane, then the angle of this plane is set using the optical alignment rig. Following alignment and survey, the plate is mounted on an identical rail system attached to the upstream wall of the RICH 1 gas enclosure, where the angle can again be surveyed and adjusted if necessary.

RICH 1 structure

The total weight of the RICH 1 detector is about 16 tons, mainly due to the magnetic shielding boxes. The lower box is fixed to the LHCb cavern floor and supports the gas enclosure and the lower photon detector assembly. The upper box is fixed to the cavern wall and supports the upper photon detector assembly.

Gas enclosure

The functions of the gas enclosure are to contain the C_4F_{10} gas radiator and to provide a light-tight and mechanically stable platform for all optical components. The gas enclosure must sustain a ± 300 Pa pressure differential between the C_4F_{10} gas and the outside atmospheric environment. It is essentially a six-sided box machined from 30 mm thick aluminium alloy tooling plate[3] that is welded at the edges to form a 600 kg structure with a total volume of about 3.5 m^3 (see figure 6.2c). All six faces have apertures. The boundaries of the upstream and downstream apertures are clear of the RICH 1 acceptance region. The upstream face attaches to a 300 μm thick stainless steel bellows that provides a gas-tight, mechanically compliant (axial stiffness 37 Nmm^{-1}) seal to the downstream face of the VELO vacuum tank. The downstream face is closed by a low-mass exit window that is sealed to a flange on the beryllium beampipe using a 1 mm thick opaque moulded silicone[4] diaphragm. The exit window is manufactured from a sandwich of two 0.5 mm thick CFRP skins separated by 16 mm thick polymethacrylimid foam. Its radiation length corresponds to 0.6% X_0. The choice of material thickness for the exit window is a compromise between material budget and the deflection (± 4 mm) due to the ± 300 Pa pressure differential that will be maintained by the C_4F_{10} gas system.

[2] 3.3 borosilicate glass by SKLÁRNY KAVALIER, a.s. COMPAS, Kinskeho 703, CZ-51101 Turnov.
[3] C250, cast using type 5083 alloy.
[4] Dow Corning Sylgard 186, with 5% black pigment added.

The side faces of the gas enclosure are fully open to maximize access for installation of the optical components and to the beampipe. They are closed by 10 mm thick aluminium door panels. With the doors bolted in place the maximum displacement of any part (except the exit window) of the gas enclosure due to variations of gas pressure is less than 150 μm. Apertures above and below the beamline are sealed using windows that allow Cherenkov light to reach the HPDs. These windows are 8 mm thick quartz[5] with dimensions 1360 mm$\times$ 574 mm, fabricated from two equal-size panes, glued together along one edge. The quartz windows are coated with MgF_2 to reduce surface reflection losses from 8% to 4%.

Magnetic shield boxes

The HPDs are located in the upstream fringe field of the LHCb dipole of about 60 mT. They operate at full efficiency at a B-field up to a maximum of 3 mT. So the shield boxes need to attenuate the external field by a factor of at least 20, they need to be large enough to accommodate the HPDs and their associated readout, and they must not obstruct Cherenkov light falling on the HPD photocathodes. In addition, the bending of charged particles in the region between the VELO and the TT station provides a momentum measurement that is important for the trigger. Therefore, in designing the magnetic shields, due consideration was given to maintaining the field integral in this region.

A schematic of the shielding structure is shown in figure 6.2. The magnetic design was optimized using the OPERA/TOSCA[6] finite element modelling software. It is assembled from 50 and 100 mm thick high purity ARMCO[7] plates. Measurements made with the shields in place and the LHCb dipole at full field indicate that the maximum B-field at the HPD plane is 2.4 mT, while the field integral between the IP ($z = 0$) and the TT ($z = 2500$ mm) is 0.12 Tm. Further details of the modelling and measurements are reported in reference [90]. The overall dimensions (x, y, z) of the shield are 1950 mm$\times$ 4000 mm$\times$1175 mm. The weight of each box is about 75 kN and the magnetic forces at full field are about 50 kN. The rigidity of the shielding structure and mounting ensures that any displacement of the HPD assembly is less than 0.5 mm when the LHCb magnet current is switched on.

6.1.2 RICH 2

The RICH 2 detector [91, 92] is located between the last tracking station and the first muon station, see figure 2.1. It contains a CF_4 gas radiator, providing PID from approximately 15 to $\geq$ 100 GeV/c for particles within the reduced polar angle acceptance of $\pm$120 mrad (horizontal) and $\pm$100 mrad (vertical). Two schematics and a photograph of the RICH 2 detector are shown in figure 6.4. It is aligned vertically, with its front face positioned at 9500 mm from the interaction point and with a depth of 2332 mm. The overall design had to comply with the following constraints:

- the supporting structures and the photon detectors need to be placed outside the acceptance of the spectrometer and the HPDs are located left and right of the beamline where the iron

[5]HERAEUS Suprasil 2B.
[6]Vector Fields plc, Oxford, UK.
[7]ARMCO - Stabilized iron; C$\leq$ 0.01%, S= 0.01%, Mn$\leq$ 0.06%, Si: traces, P= 0.01%.

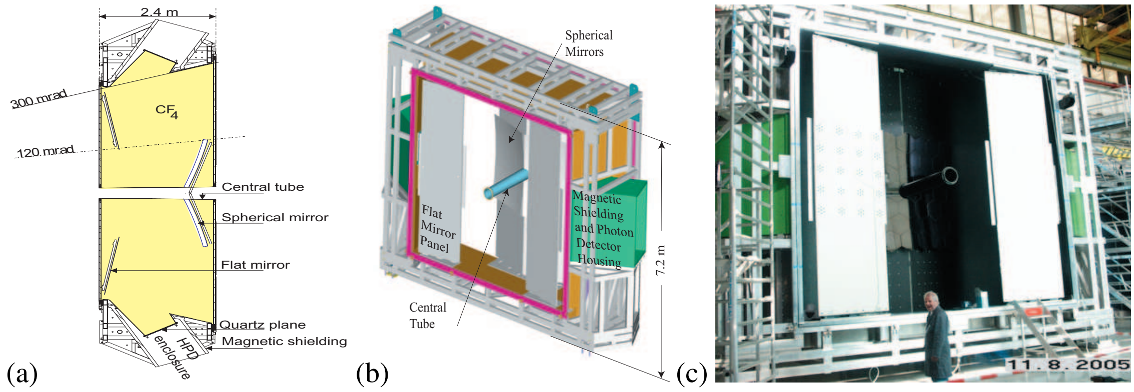

Figure 6.4: (a) Top view schematic of the RICH 2 detector. (b) A schematic layout of the RICH 2 detector. (c) A photograph of RICH 2 with the entrance window removed.

shielding is accommodated. To shorten the overall length of the detector, the reflected images from tilted spherical mirrors are reflected by flat secondary mirrors onto the detector planes. The requirement that the photon detectors are situated outside the full LHCb acceptance defines the lateral dimensions of the detector. The total radiation length of RICH 2, including the gas radiator, is about 0.15 X_0.

- the lower angular acceptance of the RICH 2 detector, 15 mrad, is limited by the necessary clearance of 45 mm around the beampipe. This distance is required to accommodate the heating jacket and thermal insulation which is required for the bakeout of the vacuum chamber (chapter 3). To gain mechanical stability of RICH 2 and minimize the material in the acceptance of the spectrometer, the detector does not split in two halves along the $x = 0$ plane.

- as for RICH 1, the HPDs are located in large iron boxes in order to be shielded from the fringe field of the LHCb dipole.

Optical system

The final adjustment of the optical layout of RICH 2 has been performed with the aid of simulation, in a similar way to that described in section 6.1.1. This involves defining the position and radius of curvature of the two spherical mirror planes, the position of the two flat mirror planes, and the position of the two photon detector planes. The smearing of the reconstructed Cherenkov angle distribution provides a measure of the quality of the focusing. The RMS of the emission-point error should be small compared to the other contributions to the Cherenkov angle resolution such as the pixelization of the photon detectors and the chromatic dispersion of the radiator. The latter effect is the limiting factor for the resolution in RICH 2, and corresponds to an uncertainty of 0.42 mrad on the Cherenkov angle per photon [91]. The optical elements of RICH 2 must therefore be set such that the emission-point error is small compared to this value.

The parameters resulting from the optimization procedure have been adopted for the engineering design of RICH 2. The spherical mirrors have radius of curvature 8600 mm with centres of

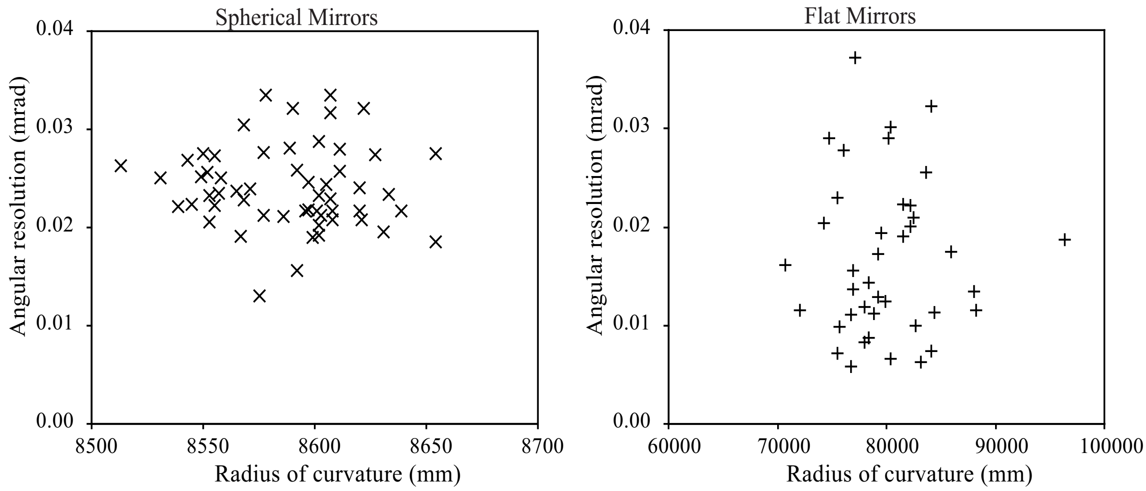

Figure 6.5: Angular precision as a function of radius of curvature for the spherical and the flat mirrors in RICH 2. The angular precision of a mirror is defined as the RMS angular deviation of the normal to the mirror surface at the given point from the radius of curvature R, and is related to D_0 by the expression $D_0/8R$, under the assumption that the light distribution of the spot is gaussian.

curvature at $x,y,z = \pm 3270, 0, 3291$ mm which defines the mirror tilt. The flat mirrors are tilted at an angle 0.185 rad with respect to the x-axis, with vertical edges lying closest to the beam line located at $x,z = \pm 1234, 9880$ mm. The two HPD planes are centered at $x,y,z = \pm 3892, 0, 10761$ mm and tilted at an angle 1.065 rad with respect to the x-axis. They are each covered with 9 rows of 16 HPDs, hexagonally close packed, with centres separated by 89.5 mm. This results in two detector planes of 710 mm$\times$ 1477 mm each.

Spherical and flat mirrors

There are two spherical mirror surfaces and two planes of flat mirrors, assembled either side of the beamline. The mirror substrates are made from 6 mm thick Simax glass; the development of these mirrors is described elsewhere [93–96]. The spherical mirrors are composed of hexagonal mirror elements with a circumscribed diameter of 510 mm, and there are 26 mirrors (or half-mirrors) in each plane. The flat mirror surfaces are formed from 20 rectangular mirror segments in each plane, each $410 \times 380\,\text{mm}^2$ in area. The greatest challenge for the manufacturers was the stability of the thin flat mirror substrates, leading to highly astigmatic or edge deformations. We have therefore chosen to use as flat mirrors, substrates with a finite but large radius of curvature, of about 80 m. The measured properties of the mirrors are shown in figure 6.5. The impact on the resolution is discussed in section 6.1.8.

Mirror support and alignment

The mirror supports are the crucial elements that will allow the construction of a near perfect reflective surface from the individual mirror segments; the initial alignments of the mirrors must be better than 1 mrad to have a negligible effect on the Cherenkov ring reconstruction [89]. Each mirror substrate is connected to a three-point adjustment system via polycarbonate flanges and rods [92]. The adjustment mechanism is attached to large aluminium *sandwich* panels which are fastened to the top and the bottom of the superstructure. These panels are made from two 1 mm thick aluminium skins separated by 28 mm aluminium honeycomb,[8] corresponding to $\sim 4\%$ X_0. This choice of material is again a trade-off between a long-term stability requirement, reduction of the radiation length and fluorocarbon compatibility. The mirror-support system has been tested in the laboratory for more than one year and, after an initial relaxation period, it is stable to within 100 μrad [94, 96]. The fluctuations are mainly governed by temperature variations.

The mirrors have been installed and aligned in a three-step process [97]. First, all of the spherical mirror segments were aligned to within 50 μrad of their common focal point. Then a few flat mirrors were aligned together with the coupled spherical mirrors. The final step was to align the rest of the flat mirrors with respect to these. The total error on the alignment is of the order of 100 μrad. Even though the fully equipped RICH 2 detector was transported by road from the laboratory to the experimental area, no change of the alignment larger than 300 μrad of any mirror has been observed.

RICH 2 structure

The total weight of the RICH 2 detector is about 30 tons, a large fraction of which, $\sim$ 12 tons, is the overall magnetic shielding structure. The superstructure provides the mechanically stable environment for the optical system, the overall magnetic shielding containing the photon detectors, and a lightweight configuration for the radiator gas enclosure. It is a rectangular box-shaped structure made from welded aluminium alloy rectangular hollow box sections. The deflection of the top of the structure is measured to be < 100 μm under the influence of the magnetic load. The RICH 2 detector is placed and surveyed into position as one unit on the beam line and, after this, the beampipe is installed.

Gas enclosure

The total volume of the gas enclosure is about 95 m^3, defined by the superstructure, the entrance and the exit windows. The entrance window, constituting a radiation length of 1.0% X_0, is a low mass composite panel made from two 1 mm thick carbon fibre reinforced epoxy skins, separated by 28 mm thick polymethacrylimide (PMI) foam. The exit window, constituting a radiation length of 2.5% X_0, is similarly made from two 1 mm thick aluminium skins separated by 30 mm PMI foam. The choice of core thicknesses and skin materials is a compromise between radiation length and deflection due to hydrostatic pressure exerted by the Cherenkov gas. The latter will be controlled to within $^{+200}_{-100}$ Pa at the top of the detector. The two windows are clamped and sealed onto the superstructure and are connected to each other by a castellated central tube running coaxial to the vacuum chamber; the tube is made from 2 mm thick carbon fibre epoxy composite. The diameter of the tube at the entrance window is 284.5 mm and 350.5 mm at the exit.

The two planes of photon detectors are separated from the Cherenkov gas by quartz windows on each side. Each window is made from three quartz panes glued together. Each quartz pane

[8]Euro-Composites S.A, Zone Industrielle - B.P. 24, 6401 Echternach.

is 740 mm by 1480 mm and 5 mm thick, with the light opening being 720 mm by 1460 mm. The quartz plates have the same antireflective coating as for RICH 1 (section 6.1.1).

Magnetic shielding structure

The RICH 2 detector is positioned almost halfway between the 1600 ton iron yoke of the dipole and the massive ferromagnetic structure of the hadron calorimeter, shown in figure 2.1. The maximum stray field in the region where the photon detectors are located is more than 15 mT and is rapidly varying in all directions [98]. The magnetic shield boxes, which are bolted onto both sides of the RICH 2 structure, must provide a mechanically stable and light tight environment for the photon detectors and attenuate the magnetic stray field by a factor of ≥ 15. The shielding, shown in figure 6.4, is a trapezoidal structure made from 60 mm thick ARMCO iron plates. The residual magnetic field measured at the position of the photon detector plane is between 0.2 and 0.6 mT, to be compared to the simulated value of ≤ 0.4 mT.

6.1.3 Radiators

Aerogel is the ideal radiator to cover the very difficult range of refractive indices between gas and liquid. Silica aerogel is a colloidal form of quartz, solid but with an extremely low density. Its refractive index is tuneable in the range 1.01–1.10, and is ideal for the identification of particles with momentum of a few GeV/c. Aerogel has a long-established use in threshold Cherenkov counters. The development of high quality very clear samples [99] has allowed its use in RICH detectors. The dominant cause of photon loss within aerogel is Rayleigh scattering; this leads to the transmission of light with wavelength λ through a block of thickness L being proportional to e^{-CL/λ^4}, where the clarity coefficient, C, characterizes the transparency of the sample. Large hygroscopic silica aerogel [99] tiles of dimension $20.0 \times 20.0 \times 5.1\,\mathrm{cm}^3$ have been produced and tested for the LHCb experiment [100]. The refractive index is 1.030 at λ=400 nm and the clarity is below $C = 0.0054\ \mu\mathrm{m}^4/\mathrm{cm}$. The effect of scattering in the aerogel dominates at high energy, so a thin (0.30 mm) window of glass is placed after the aerogel to absorb the photons with $E_\gamma > 3.5$ eV. This serves to reduce the chromatic aberration.

For a track passing through 5 cm of aerogel with $n = 1.03$, the resulting number of detected photoelectrons in a saturated ring (β=1) is expected to be ~6.5, calculated by MonteCarlo considering the detailed geometrical setup of the optics of RICH 1 and the wavelength response of the photon detectors. The MonteCarlo was found to describe reasonably well the number of photoelectrons measured in a test beam [100]. Tests have shown [101] that the optical properties will not degrade significantly over the timescale of the LHCb experiment. The aerogel is stable against intense irradiation and shows no significant change in transparency once tested after an accumulated fluence of up to 5.5 x $10^{13}/\mathrm{cm}^2$ of neutrons or protons, nor after a γ dose of 2.5×10^5 Gy. It is sensitive to water vapour absorption, but its transparency can be restored after a bakeout of the tiles. The volume of aerogel required is modest, $\sim 30\ \ell$, so its replacement, if required, would be relatively straightforward. The refractive index is fairly uniform across a tile, despite the large transverse dimension and thickness. The spread has been measured [102] to be $\sigma_{n-1}/(n-1) \sim 0.76\%$. In RICH 1 the aerogel sits in the C_4F_{10} gas radiator. Tests have shown that C_4F_{10} does not significantly degrade the aerogel performance [103].

The fluorocarbon gases C_4F_{10} (RICH 1) and CF_4 (RICH 2) were chosen because their refractive indices are well matched to the momentum spectrum of particles from B decays at LHCb and because they have a low chromatic dispersion. The refractive indices at 0°C and 101325 Pa are parameterized by:

$$C_4F_{10} : (n-1) \times 10^6 = 0.25324/(73.7^{-2} - \lambda^{-2})$$

and

$$CF_4 : (n-1) \times 10^6 = 0.12489/(61.8^{-2} - \lambda^{-2})$$

where the photon wavelength λ is in nm [104]. For C_4F_{10}, n=1.0014 and for CF_4, n=1.0005 at $\lambda = 400\,\mathrm{nm}$. The effective radiator lengths are about 95 cm in C_4F_{10} and 180 cm in CF_4. The estimated photoelectron yield is $\sim$30 and $\sim$22 respectively for charged $\beta \approx 1$ particles.

The gas radiators are operated slightly above atmospheric pressure $\lesssim$ 50 Pa (measured at the top of the gas vessel) and at ambient temperature. Pressure and temperature are recorded in order to compensate variations in the refractive index (section 6.1.7). These fluorocarbons are transparent well below 150 nm; CO_2 is used as a pressure balancing gas which itself is transparent down to 180 nm [105]. Since the quantum efficiency of the HPDs is zero below 190 nm (section 6.1.5), air contamination does not significantly affect the photon yield. O_2 and H_2O contamination are however kept low at about 100 ppm, mainly due to possible radiation-induced formation of HF. The CO_2 fraction is kept constant at $\sim$1%.

6.1.4 Mirror reflectivity studies

Several reflectivity coatings are available for RICH mirrors; the choice depends on the Cherenkov photon spectrum, the mean angle of incidence, the long term stability and compatibility to fluorocarbons. Seven different coatings have been tested [93, 106] and the reflectivity measured with a spectrophotometer at an incidence angle of 30°, close to the average angle with which the photons will impinge on the RICH 2 mirrors. The results are shown in figure 6.6. The reflectivity coatings for the RICH 1 mirrors have been optimized for the the different mean angles of incidence, i.e. 25° for the spherical mirrors and 45° for the flat mirrors.

Simulation studies have been performed by convoluting the reflectivity data with the quantum efficiency of the photon detectors, the Cherenkov photon energy spectra and the transmittance of the CF_4 radiator in RICH 2. The results of the simulation, in terms of the relative number of detected photons, are summarised in table 6.1.

The reflectivity of the two coatings with a layer of hafnium oxide (HfO_2) is very high in the near UV (curve I and II in figure 6.6), where the quantum efficiency of the photon detector is peaked. The simulation shows that good matching, taking into account the two reflections on spherical and flat mirrors, leads to a detected photon yield 5% higher for this coating compared to other UV extended coatings with magnesium fluoride (MgF_2) as the surface layer. Magnesium fluoride coatings have been successfully used in RICH detectors with C_4F_{10} and C_5F_{12} gas radiators in the DELPHI [107] and COMPASS [108] experiments, and hafnium oxide coatings have been successfully tested in C_6F_{14} vapour. Hafnium oxide also provides a very hard and chemically inert protective layer for the mirrors. For these reasons the Al + SiO_2 + HfO_2 coating was chosen for all RICH 1 and RICH 2 glass mirrors. SiO_2 is used for the middle layer of the multi-layer coating, and not MgF_2, for technical reasons.

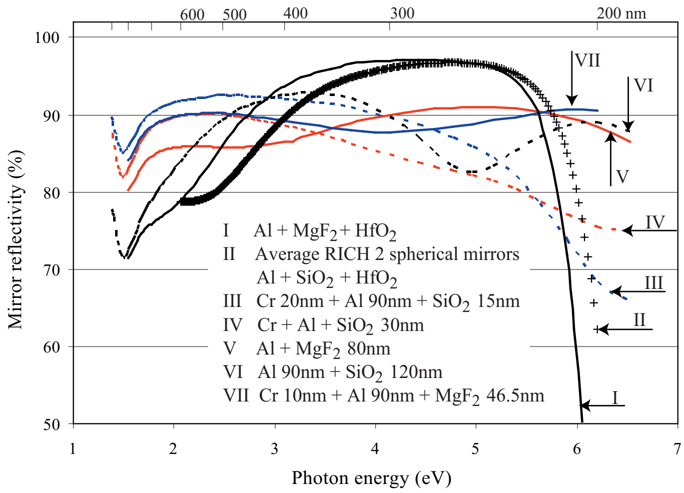

Figure 6.6: Reflectivity of several mirror coatings on glass as a function of the photon energy. The angle of incidence is 30°.

Table 6.1: Relative number of detected photons simulated in RICH 2 for different mirror coatings. The values are normalised to the highest photoelectron yield, set to 1.

Coating	Photoelectron yield
Cr + Al + SiO_2 (30 nm)	0.865
Al + SiO_2	0.945
Cr + Al + MgF_2	0.947
Al + MgF_2	0.960
Cr + Al + SiO_2 (15 nm)	0.960
Al + SiO_2 + HfO_2	1
Al + MgF_2 + HfO_2	1.00

6.1.5 Photon Detectors

Pixel Hybrid Photon Detector

The RICH detectors utilize Hybrid Photon Detectors (HPDs) to measure the spatial positions of emitted Cherenkov photons. The HPD is a vacuum photon detector in which a photoelectron, released from the conversion in a photocathode of an incident photon, is accelerated by an applied high voltage of typically 10 to 20 kV onto a reverse-biased silicon detector. During the photoelectron energy dissipation process in silicon, electron-hole pairs are created at an average yield of one for every 3.6 eV of deposited energy. Carefully-designed readout electronics and interconnects to the silicon detector result in very high efficiency at detecting single photoelectrons.

A dedicated pixel-HPD has been developed by LHCb, in close collaboration with industry [109]. The specific RICH requirements are a large area coverage ($\sim$3.5 m^2) with high active-to-total area ratio after close-packing (64%), high granularity (2.5$\times$2.5 mm^2 at the photocathode) and high speed (25 ns timing resolution). The pixel-HPD is shown in figure 6.7. It is

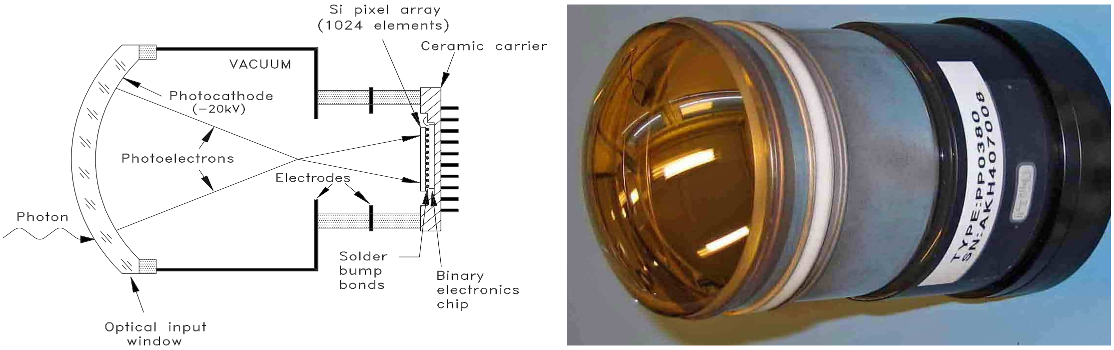

Figure 6.7: Left: a schematic and right: a photograph of the pixel-HPD.

based on an electrostatically focussed tube design with a tetrode structure, de-magnifying by a factor of $\sim$5 the photocathode image onto a small silicon detector array. The silicon detector is segmented into 1024 pixels, each 500 μm$\times$500 μm in size and arranged as a matrix of 32 rows and 32 columns. This leads to the required pixel size at the HPD entrance window of 2.5$\times$2.5 mm^2. The nominal operating voltage of the HPD is -20 kV, corresponding to $\sim$5000 electron-hole pairs released in the silicon.

The silicon pixel detector array is bump-bonded to a binary readout chip (section 6.1.6). This flip-chip assembly is mounted and wire-bonded onto a Pin Grid Array (PGA) ceramic carrier, forming the HPD anode. Since all anode parts are encapsulated in vacuum, they must be compatible with the vacuum tube technologies, and must stand high (300°C) bakeout temperatures. In particular, a specific fine-pitch bump-bonding process has been developed for this application.[9] The HPD entrance window is fabricated from quartz and forms a spherical surface, with 7 mm thickness and 55 mm inner radius of curvature. The photocathode is of the *thin-S20* multi-alkali type, deposited on the quartz inner surface. Normally-incident Cherenkov photons to the HPD plane can be detected over an active diameter of 75 mm and, since the overall tube diameter is 83 mm, the intrinsic tube active area fraction is $(75/83)^2$=0.817. A total of 484 tubes (196 for RICH1 and 288 for RICH2) are required to cover the four RICH photon detection surfaces.

The demagnification by 5 of the photoelectron image is achieved by biasing the photocathode at -20 kV, the first electrode at -19.7 kV and the second electrode at -16.4 kV. The RMS values for the point spread function (PSF) at the pixel array are constant over the tube radius and equal to 80 μm for red light and 180 μm for blue-near UV light, in the absence of magnetic field.

HPD test results

The HPDs have been fabricated in industry[10] and were then qualified at two test facilities to determine their efficiency and optimum working parameters, before installation at CERN. Each HPD in turn was placed in a light-tight box, illuminated with an LED of wavelength 470 nm, and read out by custom electronics. A selection of test results is presented below. Measurements of the quantum efficiencies (QEs) were carried out after manufacture at Photonis-DEP. Measurements were then

[9] VTT, Finland.
[10] Photonis-DEP, Roden, Netherlands.

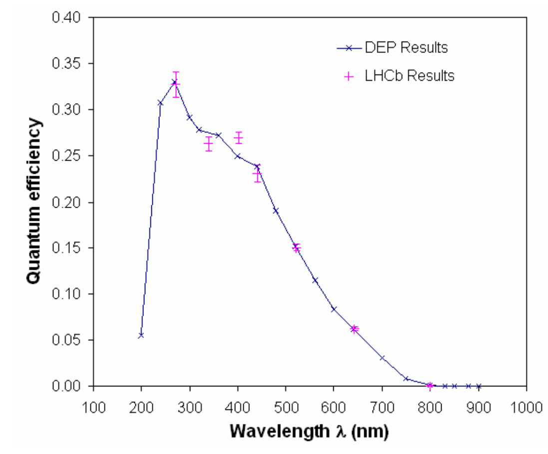

Figure 6.8: QE measurement for one of the best HPD.

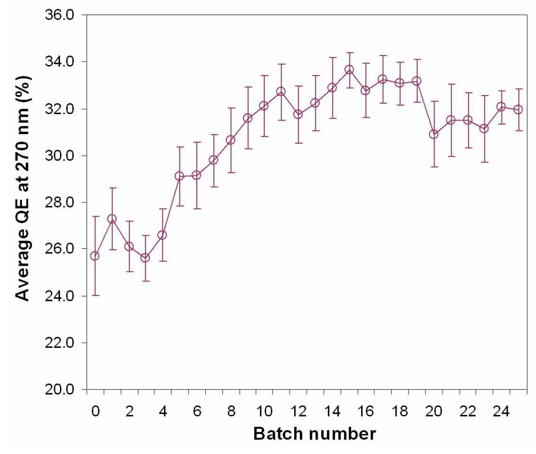

Figure 6.9: The average QE(%) at 270 nm versus the HPD batch number.

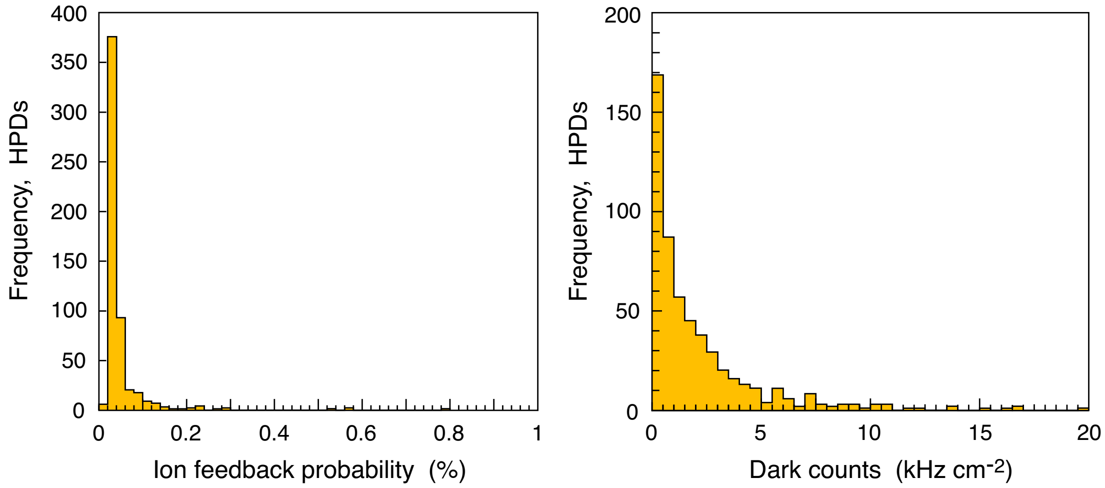

Figure 6.10: Distributions of the ion-feedback rate (left) and of the dark-count rates (right).

repeated at the test facilities for a subsample of 10% of the HPDs, using a calibrated photodiode and a quartz-tungsten halogen lamp. The QE curve for one of the best tubes is shown in figure 6.8. The average QE value per HPD batch number and the running average QE value are shown in figure 6.9 for all HPDs (484 tubes plus 66 spares). The QE curves show an average maximum of 31% at 270 nm, considerably above the specification minimum of 20%.

The vacuum quality in the HPD tube is determined by measuring ion feedback. During the acceleration process, photoelectrons may hit residual gas atoms, producing ions. These drift to the photocathode, releasing 10–40 electrons which are detected 200–300 ns after the primary photon signal. Figure 6.10 shows that the ion feedback rate is well below the specification maximum of 1%, indicating that the vacuum quality is excellent.

An important quality factor of an HPD is low dark-count rate, the main sources being thermionic electron emission at the photocathode, electrostatic field emission and any resulting

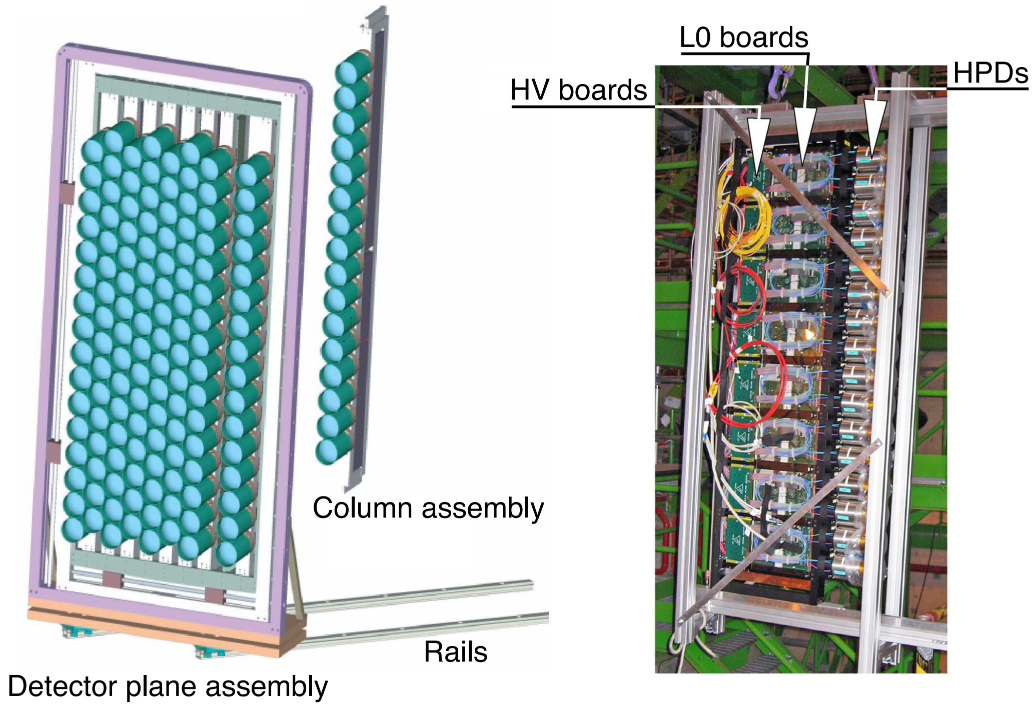

Figure 6.11: Left: the RICH 2 column mounting scheme and right: a photograph of a column.

ion feedback. Figure 6.10 shows the measured dark-count rates in the sample of HPDs in a run with the LEDs off. Dark-count rates are typically below the specification value, 5 kHz/cm^2 with respect to the photocathode area, which in turn is $\sim 10^3$ less than the maximum occupancy expected in the RICH detectors.

HPD testing was carried out at a rate of 30–40 HPDs per month. A total of 97% have been found to meet or exceed the design criteria in key areas.

Photon Detector integration

The HPDs are grouped in four detection planes (two for RICH1 and two for RICH2) and positioned on a hexagonal lattice. The hexagonal close-packing factor is 0.907. Each tube is completely surrounded by a 1 mm thick cylindrical magnetic shield which protects against stray external B-fields up to 5 mT (the maximum field value within the RICH 1 magnetic shielding has been measured to be 2.4 mT, see section 6.1.1). A tube-to-tube pitch of 89.5 mm in both RICH detectors has been chosen, resulting in a packing factor of $(75/89.5)^2 \times 0.907 = 0.64$. The HPDs are mounted on columns which are installed in the magnetic shielding boxes of the two RICH detectors. There are 2×7 columns of HPDs in RICH 1 with 14 HPDs per column and 2×9 columns in RICH 2 with 16 HPDs per column. Figure 6.11 illustrates the column mounting scheme for RICH 2. The column also contains front-end electronics boards (one per pair of HPDs), power supply distribution, cabling and active cooling, all within one mechanical module. The electronics boards and power distribution are described in section 6.1.6.

6.1.6 Electronics

The RICH electronics system reads out data from the HPDs (about 5×10^5 channels) and conforms to the general electronics architecture of LHCb (see section 2.2). The electronics system is divided into so-called Level-0 (L0) and Level-1 (L1) regions. The L0 electronics are all located on-detector where they will be exposed to radiation and must therefore contain only radiation-qualified components. The L1 electronics modules are housed in the counting house behind the radiation-shield wall and hence are not required to be radiation tolerant.

Level-0 electronics

The L0 electronics comprises the pixel chip, ZIFs/kaptons, L0 board and LV/HV distribution, and is described below.

Pixel Readout Chip: At the beginning of the electronics readout chain is the LHCBPIX1 pixel chip [110] that forms part of the anode assembly of the HPD (section 6.1.5). The chip has been designed in a commercial 0.25 μm CMOS process using special layout techniques to enhance its resistance to radiation. The chip is connected to a silicon pixel sensor by an array of solder bump-bonds, one per channel. Each pixel measures 62.5 μm by 500 μm and 8192 pixels are arranged as a matrix of 32 columns by 256 rows. Circuitry on the chip logically ORes eight adjacent pixels, thus transforming the matrix into 1024 channels of 32 by 32, each of size 500 μm by 500 μm. Signals from the silicon sensor are amplified, shaped and then compared with a global threshold. Hits are buffered for the duration of the Level-0 trigger latency and triggered events are then read out by way of a 16-deep multi-event FIFO buffer. The 32 columns are read out in parallel. The analog behaviour of the chip is crucial for a good photodetection efficiency, in particular low noise and uniform threshold. Measured values are well within the HPD specifications, with typically 160 electrons noise, compared to a signal of 5000 electrons, and a mean threshold of 1200 electrons with RMS spread of 100 electrons.

ZIFs and Kaptons: Signals to and from the HPD pass through the pins of the ceramic pin-grid-array carrier. This is plugged into a 321-pin Zero-Insertion-Force (ZIF) connector mounted on a small circuit board. The board also contains passive components for filtering and line-termination. Signals are then transmitted on two Kapton cables which also carry the low-voltage power to the HPD. These Kaptons allow mechanical flexibility between the mounting of the HPDs and the other Level-0 components.

L0 Board: The L0 board [111] acts as an interface between the HPDs and the ECS (Experiment Control System), TFC (Timing and Fast Control) and data transmission systems. This interfacing is implemented in the Pixel Interface (PINT). The antifuse gate array, ACTEL AX1000, was chosen for its tolerance to single event effects (single event latch-up and single event upset). Its main tasks are to receive data from two HPDs, add headers containing event information and data-integrity checks, and transfer events to the data transmission system. A total of 242 L0 boards are used in the RICH detectors. A photograph of a single board is shown in figure 6.12. The tolerance of the PINT to single event effects was verified by irradiation tests to simulate the expected dose in the LHCb environment. The measured rate of single event upset (SEU) was negligible, no cases of latch-up were observed and chips survived many times the expected dose of ionising radi-

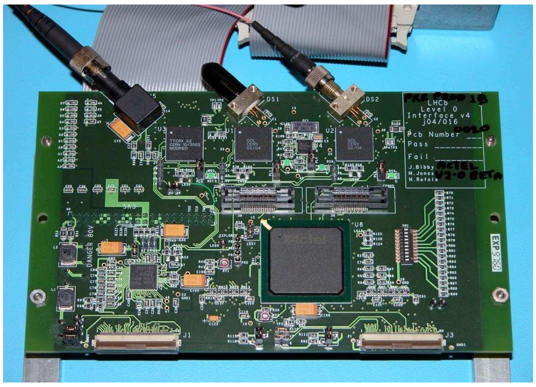

Figure 6.12: A photograph of the L0 board. The optical receiver and transmitters are visible at the top. The PINT gate array is in the centre of the board.

ation. All other components on the L0 board have been designed in radiation-hardened or tolerant technologies already qualified to levels far in excess of the RICH environment.

The optical data transmission consists of Gigabit Optical Link (GOL) chips [112] and Vertical Cavity Surface Emitting Lasers (VCSEL). The GOLs serialise the data into a 1.6 Gbit/s bit stream using 8 b/10 b encoding and the VCSELs convert this into an optical signal of 850 nm wavelength. Two output fibres, one per HPD, transmit the data from each L0 board. At a 1MHz trigger rate, the aggregate output data rate from the RICH photon detectors is in the region of 500 Gbit/s distributed over 484 optical fibres. Also on the board is a TTCrx [113] which generates the 40 MHz clock and trigger and calibration signals. The input to the TTCrx arrives on fibres connected to the global TFC system. Finally, a chip known as the Analog-Pilot generates reference voltages required by the HPDs and digitizes monitoring signals such as the temperature of the board as measured by PT1000 sensors.

LV/HV Distribution: The low voltages required by the HPDs and the L0 boards are provided by the LV distribution system. These voltages are generated locally using radiation-tolerant linear voltage regulators mounted on the LV boards. Each LV board can power two L0 boards independently, and four LV boards are daisy-chained together in an HPD column. The top-most contains a SPECS slave module [41] which provides the interface for the configuration of the HPDs and L0 boards in that column. The SPECS interface is also used for switching on and off the voltage regulators, thus allowing careful control of the powering of the column.

The high voltages for the HPDs are provided by the HV distribution system [114]. As shown in figure 6.13b, the three voltages are derived from a 20 kV input by means of a resistive divider, one per half-column, and short circuit protection is provided by 1 Gohm resistors in series with each HPD voltage line. Various measures have been taken to minimise the risk of discharge or breakdown. The bare PCB of the HV cards is machined to introduce cuts around critical points which are then filled with dielectric gel to improve insulation. After component mounting and cabling, the entire assembly is encapsulated in silicone rubber. A photograph of a completed board is shown in figure 6.13. A total of 242 boards are used to equip the RICH detectors.

Figure 6.14 shows a photograph of all front-end electronics components mounted on a RICH HPD column. On the left are the Kapton cables shown plugged into the L0 boards, then comes a

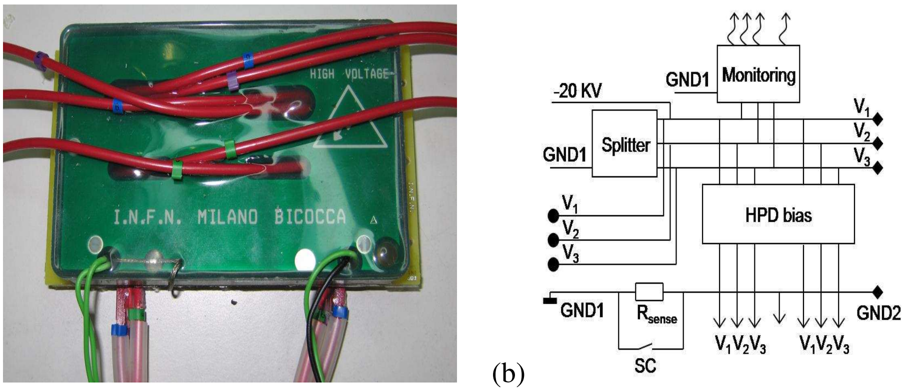

Figure 6.13: A photograph (a) and the scheme (b) of an HV board. Around the board is the silicone coating.

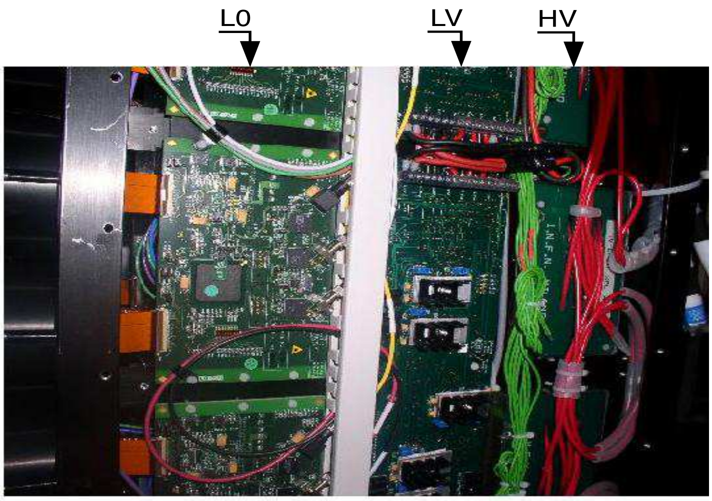

Figure 6.14: A photograph of L0, LV and HV boards mounted on a RICH HPD column.

cable tray to carry the optical fibres. Next comes the LV board which has heat sinks mounted on the surface of the voltage regulators. At the far right are the HV boards.

Level-1 electronics

The RICH L1 electronics, located off-detector in the counting room, has been designed to implement data compression and also to serve as the interface between the custom data transmission protocol of the L0 electronics and the industry-standard Gbit Ethernet protocol used by the DAQ network. The off-detector electronics also performs the important function of isolating the DAQ network from errors induced in the L0 data due to radiation induced SEU.

Each incoming serial data channel is first converted from optical to electrical using Agilent HFBR-782 optical receivers. The serial electrical data are then AC coupled to dedicated I/O pins of Virtex2Pro FPGAs, where they are deserialised using integrated Gbit transceivers that are compatible with the data encoding used by the GOL serialisers in the L0 electronics. All further data processing is done in the FPGA programmable logic.

The L1 electronics modules are controlled by signals broadcast synchronously to all subdetectors by the readout supervisor. These signals are used to control the generation of the data packets sent by the L1 to the DAQ network (see section 8.3). The data content of these packets is extracted from the incoming L0 data frames. The generation of the data packets operates autonomously to the arrival of the L0 data and therefore cannot be disrupted by incoming erroneous data. In order to predict the time of arrival of the L0 data frames so that they can be correctly inserted into the generated data packets, the operation of the L0 electronics is emulated in the off-detector modules using the TFC broadcast signals.

Once the incoming data frames have been received, the zero-suppression algorithm (L1 module copies only the non-zero bytes into the zero-suppressed buffer) is applied in parallel to all streams. The fully pipelined algorithm operates at the 1 MHz input event rate and therefore does not introduce dead-time. Zero-suppressed data are buffered in internal memory in the four ingress FPGAs before being multiplexed into multi-HPD event packets. These packets are then forwarded to the egress FPGA which further multiplexes the data into multi-event packets and transmits them using Gbit Ethernet protocol to the DAQ network using the LHCb quad Gbit Ethernet interface.

The L1 module is configured and monitored via an LHCb Credit Card PC (CCPC) [115] interface. The L1 modules are in 9U format and each can receive data from a maximum of 36 HPDs. The input links are distributed across three 12-channel optical receivers and four Virtex2Pro ingress FPGAs. For 1 MHz operation, the data throughput is expected to be limited by the capacity of the four 1 Gbit/s DAQ links at higher luminosity. Static load balancing is done by physically distributing the input fibre-optic cables across the modules. The bandwidth is distributed across 21 L1 boards to avoid bottlenecks and problems associated with inhomogeneous occupancies in the different parts of the RICH detectors.

6.1.7 Monitoring and control

The RICH Detector Control System (DCS) [116] monitors the working conditions of both RICH 1 and RICH 2, controls the operating conditions and ensures the integration of RICHes in the LHCb detector control system. It is composed of several parts:

- Power supply control and monitoring (low voltage, silicon detector bias and very high voltage);
- Environment monitoring (temperature, pressure, humidity);
- Gas quality monitoring (gas purity);
- Magnetic distortion monitoring (and correction);
- Laser alignment monitoring system.

Power supplies

Low voltage (5 V) for the front-end electronic boards is provided by commercial off-the-shelf devices, the Wiener MARATON power supply. It is radiation and magnetic field tolerant, and can be remotely monitored via a network using standard software interfaces provided by the manufacturer (OPC server). Other lower voltages (e.g. 3.3 V) required by the electronics components are generated, regulated and monitored on each front-end LV board. In addition, to improve reliability, temperature sensors placed near hot spots and critical points allow a quick check of the integrity of the electronics. A similar solution has been adopted for biasing the HPD internal silicon pixel detectors: a standard CAEN SY1527 mainframe power supply with plug-in modules. For the very high voltage of the HPDs (20 kV), no satisfactory commercial solution was found so the system was designed in-house. The system is built around a commercial HV module (ISEG CPn–200 504 24 10) controlled and monitored by a pair of DACs and ADCs connected via an I2C bus interface to a CCPC running the software to regulate the voltage and to connect to the network. The CCPC, using a *bare-bones* version of Linux, runs the control program which, in an endless loop, checks all voltages and currents, and via a DIM protocol [117] reports measurements to the high level control system. In the unlikely case of a loss of the network connection, the CCPC can still check the working conditions and cut power to the HPDs to avoid damage to personnel and HPDs.

Environment

Environmental monitoring (temperature, pressure, humidity of the radiator gas and HPD planes) is achieved using standard commercial sensors, namely platinum resistors for temperature, diaphragm sensors for pressure and HMX2000-HT sensors (by Hygrometrix) for humidity. All these devices are mounted in the harsh radiation environment hence they must be read by radiation tolerant electronics i.e. the *Embedded Local Monitor Board* (ELMB) [118].

Gas quality

The purity of the gas radiator is critical to obtain good photon transparency and for this reason a quick analysis tool to spot any contamination is employed. The stability of the gas composition is checked by periodically monitoring the speed of sound of the gas in the vessel. The speed of sound is given by $v_s = \sqrt{\frac{\gamma RT}{M}}$ where $\gamma = \frac{C_p}{C_v}$ is the ratio of specific heats of the gas, R is the universal gas constant, T the absolute temperature and M the average molecular mass. The speed is monitored by measuring the time that a sound pulse takes to propagate from an electrostatic transducer to the end of a cylindrical vessel and then, reflected by the end wall, back to the same transducer, working now as a microphonic sensor. For RICH 1 this vessel is 0.5 m long and the measured time interval is of the order of 10 ms in C_4F_{10}. For RICH 2 the vessel is approximately 0.3 m long and the relative propagation time is of the order of 3.8 ms in CF_4. The whole system is built around a timer/counter provided by a National Instrument acquisition board. The internal counter, running at 20 MHz, provides 50 ns time resolution, more than adequate to detect a 1% CO_2 contamination (which will give a 50 μs change in C_4F_{10} and 30 μs change in CF_4 for the total transit time). There are two such systems for each RICH detector, one placed on the inlet pipe and the second on the outlet of the fluid system. A typical measurement is shown in figure 6.15 which shows the change in the propagation time when the percentage of CO_2 changes from 0 to 5%.

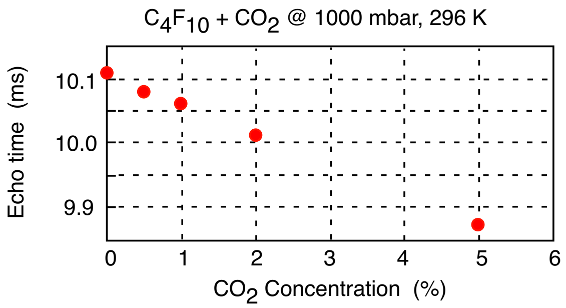

Figure 6.15: Typical sound propagation time as a function of the CO_2 percentage in C_4F_{10}.

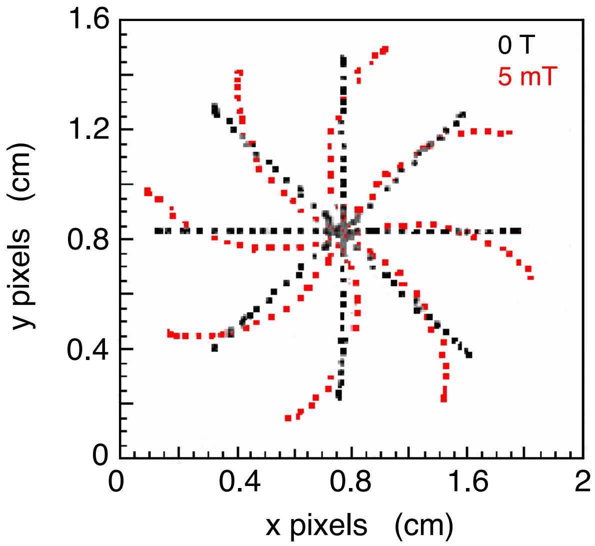

Figure 6.16: Image of a star pattern recorded on an HPD with and without a B-field of 5 mT applied parallel to the HPD axis.

Magnetic distortions

The fringe field of the LHCb dipole magnet distorts the photoelectron trajectories within the hybrid photon detectors, hence distorting the image recorded by the pixel chip. The HPDs are individually shielded by MuMetal cylinders and the arrays are completely surrounded by iron shields, however residual stray fields (up to an expected maximum of 2.4 mT in RICH 1) are sufficient to severely degrade the required precision. This effect can be clearly seen in figure 6.16, which shows how a star pattern recorded without B-field is badly distorted with a 5 mT field applied parallel to the HPD axis. Hence individual correction factors are required for each HPD and the effect of the B-field must be monitored periodically. For RICH 1 an LED system mounted in the *photon funnel* region between the HPDs and the quartz window is used. For RICH 2 a commercial light projection system projecting a fixed pattern of dots from outside the RICH vessel will monitor the magnetic distortions. In both cases the data will be acquired during dedicated calibration runs and the magnetic corrections applied off-line.

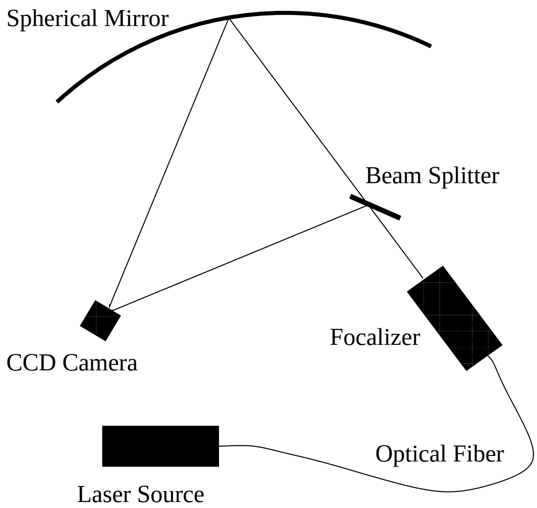

Figure 6.17: Schematic of the mirror alignment monitoring system.

Mirror alignment

Mechanical stability of the mirrors is of paramount importance to achieve the required Cherenkov angular resolution. This stability is challenging due to the size of the mirrors and the difficulty of securing them without introducing mechanical distortions to the reflecting surface. An alignment system which uses a CCD camera monitors mirror movements. On the focal plane of a given mirror, the images of two light spots are formed: the first comes directly from a laser source and the second is reflected back from the monitored mirror. Any change in the relative position of the two spots is an indication of mirror mechanical misalignment and the information is used to make an off-line correction. A schematic of the system is shown in figure 6.17. The laser light source feeds a bundle of optical fibers which generate all the required light paths (eight mirrors will be monitored in RICH 1, 16 in RICH 2). The beams are then directed to the beam splitters which guide the reference beams directly to the CCDs and the secondary beams to the mirrors.

It can be demonstrated that there is a linear transformation law between a change in the mirror tilt $(\Delta\Theta_x, \Delta\Theta_y)$ and the relative movement of the reflected spot on the CCD (Δ_x, Δ_y):

$$\begin{aligned} \Delta\Theta_x &= A\Delta_x + B\Delta_y \\ \Delta\Theta_y &= C\Delta_x + D\Delta_y, \end{aligned}$$

where the parameters A to D are fixed constants which depend on the geometry of the system. The mirror tilts can then be determined by inverting this transformation after observing the spot movement. The system tracks the displacement between the two beam spots, even if the spots move together, with an accuracy of better than 0.01 mrad.

6.1.8 RICH performance

Test Beam studies

An extensive test beam programme has allowed the RICH photodetectors, readout electronics and radiators to be evaluated with Cherenkov radiation in a realistic environment. Of particular impor-

Table 6.2: Comparison of the measured and expected photon yields for the individual HPDs in the RICH test beam run. The first column indicates the label of each HPD.

HPD	$\mu_{\text{meas.}}$	μ_{exp}	$\mu_{\text{meas.}}/\mu_{\text{exp}}$
L0	8.1 $\pm$0.10	11.4 $\pm$0.73	0.71 $\pm$0.07
L1	10.2 $\pm$0.16	10.0 $\pm$0.66	1.02 $\pm$0.07
C1	11.5 $\pm$0.33	11.2 $\pm$0.78	1.02 $\pm$0.07
R0	8.7 $\pm$0.24	8.9 $\pm$0.73	0.98 $\pm$0.09
R1	10.1 $\pm$0.03	10.7 $\pm$0.83	0.95 $\pm$0.08

tance has been the comparison of the expected and observed photoelectron yields and Cherenkov angle resolutions. Because the predictions of these quantities for test beam operation are made using a simulation with identical assumptions to those of the full LHCb MonteCarlo, agreement between prediction and observation is an important indicator that the RICH system will perform to specification.

A demonstrator RICH detector was operated in a test beam utilizing pre-production photon detectors and realistic prototypes of the associated RICH electronics [119]. The tests were performed at the CERN-PS in the T9 facility using 10 GeV/c pions together with an N_2 gas radiator to generate Cherenkov light. The HPDs were arranged in columns with the close-packing arrangement that will be used in the experiment and were read out at the LHC frequency of 40 MHz. In this configuration, the Cherenkov rings from the N_2 gas radiator were fully contained within a single HPD. Having included corrections for the asynchronous nature of the test beam set-up, the photoelectron yields were found to be in good agreement with those expected from the MonteCarlo simulation, as shown in table 6.2. A distribution of the number of pixel hits observed per event on a single HPD is shown in figure 6.18. Uncertainties in the corrections for the asynchronous beam structure explain the residual differences between the data and simulated distributions.

The distribution of reconstructed Cherenkov angles was also found to be in good agreement with the simulation (see figure 6.19). The Cherenkov angle resolution was determined to be 1.66 ± 0.03 mrad, to be compared with the simulation expectation of 1.64 mrad. The dominant contributions to the Cherenkov angle resolution came from the uncertainty in the beam direction, the HPD point-spread function and the HPD pixelisation. The relative contributions of the latter two effects were significant owing to the test beam geometry but are not expected to be dominant in the final LHCb experiment.

Detector simulation

The LHCb RICH system is modelled as part of the LHCb Simulation program based on the GEANT4 simulation toolkit (see chapter 10). All important aspects of the geometry and the material description are fully simulated. A database is setup with all this information which is then input into the simulation and the reconstruction programs.

The Cherenkov light generation is performed inside GEANT4, and the photons propagated with full knowledge of the expected reflectivities, transmissions and refraction effects at the various optical elements. The Rayleigh scattering in aerogel and absorption in the various media are also

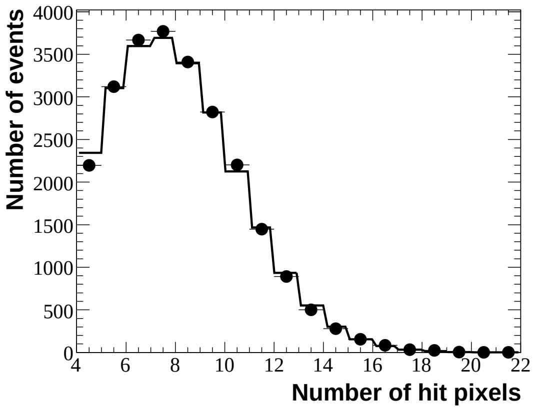

Figure 6.18: Number of pixel hits per event for data (points) and simulation (histogram) for a single HPD used in the RICH test beam run.

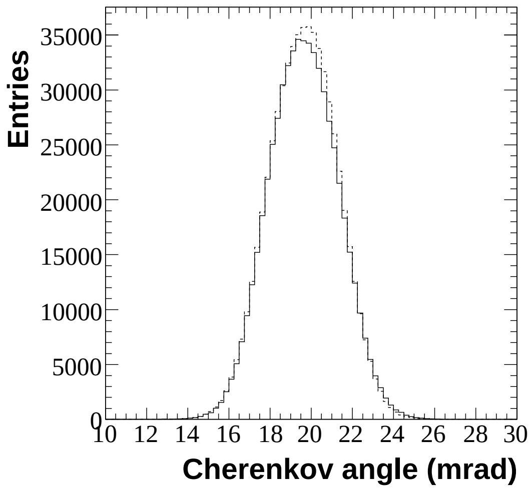

Figure 6.19: Reconstructed Cherenkov angle for data (solid histogram) and simulation (dotted line) on one of the HPDs used in the 2004 RICH test beam run.

included. Inside the HPDs, using the measured quantum efficiencies and cross-focussing relations, the photoelectrons created from the photocathode are mapped down onto the silicon detectors (hits location and energy). From these hits, the charge sharing in the pixels and the response of front-end readout are modelled in a separate package, which creates the digitized hits in the same format which will be output from the operational detector. All known sources of background are simulated. The most important components come from Rayleigh scattered photons in the aerogel, rings from secondary particles without associated reconstructed tracks and Cherenkov light generation in the HPD windows from traversing charged particles. More information on the LHCb RICH simulation may be found in [120]. Figure 6.20 shows a simulated event display in RICH 1.

For a given pixel-track association, the apparent Cherenkov angle is reconstructed through knowledge of the track direction, the hit pixel location, and the geometry of the RICH optics. This reconstruction assumes that the Cherenkov photon was emitted at the midpoint of the radiator. In simulation the resolution on the Cherenkov angle per photoelectron, and the mean number of photoelectrons detected per $\beta \approx 1$ track can be determined by using truth information to ensure that the hit pixel-track association is correct. The mean number of photoelectrons is found to be 6.7 for aerogel, 30.3 for C_4F_{10} and 21.9 for CF_4. The resolution results are shown in table 6.3, where both the total resolutions and the individual contributions are listed. The single photoelectron resolution is largest for the aerogel, at 2.6 mrad, and smallest for the CF_4, at 0.7 mrad. These resolutions receive contributions from the uncertainty associated with the photon emission point, the chromatic dispersion of the radiator, the finite pixel size and the point spread function (together listed as ‘HPD’ in the table). For the aerogel it is the chromatic dispersion error which dominates, whereas for the other two radiators the contributions are well matched. An additional uncertainty comes from the reconstruction of the track direction.

The resulting particle identification performance of the RICH system will be discussed in section 10.

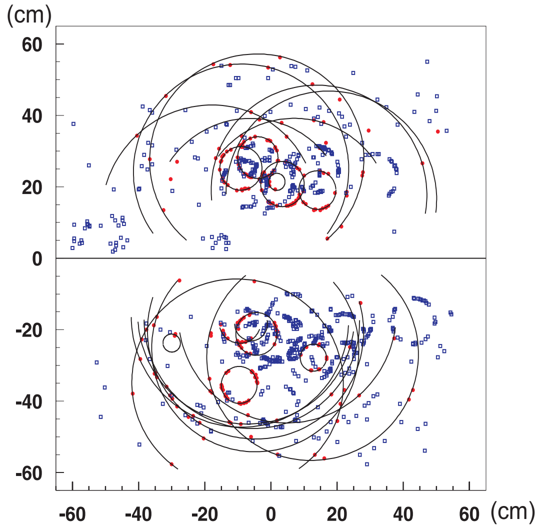

Figure 6.20: Display of a typical LHCb event in RICH 1.

Table 6.3: Single photoelectron resolutions for the three RICH radiators. All numbers are in mrad. Individual contributions from each source are given, together with the total.

	Aerogel	C_4F_{10}	CF_4
Emission	0.4	0.8	0.2
Chromatic	2.1	0.9	0.5
HPD	0.5	0.6	0.2
Track	0.4	0.4	0.4
Total	2.6	1.5	0.7

6.2 Calorimeters

The calorimeter system performs several functions. It selects transverse energy hadron, electron and photon candidates for the first trigger level (L0), which makes a decision 4μs after the interaction. It provides the identification of electrons, photons and hadrons as well as the measurement of their energies and positions. The reconstruction with good accuracy of π^0 and prompt photons is essential for flavour tagging and for the study of B-meson decays and therefore is important for the physics program.

The set of constraints resulting from these functionalities defines the general structure and the main characteristics of the calorimeter system and its associated electronics [1, 121]. The ultimate performance for hadron and electron identification will be obtained at the offline analysis level. The requirement of a good background rejection and reasonable efficiency for B decays adds demanding conditions on the detector performance in terms of resolution and shower separation.

2008 JINST 3 S08005

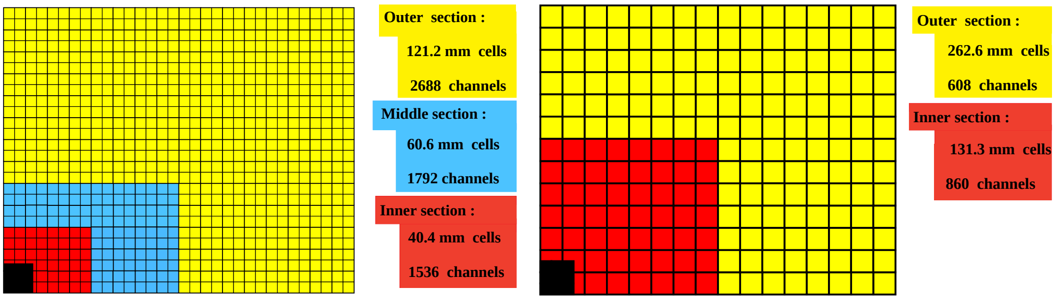

Figure 6.21: Lateral segmentation of the SPD/PS and ECAL (left) and the HCAL (right). One quarter of the detector front face is shown. In the left figure the cell dimensions are given for the ECAL.

6.2.1 General detector structure

A classical structure of an electromagnetic calorimeter (ECAL) followed by a hadron calorimeter (HCAL) has been adopted. The most demanding identification is that of electrons. Within the bandwidth allocated to the electron trigger (cf. section 7.1.2) the electron Level 0 trigger is required to reject 99% of the inelastic pp interactions while providing an enrichment factor of at least 15 in b events. This is accomplished through the selection of electrons of large transverse energy E_T. The rejection of a high background of charged pions requires longitudinal segmentation of the electromagnetic shower detection, i.e. a preshower detector (PS) followed by the main section of the ECAL. The choice of the lead thickness results from a compromise between trigger performance and ultimate energy resolution [122]. The electron trigger must also reject a background of π^0's with high E_T. Such rejection is provided by the introduction, in front of the PS, of a scintillator pad detector (SPD) plane used to select charged particles. A thin lead converter is placed between SPD and PS detectors. At Level 0, the background to the electron trigger will then be dominated by photon conversions in the upstream spectrometer material, which cannot be identified at this stage. Optimal energy resolution requires the full containment of the showers from high energy photons. For this reason, the thickness of ECAL was chosen to be 25 radiation lengths [123]. On the other hand, the trigger requirements on the HCAL resolution do not impose a stringent hadronic shower containment condition. Its thickness is therefore set to 5.6 interaction lengths [124] due to space limitations.

The PS/SPD, ECAL and HCAL adopt a variable lateral segmentation (shown in figure 6.21) since the hit density varies by two orders of magnitude over the calorimeter surface. A segmentation into three different sections has been chosen for the ECAL and projectively for the SPD/PS. Given the dimensions of the hadronic showers, the HCAL is segmented into two zones with larger cell sizes.

All calorimeters follow the same basic principle: scintillation light is transmitted to a Photo-Multiplier (PMT) by wavelength-shifting (WLS) fibres. The single fibres for the SPD/PS cells are read out using multianode photomultiplier tubes (MAPMT), while the fibre bunches in the ECAL and HCAL modules require individual phototubes. In order to have a constant E_T scale the gain in the ECAL and HCAL phototubes is set in proportion to their distance from the beampipe. Since the light yield delivered by the HCAL module is a factor 30 less than that of the ECAL, the HCAL tubes operate at higher gain.

6.2.2 Electronics overview

The basic structure is dictated by the need to handle the data for the Level 0 trigger as fast as possible. The front-end electronics and the PS/SPD photomultipliers are located at the detector periphery. The HCAL and ECAL phototubes are housed directly on the detector modules. The signals are shaped directly on the back of the photomultiplier for the PS/SPD or after 12 m and 16 m long cables for ECAL and HCAL respectively. They are then digitized in crates positioned on top of the detectors and the trigger circuits, hosted in the same crates, perform the clustering operations required by the trigger [125]. For each channel, the data, sampled at the bunch crossing rate of 40 MHz, are stored in a digital pipeline until the Level-0 trigger decision. In order to exploit the intrinsic calorimeter resolution over the full dynamic range, ECAL and HCAL signals are digitized by a 12-bit flash ADC [126]. Ten bits are enough for the preshower, and the SPD information is only one bit, a simple discriminator recording whether a cell has been hit or not [127, 128]. An additional requirement is to reduce the tails of signals associated to the bunch crossing preceding the one being sampled. For ECAL and HCAL, this goal can be achieved at the percent level by suitable signal treatment within 25 ns. In the case of the PS and SPD, the signal shape fluctuations require the longest possible signal integration time. They therefore use a different front-end design for the integrator, as described in section 6.2.7. Finally, in order not to degrade the resolution, the electronic noise must remain at the least significant bit level [129]. At the short shaping times being used, this requires careful design of the very front-end part.

6.2.3 The pad/preshower detector

The pad/preshower (SPD/PS) detector uses scintillator pad readout by WLS fibres that are coupled to MAPMT via clear plastic fibres. The choice of a 64 channel MAPMT allowed the design of a fast, multi-channel pad detector with an affordable cost per channel.

The SPD/PS detector consists of a 15 mm lead converter 2.5 X_0 thick, that is sandwiched between two almost identical planes of rectangular scintillator pads of high granularity with a total of 12032 detection channels (figure 6.22 left). The sensitive area of the detector is 7.6 m wide and 6.2 m high. Due to the projectivity requirements, all dimensions of the SPD plane are smaller than those of the PS by $\sim$0.45%. The detector planes are divided vertically into two halves. Each can slide independently on horizontal rails to the left and right side in order to allow service and maintenance work. The distance along the beam axis between the centres of the PS and the SPD scintillator planes is 56 mm. In order to achieve a one-to-one projective correspondence with the ECAL segmentation (described in section 6.2.4), each PS and SPD plane is subdivided into inner (3072 cells), middle (3584 cells) and outer (5376 cells) sections with approximately 4×4, 6×6 and $12 \times 12\,\text{cm}^2$ cell dimensions.

The cells are packed in $\sim 48 \times 48\,\text{cm}^2$ boxes (detector units) that are grouped into supermodules. Each supermodule has a width of $\approx$ 96 cm, a height of $\approx$ 7.7 m and consists of detector units that form 2 rows and 13 columns. The space available for the SPD/PS detector between the first muon chamber and the electromagnetic calorimeter is only 180 mm. Figure 6.22 (right) shows an individual scintillator pad with the WLS fibre layout. The diameter of the WLS fibre groove is a few mm smaller than the tile size; exact parameters of the tile geometry can be found in [130]. The basic plastic component is polystyrene to which primary and secondary WLS dopants, parater-

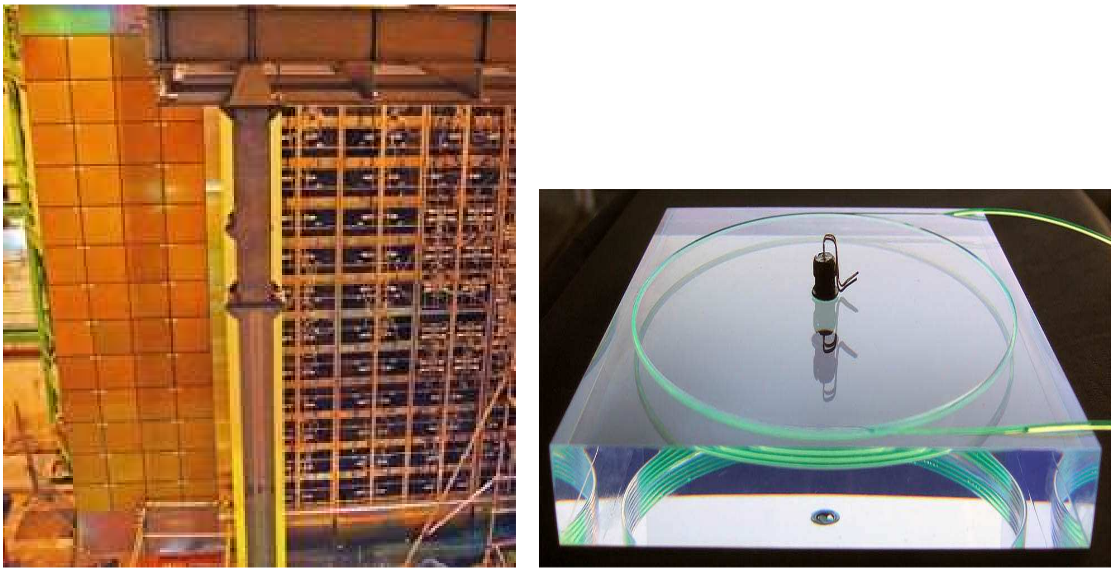

Figure 6.22: Front view of one half of the SPD/PS installed in the LHCb experimental hall (left). Individual scintillator pad with the WLS fibre layout and the LED housing in the middle (right).

phenyl (PTP), 1.5% and POPOP, 0.04%, are added.[11] The square structure of a pad is cut out from a 15 mm thick scintillator plate, and the scintillator surface is polished to reach the necessary optical quality. In order to maximize the light collection efficiency, WLS fibres are coiled and placed into a ring groove that is milled in the body of the cell. The rectangular cross section of the groove is 4.1 mm deep and 1.1 mm wide. The groove contains 3.5 loops of WLS fibre. The number of loops was chosen to achieve an overall optimization of the light collection efficiency [131] and the signal formation [132]. Two additional grooves are milled in the scintillator allowing both ends of the WLS fibre to exit the plate. The fibre is glued inside the groove[12] using a dedicated semi-automatic device that provides the winding of the fibre and a uniform glue filling along the groove. A 1.0 mm diameter Y11(250) MS70 multi-cladding S-type WLS fibre[13] was chosen as a reasonable compromise between light output and durability. The pad is wrapped with 0.15 mm thick TYVEK[14] paper in order to improve the light reflection and to minimize the dead space between adjacent pads. Light produced by an ionizing particle in the scintillator is guided by the WLS fibre to the exit of the detector box. At this point optical connectors (described in [130]) join the WLS fibres to long clear fibres. The two clear fibres connected to the two ends of the WLS fibre of a given pad are viewed by a single MAPMT pixel [130]. The length of clear fibres varies from 0.7 to 3.5 m but all the fibres connected to a particular PMT have the same length in accordance with the front-end electronics specification [127, 128]. The clear fibre allows the transport of the scintillator light from the SPD/PS planes over a few metres to the multi-anode PMT without significant attenuation.

The scintillator cells are grouped into self-supporting detector units that are packed inside square boxes with dimension 476 mm $\times$ 476 mm (SPD) and 478 mm $\times$ 478 mm (PS) boxes, yield-

[11]produced at SSI *Institute for Single Crystals* NAS of Ukraine, 60 Lenin Ave, Kharkov, 61001, Ukraine.
[12]with BICRON BC-600 glue, BICRON Corp., 12345 Kinsman Rd. Newbury OH 440 USA.
[13]KURARAY Corp., 3-10, Nihonbashi, 2 chome, Chuo-ku, Tokyo, Japan.
[14]TYVEK of type 1057D used, product of E.I. du Pont de Nemours and Company.

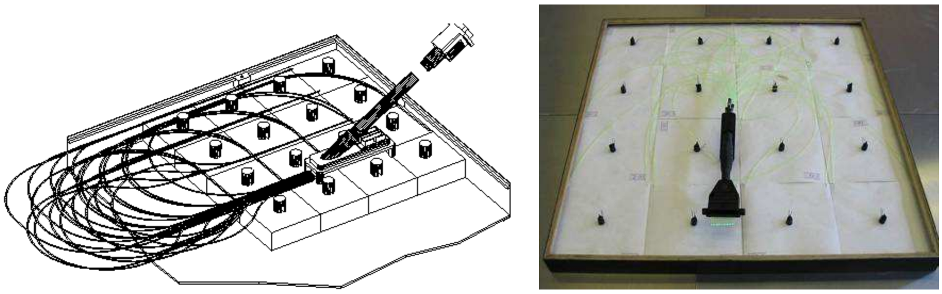

Figure 6.23: Fibre routing for the inner (left) and outer (right) module boxes.

ing a total of 26 boxes per supermodule. Since there are three sections with different cell sizes for the SPD/PS planes, the boxes are filled with a different number of pads with sizes that add up to 119 mm for the SPD to 119.5 mm for the PS planes. A dedicated fibreglass technology of box manufacturing was developed in order to obtain stiff boxes with a minimum amount of material between the adjacent cells of neighbouring boxes. The lateral walls of the monolithic box frame are manufactured using Fibreglass Reinforced Plastic (FGRP) with a wall thickness of 0.3 mm. This fabrication method consists of a one cycle polymerization process with predefined curing parameters. To ensure light tightness a layer of black paper was incorporated in addition to the FGRP layer. The top and bottom layers of the box are made of 2 mm thick Al plate and G10 plastic. The bottom cover is glued to the FGRP frame by epoxy and the top one is fixed by screws. On the top cover there are output plastic ports, made of relatively cheap pressure die casting technology, disposed to allow exit of fibre bundles out of the box. The module assembly procedure is as follows. All cells in a detector unit are grouped in matrices of 4×4 cells. The scintillator pads with glued WLS fibres are placed into the box after quality control tests. The fibre ends are grouped by 32, fit into a light-tight flexible tube and glued into an optical connector, before being cut and polished. The routing of fibres inside a box from one matrix is shown in figure 6.23. The bending diameter always exceeds 100 mm. Depending on the number of scintillator cells inside a unit, the boxes are equipped with one (outer region), four (middle region) or nine (inner region) output port(s) and light connector(s).

The detector units are designed to be mounted on a supermodule support plate. All supermodules of the SPD/PS planes have identical design. Each consists of 26 detector units mounted on a long aluminium strip in two columns. The photomultiplier tubes are located on both the top and bottom ends of the supermodule support outside the detector acceptance. The detector units are optically connected to the PMTs by bundles of 32 clear fibres, enclosed in a light-tight plastic tube, by means of a photo-tube coupler. The PMT is a (8-stage) R5900-M64 manufactured by Hamamatsu[15][133, 134] and has a bialkali photocatode segmented into 64 pixels of 2×2 mm^2. The HV is provided by a Cockroft-Walton voltage multiplier.

The quality of the phototubes has been extensively studied using measurements of the nonuniformities of anode response within one MAPMT, the linearity over the required dynamic range of the PS, the absolute gain of the MAPMT channels and the electronic crosstalk. The nonuniformity

[15] HAMAMATSU Photonics KK, Electron Tube Center, 314-5, Shimokanzo, Toyooka-village, Iwata-gun, Shizuoka-ken, 438-01 Japan.

of response within one MAPMT was found to be in a ratio of 1 to 2 (minimum to maximum) for most of the installed tubes. A special care has been brought to the selection of the best tubes for the PS in order to limit the digital correction to at most a factor of 2 at the level of the front-end (FE) electronics. While the crosstalk between the PMT electronics channels has been measured to be negligible, a large number of tubes showed large crosstalk produced at the level of the focussing grid, immediately behind the MAPMT photocathode. This was one of the major cause for rejection. The response linearity was found to be well within specification for all the tested phototubes [135].

Specific measurements of the MAPMT behaviour in the magnetic field were carried out as well. It has been discovered that these phototubes, initially thought to be robust in a magnetic field were significantly sensitive to fields as weak as 1 mT. A dedicated magnetic shielding has been designed. A MuMetal cylinder (6 cm long with a 4 cm diameter) is used along the tube axis and the MAPMT (together with the very front-end (VFE) electronics) are housed in a box made of soft iron. Special attention was given to evaluate the long term behaviour of the phototubes subject to the conditions of the largest illumination of the PS (DC currents for the SPD are much smaller than for the PS [136]). The PMT gain is set to 10^4, which gives stable conditions of operation. Prior to the installation all the SPD and PS modules were tested using a cosmic ray facility. Using a reference LED the average number of photoelectrons per Minimum Ionizing Particle (MIP) was measured to be 26, 28 and 21 for the PS and SPD cells of the inner, middle and outer regions correspondingly. During the production phase the light yield was measured for all tiles using a gamma radiation source. The tiles with similar light yield were grouped within the same matrix. The uniformity of matrices, also affected by the uniformity of the optical cables, was measured in a cosmic test of the detector supermodules. The uniformity of response within matrices was found to be within 6% RMS.

Performance of the SPD/PS modules

The e/π separation performance of the PS prototype was measured in the X7 test beam at the CERN SPS with electrons and pions between 10 and 50 GeV/c momentum. The energy deposited in the PS for 50 GeV/c electrons and pions is shown in figure 6.24.

The measurements show that with a threshold of 4 MIPs (about 100 ADC channels), pion rejection factors of 99.6%, 99.6% and 99.7% with electron retentions of 91%, 92% and 97% are achieved for 10, 20 and 50 GeV/c particle momentum, respectively. From measurements with 20 GeV electrons in the combined PS and ECAL test, it is confirmed that the energy resolution of the ECAL does not deteriorate if one corrects for the energy absorbed in the PS lead converter using the energy measured in the PS scintillator [131]. In order to separate photons and electrons at Level 0 of the ECAL trigger, the information from the SPD positioned in front of the lead absorber is used. Charged particles deposit energy in the scintillator material, while neutrals particles do not interact. However, several processes can lead to an energy deposit in the scintillator and result in the misidentification of photons. The dominant one is the photon conversion in the detector material before the SPD (see sections 10.2.3 and 10.2.4). Two other sources are interactions in the SPD that produce charged particles inside the SPD, and backwards moving charged particles, *back splash*, that are generated in the lead absorber or in the electromagnetic calorimeter. The latter two

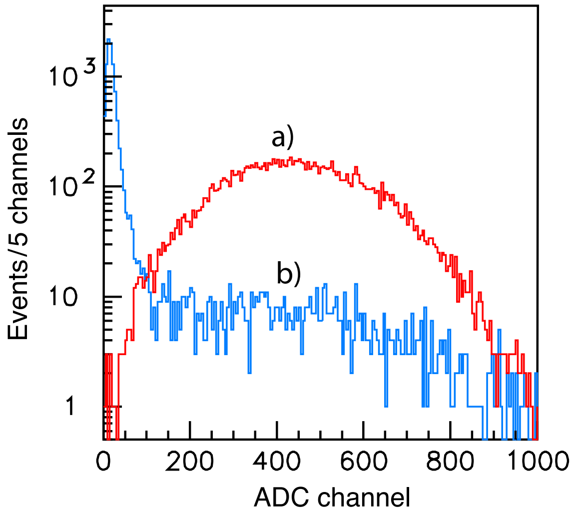

Figure 6.24: Energy deposition of (a) 50 GeV electrons and (b) pions in the PS.

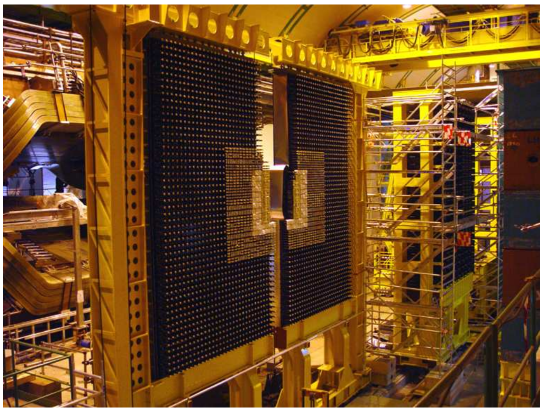

Figure 6.25: Downstream view of the ECAL installed (but not completely closed) with the exception of some detector elements above the beam line. Outer, middle and inner type ECAL modules (right).

effects have been studied with the prototype in both a tagged photon beam and beams of electrons and pions of different energies, in the CERN X7 test beam area. The results were compared with simulation. The measurements for photon energies between 20 and 50 GeV show [137] that the probability of photon misidentification due to interactions in the SPD scintillator is (0.8±0.3)%, when applying a threshold of 0.7 MIPs. The probability to pass this threshold due to backward moving charged particles was measured to be (0.9±0.6)% and (1.4±0.6)% for 20 and 50 GeV photons, respectively. All these numbers are in very good agreement with MonteCarlo simulation study. More details on backsplash study can be found in [137].

2008 JINST 3 S08005

Table 6.4: Main parameters of the LHCb electromagnetic calorimeter. (*) Only 1536 channels are active, instead of 1584, due to the clearance around the beam.

	Inner section	Middle section	Outer section
Inner dimension, $x \times y$, cm^2	65×65	194×145	388×242
Outer dimension, $x \times y$, cm^2	194×145	388×242	776×630
Cell size, cm^2	4.04×4.04	6.06×6.06	12.12×12.12
# of modules	176	448	2688
# of channels	1536*	1792	2688
# of cells per module	9	4	1
# of fibres per module	144	144	64
Fibre density, cm^{-2}	0.98	0.98	0.44

6.2.4 The electromagnetic calorimeter

The shashlik calorimeter technology, i.e. a sampling scintillator/lead structure readout by plastic WLS fibres, has been chosen for the electromagnetic calorimeter not only by LHCb but by a number of other experiments [138, 139]. This decision was made taking into account modest energy resolution, fast time response, acceptable radiation resistance and reliability of the shashlik technology, as well as the experience accumulated by other experiments [140–142]. Specific features of the LHCb shashlik ECAL are an improved uniformity and an advanced monitoring system. The design energy resolution of $\sigma_E/E = 10\%/\sqrt{E} \oplus 1\%$ (E in GeV) results in a B mass resolution of 65 MeV/c^2 for the $B \to K^*\gamma$ penguin decay with a high-E_T photon and of 75 MeV/c^2 for $B \to \rho\pi$ decay with the π^0 mass resolution of ~ 8 MeV/c^2.

The electromagnetic calorimeter, shown in figure 6.25 (left), is placed at 12.5 m from the interaction point. The outer dimensions of the ECAL match projectively those of the tracking system, $\theta_x < 300$ mrad and $\theta_y < 250$ mrad; the inner acceptance is mainly limited by $\theta_{x,y} > 25$ mrad around the beampipe due to the substantial radiation dose level. The hit density is a steep function of the distance from the beampipe, and varies over the active calorimeter surface by two orders of magnitude. The calorimeter is therefore subdivided into inner, middle and outer sections (table 6.4) with appropriate cell size, as shown in figure 6.25 (right).

A module is built from alternating layers of 2 mm thick lead, 120 μm thick, white, reflecting TYVEK[16] paper and 4 mm thick scintillator tiles. In depth, the 66 Pb and scintillator layers form a 42 cm stack corresponding to 25 X_0. The Moliere radius of the stack is 3.5 cm. The stack is wrapped with black paper, to ensure light tightness, pressed and fixed from the sides by the welding of 100 μm steel foil.

The scintillator tiles are produced from polystyrene[17] with 2.5% PTP[18] and 0.01% POPOP[19] admixtures. The scintillator tile production employs a high pressure injection moulding technique. Tile edges are chemically treated to provide diffusive reflection and consequently improved light

[16]TYVEK of type 1025D used, product of E.I. du Pont de Nemours and Company.

[17]Polystherene in pellets, Polystyrol 165H, [Cn Hn], product of BASF AG, Badische Anilin- & Soda Fabrik Aktiengesellschaft, Carl-Bosch-Strasse 38, D-67056 Ludwigshafen, Germany, mailto:global.info@basf.com.

[18]PTP, p-Terphenyl, 1,4-Diphenylbenzene, [C6 H5 C6 H4 C6 H5], product of FLUKA(TM), Sigma-Aldrich Chemie GmbH, CH-9470, Buchs, Switzerland, mailto:fluka@sial.com.

[19]POPOP, 1,4-Bis(5-phenyl-2-oxazolyl)benzene, [C24 H16 N2 O2], product of FLUKA(TM), Sigma-Aldrich Chemie GmbH, CH-9470, Buchs, Switzerland, mailto:fluka@sial.com.

2008 JINST 3 S08005

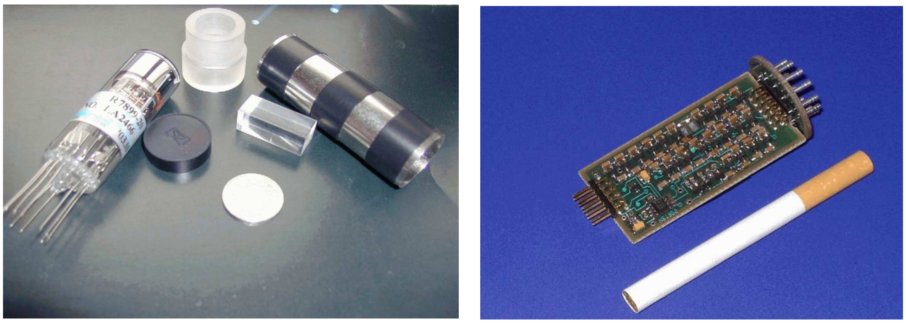

Figure 6.26: Hamamatsu R7899-20 phototube, light mixer and MuMetal magnetic shielding screen (left). Cockcroft-Walton voltage multiplier (right).

collection efficiency and prevent tile-to-tile light crosstalk for the inner and middle modules. The tile-to-tile light yield fluctuation has an RMS smaller than 2.5%. The Pb plates are produced using sheet-metal stamping. In order to ease handling of the lead plates during module assembly the plates are covered with a 3μm thick layer of tin. Both the scintillator tiles and lead plates incorporate a pattern of precisely positioned holes that are needed for the traversing fibres. The demanding tolerances are ensured by injection moulding for the scintillator tiles and a punching technique for the lead plates.

The light from the scintillator tiles is absorbed, re-emitted and transported by 1.2 mm diameter WLS Kuraray Y-11(250)MSJ fibres, traversing the entire module. In order to improve light collection efficiency the fibres are looped such that each traverses the module twice, the looped part remaining in a housing outside the front of the module. Fibre bending under uniformly distributed dry heat made it possible to produce fibre loops with radii as small as 10 mm, where the light loss is determined by the geometrical optics of reflection down the loop. When measured after the fibre loop, the light yield varies from loop to loop with an RMS of the spread of 1.6%. The fibres belonging to each cell are bundled at the rear end of the module and polished.

The light is read out with Hamamatsu R7899-20 phototubes where the high voltage is provided by a Cockcroft-Walton (CW) base (figure 6.26).

Before installation all ECAL modules underwent detailed quality control at various stages of production. The final control was made with cosmic rays [143]. The standard deviations of the mean energy deposition by a MIP in the ECAL module was measured to be 7.4%, 4.4% and 6.0% for the outer, middle and inner sections respectively. The number of photoelectrons recorded for a MIP and for electrons in the test beam was calculated using the measurements of the amplitude and width of the LED signal. This method gives for the inner modules about 3100 photoelectrons per GeV of deposited energy, 3500 for the middle and 2600 for the outer modules. The differences are due to the differing WLS fibre density in the inner, middle and outer modules and to the cell size differences which influence the probability of photon absorption in the scintillating tiles.

Performance of the ECAL modules

The energy resolution and, in particular, the uniformity in response of the ECAL were studied at the test beam [144]. Only a few percent of the scintillation light is registered by the phototubes

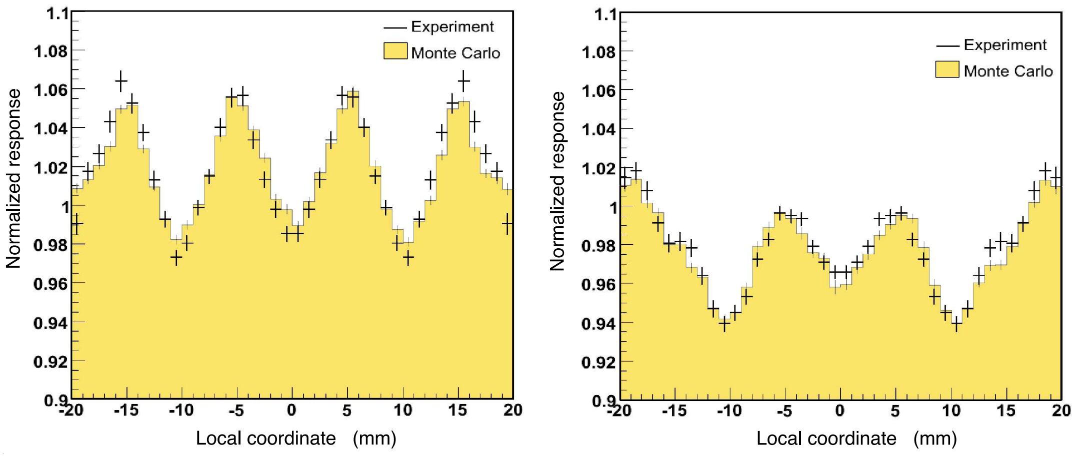

Figure 6.27: Uniformity of response to 100 GeV/c^2 muons of the inner module. The scan was made in 1 mm wide slices through the fibre positions (left) and in between two fibre rows (right).

after capture and re-emission in the WLS fibres; about half of this light is delivered by the WLS fibres close to the light's origin. Some lateral nonuniformity in the light collection efficiency was expected from two sources: imperfect reflection from tile edges (the so-called global nonuniformity effect), and a dependence on the emission point of the scintillating light with respect to the fibres (local or inter-fibre nonuniformity). The global nonuniformity depends on the mean light path, which is a function of tile transparency, edge reflection quality and fibre density. In addition the module response at the edge is further degraded due to the presence of the stainless steel foils between the active volumes of two adjacent modules. The local nonuniformity is affected by the inter-fibre distance and the diameter of the fibre.

The light collection efficiency was studied using test beam data and a dedicated MonteCarlo simulation of the light propagation and absorption in the plastic tiles which takes into account the transparency of the scintillator as a function of wavelength, the tile-edge and TYVEK reflection properties and the WLS fibre absorption spectrum. The modules of the inner, middle and outer sections were scanned using 100 GeV/c muons with a 1 mm transverse step. As shown in figure 6.27, the measured inner module response is well described by MonteCarlo simulation. Shown are two different scans for the inner module, one using 1 mm wide slices through the WLS fibre positions (left plot), and the other between two fibre rows (right plot). In the outer modules the inter-fibre nonuniformity is slightly higher due to a factor of 1.5 larger fibre-to-fibre distance (15 mm instead of 10 mm for the inner and middle modules). The global nonuniformity of response was measured to be negligible for all module types. A slight increase of response in the vicinity of the module edges is explained by diffuse reflection from the boundary layer introduced by the dedicated chemical treatment of the tile edges. The effect of signal loss in the dead material between the modules is overcompensated by 8% at -20 and 20 mm, as visible in figure 6.27 (right). Electromagnetic showers of electrons and photons considerably reduce the inter-fibre nonuniformity of response compared to that measured for MIPs. The results of a lateral scan with 50 GeV/c electrons is shown in figure 6.28 for the inner and outer ECAL modules. The module response is

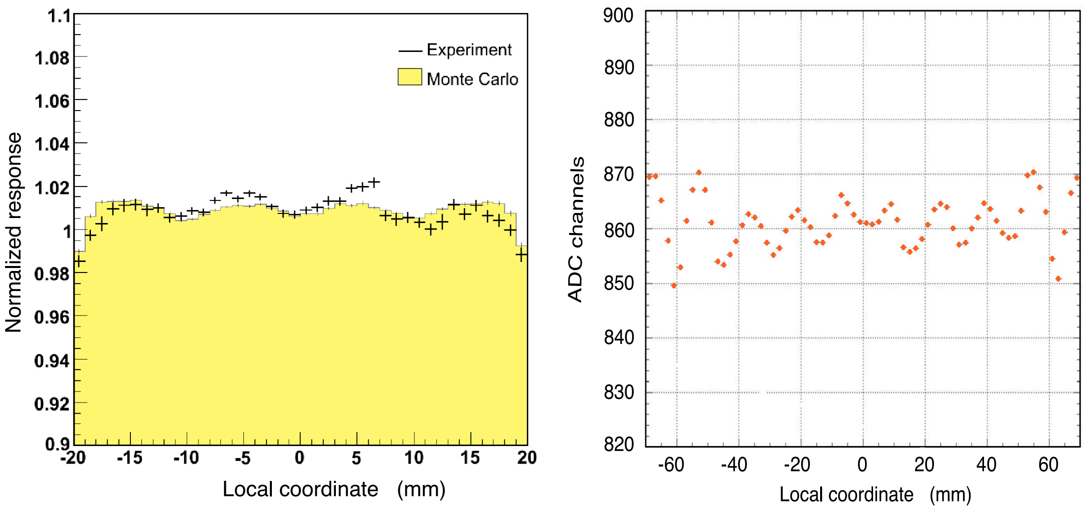

Figure 6.28: Uniformity of response to 50 GeV/c electrons of the inner (left) and outer (right) modules. The scan was made in 1 mm wide slices through the fibre positions.

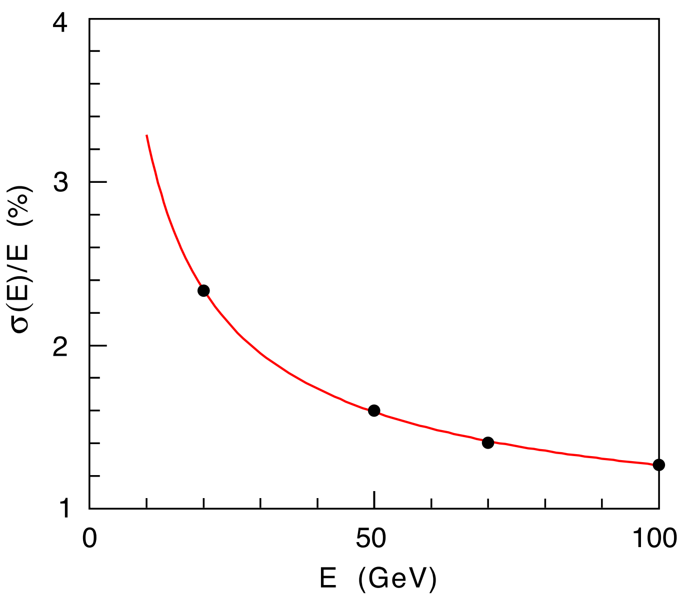

Figure 6.29: The energy resolution as measured with electrons over a surface of (± 15 mm , ± 30 mm) in an outer module.

uniform within 0.8%. The energy resolution of the ECAL modules has been determined at the test beam. The parametrization $\sigma_E/E = \mathrm{a}/\sqrt{E} \oplus \mathrm{b} \oplus \mathrm{c}/E$ (E in GeV) is used, where a, b and c stand for the stochastic, constant and noise terms respectively. Depending on the type of module and test beam conditions the stochastic and constant terms were measured to be $8.5\% <$ a $< 9.5\%$ and b $\sim 0.8\%$ (see figure 6.29).

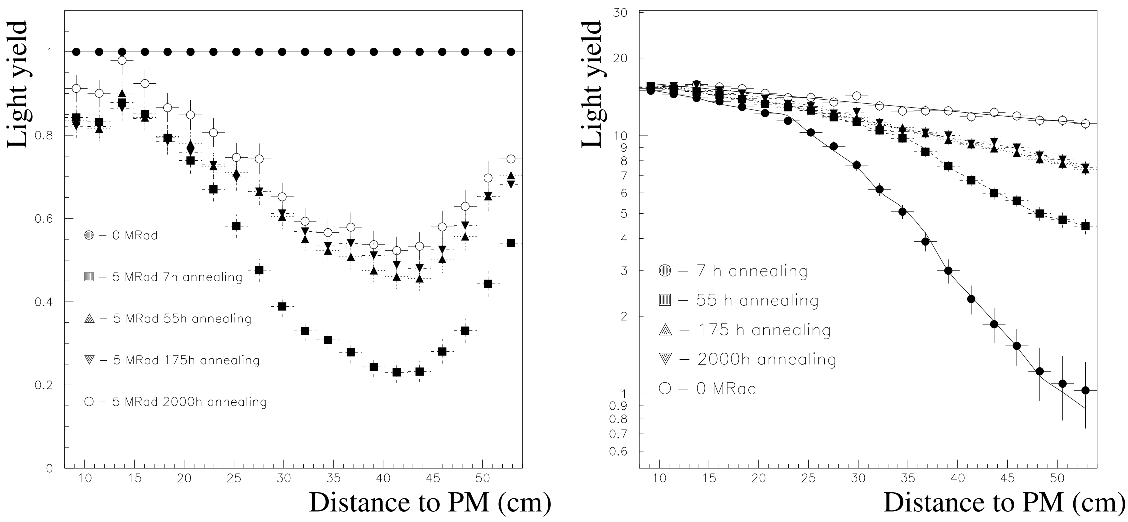

Figure 6.30: Scintillator (left) and WLS fibre (right) degradation and annealing effect after irradiation at LIL. The light yield (scintillator) and PMT current (fibres) are shown vs. the distance to the PMT (the shower maximum position corresponds to a distance from the PMT of 42 cm).

Radiation resistance of the ECAL modules

Detailed measurements and simulation studies were performed to determine the degradation of the ECAL resolution due to radiation damage of the optical components. The expected annual radiation dose at the shower maximum for the ECAL modules closest to the beampipe is 0.25 MRad assuming a luminosity of $2 \times 10^{32}\mathrm{cm}^{-2}\mathrm{s}^{-1}$ and 10^7 s per nominal year. The optical components of the ECAL modules, namely the $40 \times 40\,\mathrm{mm}^2$ scintillating tiles and WLS fibres, were irradiated at the LEP Injector Linac (LIL) at CERN with electrons of 500 MeV energy. The total irradiation dose was as large as 5 MRad at a dose delivery rate of 10 Rad/s; that is 200 times higher than the rate expected at LHCb. Figure 6.30 shows the degradation in light yield and transparency, and the subsequent annealing of the irradiated components as a function of the distance to the phototube. In order to determine the degradation of the energy resolution due to irradiation, the energy response of the ECAL module was simulated using the expected longitudinal dose profile and the measured degradation of the scintillating tiles and WLS fibres in accordance with figure 6.30. The effects induced by irradiation of 2.2 MRad leads to an increase of the constant term from 0.8% up to 1.5%. Such a degradation in the ECAL resolution is expected after about eight years of operation under nominal conditions and is acceptable. However, taking into account simulation uncertainties on the expected radiation doses at the LHC, the ECAL detector was designed such that the modules closest to the beampipe could be replaced if this should become necessary.

6.2.5 The hadron calorimeter

The LHCb hadron calorimeter (HCAL) [1, 121] is a sampling device made from iron and scintillating tiles, as absorber and active material respectively. The special feature of this sampling structure is the orientation of the scintillating tiles that run parallel to the beam axis. In the lateral direction

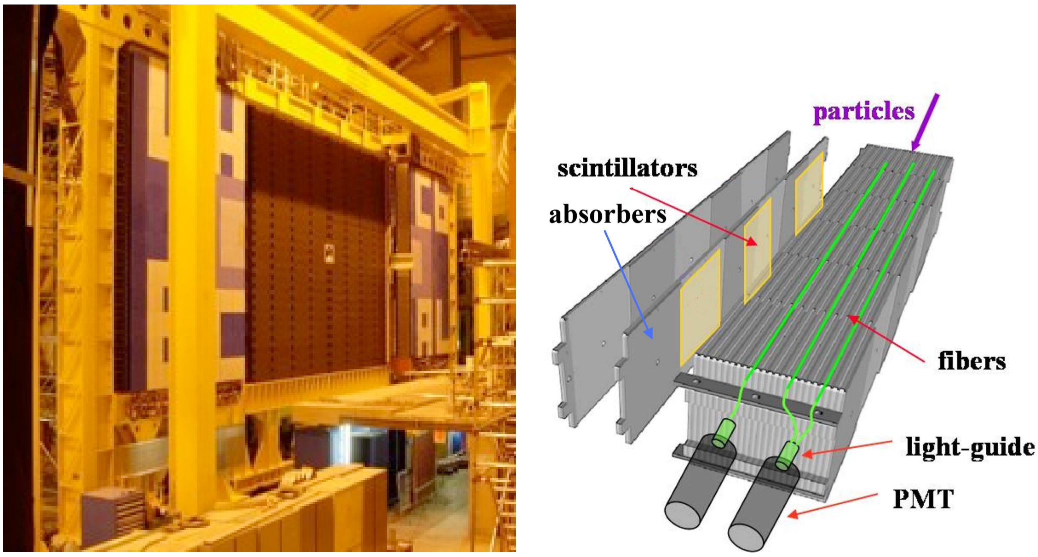

Figure 6.31: View from upstream of the HCAL detector installed behind the two retracted ECAL halves in the LHCb cavern (left). A schematic of the internal cell structure (right). The exploded view of two *scintillator-absorber* layers illustrates the elementary periodic structure of a HCAL module.

tiles are interspersed with 1 cm of iron, whereas in the longitudinal direction the length of tiles and iron spacers corresponds to the hadron interaction length λ_I in steel. The light in this structure is collected by WLS fibres running along the detector towards the back side where photomultiplier tubes (PMTs) are housed. As shown in figure 6.31, three scintillator tiles arranged in depth are in optical contact with 1.2 mm diameter Kuraray[20] Y-11(250)MSJ fibre [145] that run along the tile edges. The total weight of the HCAL is about 500 tons.

The HCAL is segmented transeversely [146] into square cells of size 131.3 mm (inner section) and 262.6 mm (outer section). Readout cells of different sizes are defined by grouping together different sets of fibres onto one photomultiplier tube that is fixed to the rear of the sampling structure. The lateral dimensions of the two sections are ± 2101 mm and ± 4202 mm in x and ± 1838 mm and ± 3414 mm in y for the inner and outer section, respectively. The optics is designed such that the two different cell sizes can be realized with an absorber structure that is identical over the whole HCAL. The overall HCAL structure is built as a wall, positioned at a distance from the interaction point of z=13.33 m with dimensions of 8.4 m in height, 6.8 m in width and 1.65 m in depth. The structure is divided vertically into two symmetric parts that are positioned on movable platforms, to allow access to the detector. Each half is built from 26 modules piled on top of each other in the final installation phase. The assembled HCAL is shown in figure 6.31(left). The absorber structure, shown in figure 6.31 (right), is made from laminated steel plates of only six different dimensions that are glued together. Identical periods of 20 mm thickness are repeated 216 times in the module. One period consists of two 6 mm thick master plates with a length of 1283 mm and a height of 260 mm that are glued in two layers to several 4 mm thick spacers of 256.5 mm in height and variable length. The space is filled with 3 mm scintillator.

[20]KURARAY Corp., 3-10, Nihonbashi, 2 chome, Chuo-ku, Tokyo, Japan.

The periodic structure of the system is designed to be self supporting and uniformly instrumented with no dead zones. To facilitate the construction of modules, each module is subdivided into eight sub-modules that have a manageable size for assembly from the individual absorber plates. A total of 416 submodules have been produced to form 52 modules needed to build up the two halves of the HCAL structure. The mechanical structure is reinforced by welded cross members and is completely independent from the optical instrumentation.

The optics of the tile calorimeter consists of three components: the scintillating tile, the WLS fibre and a small square light mixer just in front of the photo-multiplier entrance window. The scintillating light propagates through the 3 mm thick tile to its edges where it is collected by 1.2 mm diameter WLS fibres.

In total more than 86000 tiles of two different dimensions have been produced by the cost effective casting technology using polystyrene as a base and two dopants: paraterphenyl (PTP, 1.75%) and POPOP (0.05%). Each tile of 197×256 mm^2 or 197×127 mm^2 is wrapped in a 120–150 micron thick TYVEK envelope.[21]

The edges of a tile are wrapped in such a way that the fibre running along the edge can be easily inserted between the envelope and the tile edge during the module optics assembly. This reflective envelope avoids light crosstalk between adjacent edges of the small tiles, enhances the light collection in the wavelength shifting fibre and in addition protects the optical reflective surface of the tiles. Each fibre collects light from three scintillator tiles arranged along the shower development direction. There are a total of 50k fibres in the HCAL with an identical length of 1.6 m. In order to increase the light collection efficiency both fibre ends were cut with a diamond mill, and opposite to the photomultiplier end coated with a layer of reflective aluminum deposited in vacuum. The reflectivity of all fibres was checked on a measuring stand specially designed for that purpose. All fibres were measured to have a mirror reflectivity in the range of (85 ± 10)%. The light propagates along the fibre by total reflection but tiles located further from the PMT yield less light due to attenuation in the WLS fibre. To compensate for this effect, the tile-fibre optical contact was progressively reduced for the different tile layers in depth. The last tile layer closest to the PMT has an optical contact reduced by 22% as compared to the first layer at the entry of the HCAL. This precaution minimizes the difference in response between tiles, providing light to the same PMT with a uniformity at a level of a few percent.

Each cell is read out by one photomultiplier tube that is attached to the rear mechanical structure of the module. The optical connection between the fibre bundle and the photomultiplier is ensured by a 35 mm long light mixer of square shape. To shield the photomultiplier tube from the stray magnetic field the tube, including the light mixer, is housed inside a 3 mm thick iron tube and MuMetal foil. The influence of the magnetic field on a PMTs performance was studied during the LHCb magnet measurement. A field of approximately 2 mT along z, but negligible in x and y, is expected in the region of the HCAL PMTs [23]. No variation of the monitoring LED signal has been observed within about 0.1% measurement error while switching on and off the magnet full power and when changing its polarity.

In order to monitor the HCAL stability an embedded self-calibrating scheme with ^{137}Cs gamma source has been implemented [147]. A capsule of 10 mCi activity can be transported

[21] TYVEK of type 1057D used, product of E.I. du Pont de Nemours and Company.

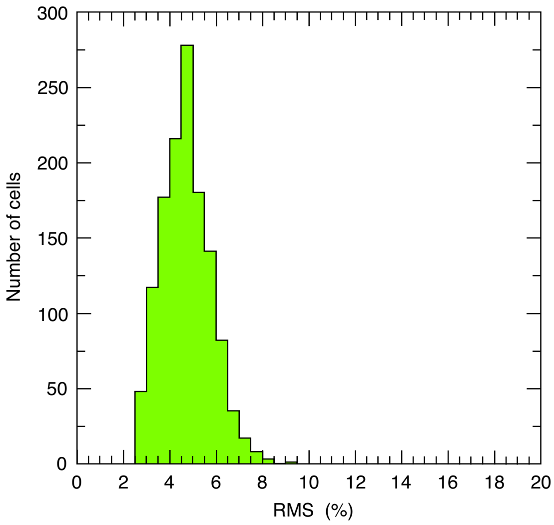

Figure 6.32: The distribution of RMS light yield for tiles read out by the same PMT.

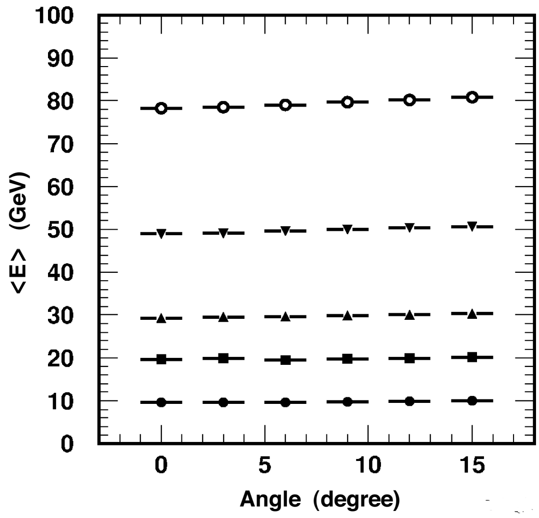

Figure 6.33: The angular dependence of the HCAL prototype response at different energies.

through a stainless steel pipe fed through all tiles. The source is encapsulated in a 2 mm diameter, 4 mm long stainless steel tube that is welded at both ends. The hydraulic driving system filled with distilled water includes a garage to store the source, and computer controlled pump and valves that allow reversal of the water flow direction. A separate readout circuit measures the integrated anode current every 5 ms resulting from the scan of a half detector when the source propagates sequentially through 26 HCAL modules with an average velocity of about 20–40 cm/s. This procedure takes less than one hour. The method was widely used both during construction and in the final test of modules before installation in the cavern. Furthermore this system is used for the absolute calibration of the HCAL in-situ.

Beam tests performed with several HCAL modules allow the correspondence between the anode current induced by the radioactive source and the measured beam particle energy to be determined. Being absolutely calibrated the HCAL provides a unique possibility to cross-check the calibration of the upstream detectors (e.g. electromagnetic calorimeter) by comparison of the average energy deposition of the hadronic shower in the corresponding cells of two detectors. The energy sharing function varies slowly over the calorimeter surface and can be extracted from the MonteCarlo simulation.

The tile response during optics assembly was monitored using the radioactive source system. A maximum deviation of 20% from the average anode current for tiles grouped to the same PMT was accepted. The tiles and fibres not satisfying this requirement have been replaced. A distribution of the RMS of tile responses within the groups coupled to the same PMT is shown in figure 6.32. The mean value of this distribution is 4.7%.

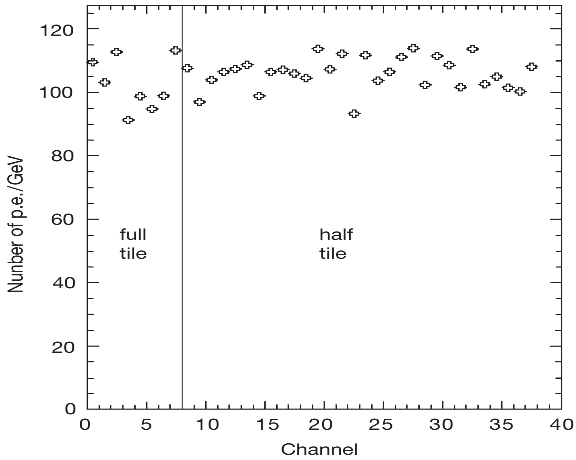

Figure 6.34: The light yield for the HCAL module measured in the test beam. The left part of the plot corresponds to 8 big cells of $26 \times 26\,\text{cm}^2$. The other 32 cells comprise half-size cells of $13 \times 13\,\text{cm}^2$.

Performance of the HCAL modules

The performance of the HCAL has been studied with prototypes [148] and continuously checked during module assembly using the CERN SPS test beam [149]. The dependence of the HCAL response on the angle of the incoming particle has been studied by rotating the detector between 0° and 15° around a vertical axis that traverses the HCAL close to the average shower maximum. Figure 6.33 shows the response of the 5.6 λ_I long prototype for pion energies between 10 GeV and 80 GeV. From a lateral scan of the particle beam across the prototype front surface the uniformity in response is measured to be well within $\pm 3\%$.

During the assembly process [150] tiles with similar properties were grouped into the same cell to minimize nonuniformities. The light yield of all cells from one typical module is shown in figure 6.34. In total five modules (out of 52) were tested in the beam with an average light yield of 105 p.e./GeV.

The moderate requirements for the HCAL energy resolution allow the ratio of the active to passive material in the detector to be as low as 0.18. Furthermore, owing to the limited space available, the length of the HCAL has been chosen at 5.6 λ_I. The upstream ECAL adds a further 1.2 λ_I. Beam-test measurements were compared in detail with results using different software packages for the simulation of the hadronic shower development. The energy response to 50 GeV pions is shown by the hatched histogram in the left-hand plot of figure 6.35. The tail towards low energies due to leakage of the shower is easily seen. However, this tail is not a concern for the hadron trigger performance since it only introduces some minor inefficiency for high E_T signal events but does not affect the rejection of low E_T minimum-bias events. The black dots show the result of a MonteCarlo simulation that is in good agreement with the data, when using the GEANT (MICAP+FLUKA) interface. The energy resolution has been determined by fitting the energy spectrum with a gaussian distribution bounded by $\pm 2.5\sigma$. The resolution extracted from a fit to the data at several energies is $\sigma_E/E = (69 \pm 5)\%/\sqrt{E} \oplus (9 \pm 2)\%$ (E in GeV) as shown in the right-hand plot of figure 6.35.

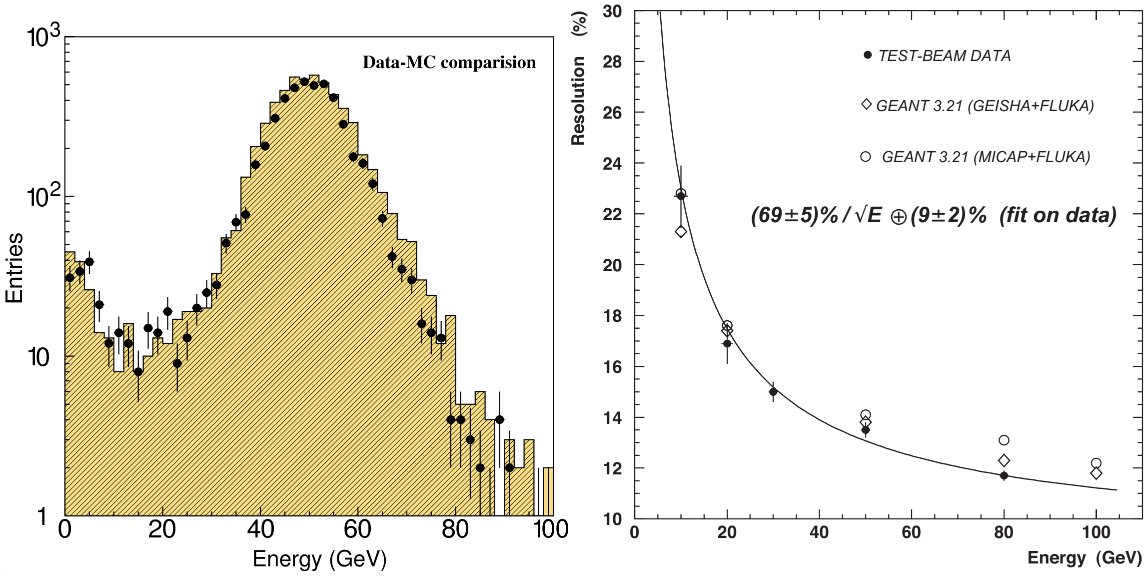

Figure 6.35: Left: energy response for 50 GeV pions from test-beam data (hatched) and from simulation (dots). Right: HCAL energy resolution, both for data and for simulation with three different hadronic simulation codes. The curve is a fit to the data.

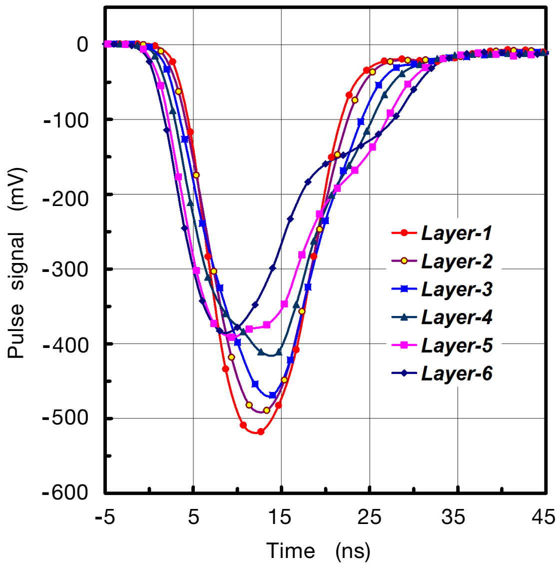

Figure 6.36: The average signal pulse shape of 30 GeV electrons in tile layers at different depths.

Another important feature of the HCAL is its signal timing properties. A precise signal shape measurement has been done with an electron beam of 30 GeV hitting layers of tiles at different depths. For this purpose the HCAL modules have been rotated by 90° and moved transversely with respect to beam line. Average pulse shapes of the detected signals are shown in figure 6.36. The variation of the shape is due to light reflection from the mirror at the end of the fibre opposite to the PMT. For layer 1, for example, the direct and reflected light reach the PMTs simultaneously, but for layer 6, closest to the PMT, the direct light reaches the photocathode earlier than the reflected one by the propagation delay in the 1.2 m long WLS fibre.

Radiation resistance of the HCAL modules

A comprehensive study of the degradation under irradiation has been performed for all optical components of the HCAL [151]. Scintillating tiles and WLS fibres have been irradiated at the IHEP 70 GeV proton synchrotron near the internal target area to get realistic environmental conditions as expected during the LHC operation. The transparency of tiles degrades by 25% after 250 kRad irradiation, but then steadily decreases by a further 20% with irradiation up to 1.4 MRad. The relative light yield after irradiation shows almost the same behaviour. Another important effect is the radiation degradation of the WLS fibres which introduces a longitudinal nonuniformity of the calorimeter response [152]. For example, the attenuation length in the WLS fibre degrades by 30% after irradiation with a dose of about 0.5 MRad, which corresponds to 10 years of operation for the most central cells of the HCAL at nominal luminosity of $2 \times 10^{32}\mathrm{cm}^{-2}\mathrm{s}^{-1}$. As a result of the same amount of irradiation, the constant term of the HCAL resolution degrades by 20%. To monitor the fibres radiation damage we intend to use the embedded calibration system with the radioactive source, that allows measurement of the response from each tile along the detector depth with a few percent accuracy.

6.2.6 Electronics of ECAL/HCAL

Because of the similarity of input signals and functionalities, it has been decided to use a common electronic system for the ECAL and HCAL. This system is based on a deadtimeless and low pedestal integrator system using delay lines, followed by ADCs and pipeline buffers. Each card is connected to 32 channels of the ECAL or the HCAL. After digitization in the front-end card the data is processed further and sent to a trigger validation card. The data is also pipelined and stored on the front-end card, and then sent through the back plane to a calorimeter readout card (CROC).

Pulse shaping and front-end chip

In order to take advantage of the inherent speed of the scintillator and WLS based calorimeter system the electronic system is capable of measuring every bunch crossing independently of signals from associated neighboring bunch crossings (pileup). The PMT pulses therefore are shaped to eliminate the small tail of pulses extending beyond 25 ns. A schematic of the PMT signal shaping and of the front-end chip is shown in figure 6.37 for HCAL. The PMT pulse is shortened by a clipping line which is a cable for the HCAL and a delay chip for the ECAL due to lack of space. The length of the line is typically one metre, giving a FWHM of about 10 ns. The resistor load at the end of the line is adjusted to obtain a return to a 0 Volt level after clipping. Due to fluctuations in the number of photoelectrons as a function of time, a fluctuation is also present in the shaped pulse. However the effect is small, especially for the ECAL where about 3000 photoelectrons produced per GeV. The pulses are then sent along 10 m of coaxial cables to the front-end cards which reside in

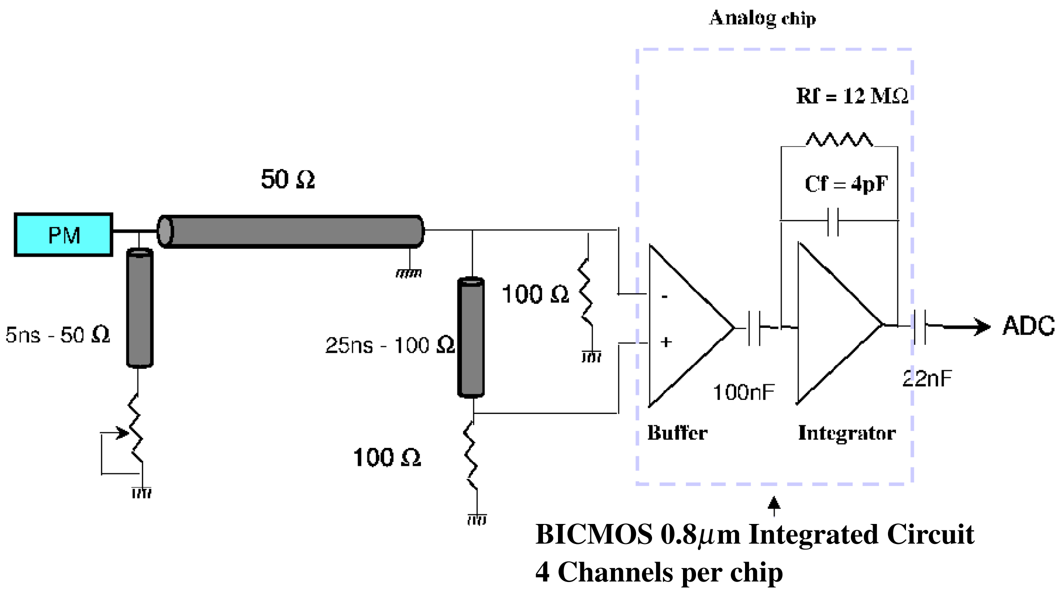

Figure 6.37: Schematic of the PM signal shaping and of the front-end chip.

crates above the calorimeters. The pulse-shape distortion produced by the cable is compensated to first order by a pole-zero circuit placed after the integrator. The first element of the pole-zero card is a front-end chip which contains a buffer amplifier and an integrator. To discharge the integrator the same pulse is subtracted in a buffer amplifier after a 25 ns delay obtained by a lumped-element delay line. Simulated input and output pulses using a 10 ns rectangular pulse are shown in figure 6.38, as well as an average 80 GeV PM HCAL pulse (averaged over 1000 measurements on a digital scope) and the resulting integrated pulse.

The schematic of the analog chip is given in figure 6.39. The circuit has been realized in AMS 0.8 μm BICMOS technology. A typical noise of 150 μV has been obtained after a 25 ns integration, which should correspond to a total noise of less than one ADC count. As measured with prototypes, the tail of the pulse integral in the next sampling is about 2% with an additional fluctuation of 1%. The impact of the amplifier noise on the physics performance is found to be negligible compared to the energy resolution of the ECAL.

The ECAL/HCAL front-end board

Figure 6.40 shows the block diagram of the 32 channel front-end board. It is a 9U board using VME mechanics with a specialized serial bus used for Experiment Control System purposes (see section 8.4). The pulses from the front-end chip, described above, are sent to 12-bit ADCs. The pulses after integration are flat (within 1%) over ± 2 ns around the maximum. To strobe at the maximum of the pulse, the different delays in the photomultipliers have to be compensated. This is achieved by adjusting the clock of each ADC by a delay chip to an accuracy of 1 ns. The digitized output of the ADCs are then resynchronized to a common clock (per card) in a register at the input of the next chip. The pulses at the integrator output can be subject to baseline shift and to the

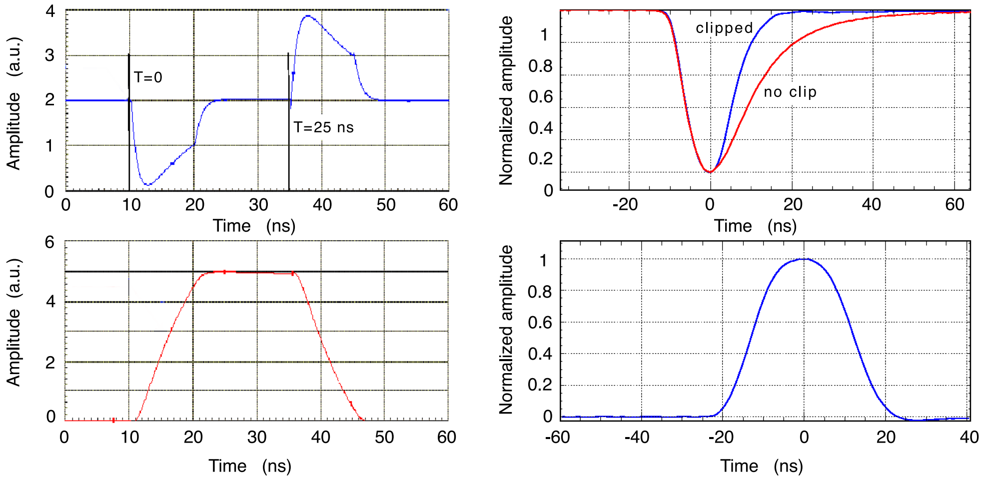

Figure 6.38: Left: simulated input pulse of a 10 ns rectangular pulse and the corresponding output pulse of the integrator: buffer output current before integration (top) and output integrated signal (bottom). Right: 80 GeV HCAL signals. The upper figure shows the PM signal with and without clipping, the lower one shows the same clipped signal at the output of the integrator.

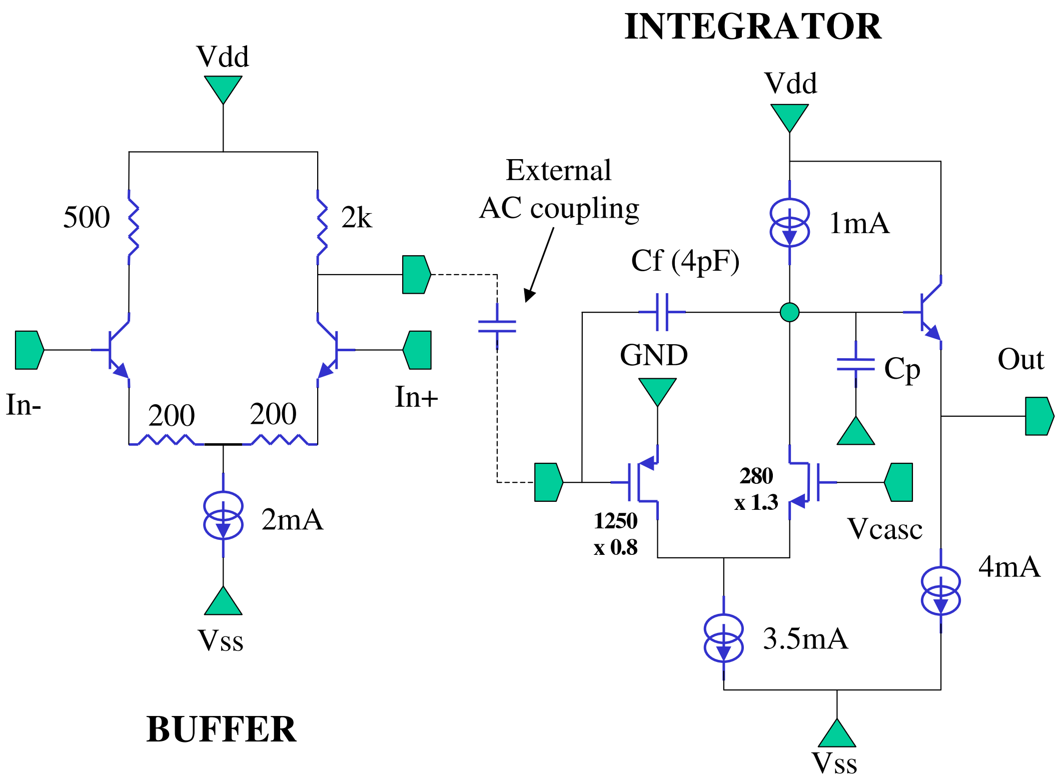

Figure 6.39: Schematic of the analog chip.

influence of low frequency pickup noise which would cause slow variation of the ADC pedestal. These variations are cancelled through a *digital differentiation* by subtracting the digitization in a

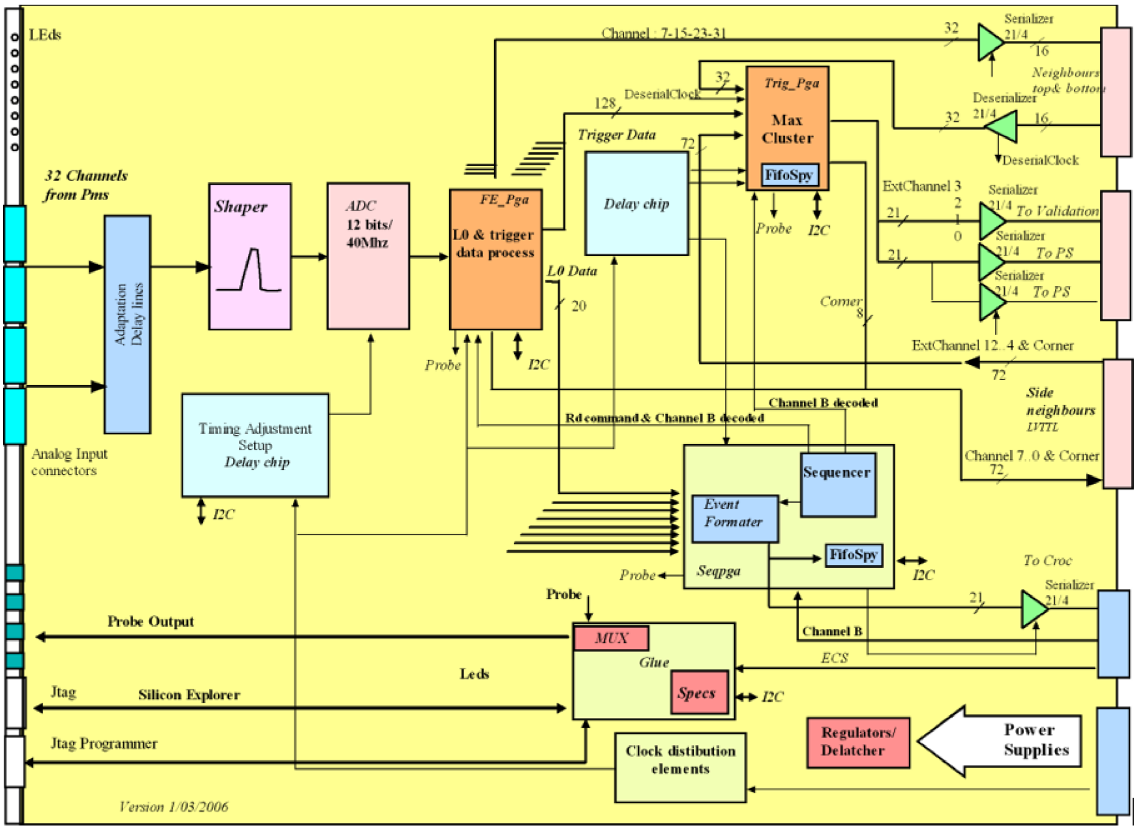

Figure 6.40: Block diagram of the front-end board, for ECAL and HCAL.

preceding sample (25 ns before). This subtraction also defines the effective integration time of the amplifier and therefore limits the integrated thermal noise from the buffer amplifier. To decrease the possibility of subtracting a signal present in the same channel, the quantity subtracted is actually the smallest of the two preceding measurements. Even at the highest occupancy, about 5%, the probability of subtracting a significant signal is therefore reduced to less than 0.25%. Simulations have shown that this procedure introduces negligible deterioration of energy and position measurements [129]. However the procedure introduces a pedestal shift of about 40% of the 40 MHz noise (i.e less then one ADC count) and an increase of the 40 MHz noise by 16%. The subtraction of the smallest of the two preceding samples is performed in 8 dedicated anti-fuse based FPGAs (cf. section 7.1.3) [22] called FE-PGAs, each of these being used to process four ADC channels [153]. Actually each FE-PGA has, for each ADC channel, four functional blocks. The first one processes the input ADC data, as described above. The second block produces the trigger data, converting the 12 bits of the ADC to 8 bits by a simplified multiplier with an adjustable 8 bits calibration constant. The third block is in charge of storing the data (12 ADC bits and 8 trigger bits per ADC, 80 bits per FE-PGA), during the L0 latency, and upon L0-Yes store again the data in a derandomizer and send them as four successive groups of 20 bits to the SEQ-PGA. The last block of the FE-PGA permits injecting test values at the input, in place of the ADC values, in order to check the proper behaviour of the card.

[22] AX250 anti-fuse PGA from ACTEL.

To adjust the timing of the clock signals used to strobe the ADCs and to synchronize the PGAs, delay-chip modules are used. These delay chips are custom made ASICs which shift the 40 MHz clock sent by the crate controller, the CROC. The delay-chips' clock shifts have a 25 ns range and steps of 1 ns.

Three other PGAs are used on the board for specific functions: The Trig-PGA is used to process the 8 bits trigger data from each of the 32 channels of a board together with the 8 side-neighbours channels from adjacent boards 4 top neighbours and one corner neighbour from other crates. The Trig-PGA computes the total transverse energy of the board and the information on the 2X2 cluster of cells with the highest transverse energy. This information is then passed to further boards involved in the trigger decision (the PS/SPD FE Board and the Trigger Validation Board). The Trig-PGA is implemented in an anti-fuse AX500 from ACTEL. The SEQ-PGA, mentioned above, serializes the 32 channels of the front-end board and sends them to the readout controller, the CROC. It also dispatches the L0 trigger signals and control signals linked to the trigger, the so-called *channel B*, to the FE-PGAs. The Glue-PGA is an interface between the Experiment Control System (based on the SPECS system) and the other PGAs of the board. It allows to load and read back *constant* parameters which adjust the delay chip values, calibration constants in FE-PGAs and so on. The SEQ and Glue PGAs are implemented in reprogrammable flash-based PGAs from ACTEL the APA300 and APA150.

The calorimeter readout card (CROC)

The CROC (for a conceptual design see [129]) is the board, which gathers the front-end L0 data of a calorimeter crate and sends them through optical fibres to the LHCb DAQ system (the TELL1 boards). Each of the 26 crates housing up to 16 ECAL, HCAL or PS/SPD front-end boards, are equipped with one single CROC, plugged into the central slot. The CROC also provides the clock, trigger signal, broadcast (channel B) and slow control command for all boards of a crate. In the DAQ path the data from front-end boards, which has been serialized at a 280 Mbits/s rate and sent through the backplane, are first deserialized and then captured and resynchronized in 4 FE-PGAs. These FE-PGAs (APA300) detect the presence of data (header detection) and add to the 21 bits of data coming from front-end boards 11 bits providing the data type and the board and crate identification numbers. The data are then sent to 2 GOL mezzanines each equipped with 8 fibres. In the absence of data the FE-PGAs send a special signal used to periodically synchronize the fibres drivers and receivers in the TELL1 boards. A spy functionality is also implemented in the FE-PGAs where data for up to 15 L0 events can be copied into RAMs. The data are then collected by a dedicated Spy-PGA based on an APA450. These dcalorimeter system is inherently fast, it has been decided to ata can be read at a slow rate using a slave mezzanine of the SPECS ECS system, which is mounted on the CROC board. The SPECS mezzanine also loads and reads control data onto the board, and also sends through the backplane, ECS data to the Glue-PGAs of each front-end board which are programmed to act as SPECS slaves. Finally a TTCrx mezzanine mounted on the CROC board receives by a fiber the 40 MHz clock, the L0 trigger signal and the channel B signals which have been generated in the readout supervisor boards in the electronic barracks. These signals are buffered and sent through the backplane to each other board in the crate. For debugging purposes the CROC can work as a stand alone system locally generating the clock L0 and channel B signals.

Calorimeter specific TELL1 features

The TELL1 boards of LHCb are described in section 8.2. The specifications of the calorimeters are described in [154].

A preprocessor FPGA (PP-FPGA) collects and treats the incoming data from front-end boards sent by the CROC to the TELL1 board through an optical receiver mezzanine card (O-Rx card) which ensures the optical to electrical conversion and data synchronization. The PP-FPGA treats the event according to the detector identification (ECAL/HCAL or PS/SPD). Inside each PP-FPGA, a zero suppression is performed on the events during physics runs for PS/SPD data and a data compression without loss of information for ECAL and HCAL data [155]. The output data of each PP-FPGA are collected by the SyncLink-FPGA which then packs them in a Multiple Event Packet (MEP). For each event, the SyncLink-FPGA gives the trigger type of the run (physics or calibration) to the PP-FPGA. The MEPs are sent to the DAQ through a Gigabit-Ethernet (GBE) card. The output bandwidth of the GBE limits the use of one among the two O-Rx cards for ECAL and HCAL and thus two PP-FPGAs among the four. The two O-Rx cards are used for PS/SPD. In case of no data and/or synchronization error from the optical input links in the O-Rx card, an error bank is optionally generated (it is suppressed by default due to bandwidth limit). In order to keep track of these errors, a minimal information is kept in each event header.

The LED monitoring system is described in section 6.2.8. During calibration runs the LED data are not affected by the zero suppression, and only non-zero values are kept for PS/SPD. During physics runs, the data coming from the PIN boards (FE boards devoted to the PIN diode signals of ECAL/HCAL) are ignored.

6.2.7 Electronics of PS and SPD detectors

The signal of the PS and SPD has about the same duration as the ECAL and HCAL pulses; on average 85% of the charge is obtained in 25 ns. However, since the average number of photoelectrons is only about 25 per MIP, there are very large fluctuations in the signal pulse shape [156]. It was therefore considered unreasonable to try to implement the delay-line pulse shaping used for the ECAL/HCAL. On the other hand, since the useful dynamic range of the PS is typically only from 1 MIP to 100 MIP, an ADC with only 10-bits can be used and pedestal stability is not as important as for the ECAL/HCAL electronics, although it is important to integrate the signal over a time as long as possible within the 25 ns limitations. The phototube chosen to detect the light from the PS and SPD fibres is a 64 channel multi-anode PM. The HV is common to all 64 channels and there is a nonadjustable gain dispersion among these channels of a factor of 3, which however is constant in time. For this reason it was decided to introduce a Very Front End (VFE) stage of integration on the back of the phototubes in order to compensate the gain variation using a digital correction of a factor up to 2 in the front-end electronics.

The PS very front-end design

The solution adopted for the PS is to alternate every 25 ns between two integrators and to reset one integrator when the other one is active. The signal is sampled by track-and-hold circuits and the output of the active integrator is chosen by a multiplexer, followed by a twisted-pair cable driver.

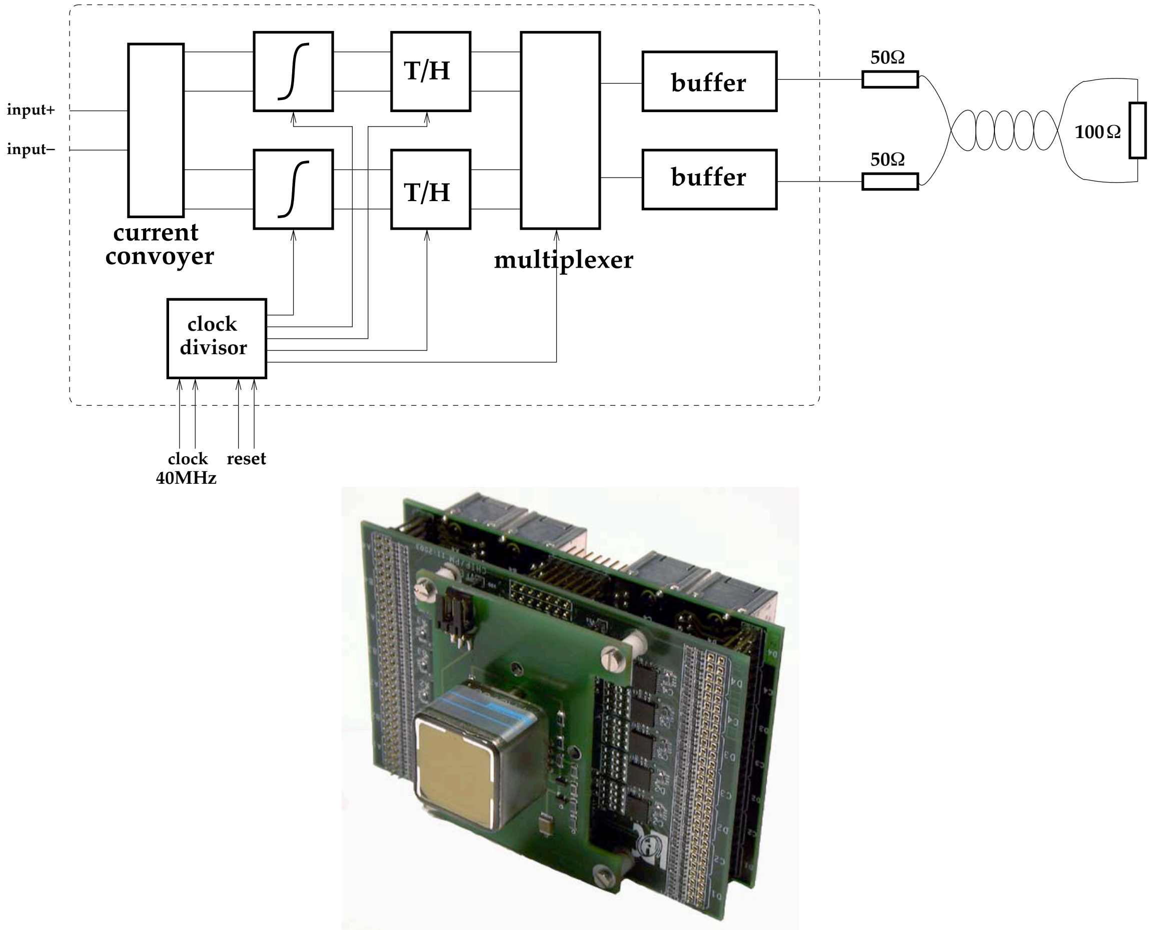

Figure 6.41: Schematic of the PS *Very Front-End* integrator (top) and a photograph of the integrator card mounted behind the MAPMT (bottom).

All circuit elements are functioning in differential mode to improve stability and pickup-noise rejection. The circuit design is shown in figure 6.41 and its detailed description is given in [157]. The phasing of the clock with respect to the signal determines the start of the integration. Since the length of the 64 fibres connected to a given PM are identical and the delay inside the PM is identical within a fraction of 1 ns, it is sufficient to have one clock adjustment (in steps of 1 ns) per phototube. The amplifier integrator circuit is realized in monolithic AMS 0.8 μm BICMOS technology with 4 channels implemented per chip. The dynamic range is 1 Volt with a noise of 1 mV. Sixteen chips are grouped in a card on each phototube. The outputs of each chip (4 channels) are sent through 27 m long ethernet cables[23] with RJ45 connectors to the ADC located on the FE board. Two clock and two reset signals delivered by the corresponding FE board are received by the VFE board through a cable of the same type as those used for the signal.

[23] from Kerpen company, Geramny.

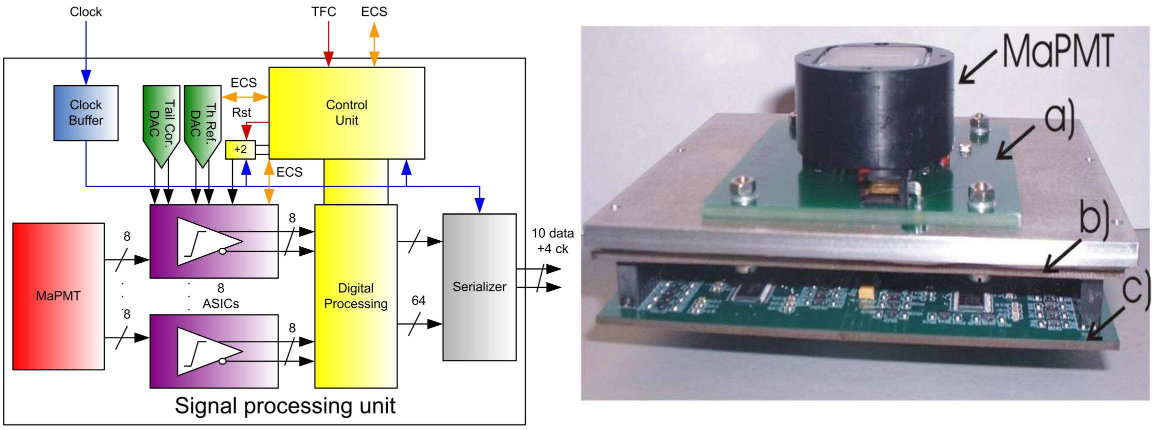

Figure 6.42: Left: block diagram of the SPD VFE card. Right: picture of the VFE assembly where the components are a) PMT base board, b) ASICs board and c) FPGA board.

The SPD very front-end and control board design

The SPD function is to discriminate between charged particles and neutrals in a detector which matches the preshower and ECAL cell size. The SPD signals are obtained, as in the case of the PS, from 64 channel multianode photomultipliers. The main difference of specification is that there is no compelling reason to perform pulseheight analysis on SPD signals. It was therefore decided to use a simpler solution with a simple discriminator output and a threshold set at 0.5 MIP thus obtaining 98% efficiency on charged particles [131, 137]. The principle of the design is shown in figure 6.42 and described in [127]. Although the functional architecture of a signal processing channel is similar to that of the PS, the circuits have been designed for the SPD specifically [158, 159]. The main architectural difference is the inclusion of an on chip pile-up compensation system and a comparator. The pile-up compensation system takes a tunable fraction of the integrator output at the current period and stores it on a track and hold circuit. This cancels on average the charge delivered by a pulse in the time interval between 25 and 50 ns after its start. The reference threshold value is set by a 7-bit DAC. The integration of each channel uses an independent DAC to compensate the offsets and the gain nonuniformity of the PMT. The circuit is realized in the AMS BICMOS 0.8 μm technology with 8 channels per chip. There are two external (not on-chip) DAC, with I2C interface to set some analogue references for the signal processing part. The control unit, the digital processing and clock divider used to obtain the 20 MHz clock that controls the ASICs are implemented in a reprogrammable FPGA, the ProASIC Plus ACTEL APA300. Triple voting registers (TVRs) are used to minimize signal event upset (SEU) errors. The digital processing consists of mapping PMT channels to given serializer channels to match the PS and SPD detector cell and injecting arbitrary patterns to test the detector data flow. The 64 channels and the 20 MHz clock are sent via standard shielded twisted pair (SSTP) LAN cables to the PS/SPD FE board, by means of 4 serializer chips (DS90CR215) with 3 data pairs and 1 clock pair each, requiring a serializing factor of 7. Control boards provide the VFE cards with links to the ECS and the timing and fast control (TFC) system. The boards are located in the FE crates. Two boards are needed for each of the 8 crates corresponding to the PS/SPD subsystem.

The PS/SPD front-end board

The PS/SPD front-end boards implement functions similar to the HCAL/ECAL boards i.e an ADC for the preshower signal, pedestal correction and gain calibration, preparation of the trigger information, pipeline storage and selection of data for readout upon reception of trigger signals. The PS/SPD board handles 64 PS data channels for raw data readout and trigger purposes, and 64 SPD single bit trigger channels. The PS raw data dynamic range corresponds to 10 bits, coding energy from 0.1 MIP(1 ADC count) to 100 MIPs. A general overview of the board is given in figure 6.43 for the PS. An identical board is used for the SPD. Its general architecture is similar to the ECAL/HCAL boards with five major components:

- An analog block receiving the 64 analog PS channels from the VFE part and digitizing them. Each channel is composed of a fully differential operational amplifier followed by a 10-bit 40 MHz differential ADC. A synchronization signal (clock and reset) is sent to the VFE.
- A processing block made of 8 identical FE PGAs. Each of them is in charge of processing 8 PS channels. After applying corrections for pedestal subtraction, gain adjustment and pile-up, the 10-bit data are coded into an 8-bit floating format. A trigger bit is produced for each channel by applying a threshold on the corrected data. Eight SPD channels are also received. Two PS and SPD channels are packed together, stored and retrieved after L0. Two blocks of memory per two channels are used in each FE PGA for the L0 pipeline and derandomizer. The processing block is very resource consuming. Since the VFE comprises two interleaved integrators working in alternance, the gain and offset corrections have to be applied differently for two consecutive events leading to two effective subchannels per physical channel. Also the data inputs, 8 SPD channels of 1-bit and 8 PS channels of 10 bits are important. Consequently, the FE PGA chosen was the AX1000 of the ACTEL anti-fuse technology.
- A trigger block made of one Trig-PGA. It handles the processing for the production of the L0 information. The block receives the address of each cell and its local maximum of transverse energy from the ECAL Front End Board (FEB). As the ECAL electronics is organized into 32 channel boards, each 64 channel PS/SPD FEB is seen by the system as two 32 channel half boards, each receiving its own request address. The Trig-PGA is an APA450 of the ACTEL ProASIC plus Flash based FPGA family.
- A SEQ PGA builds the data block after a L0-Yes signal, and sends it to the CROC. It also issues control and synchronization signals for the other 8 FE PGAs and the Trig-PGA.
- A SPECS slave called GLUE PGA handling all the I2C communication of the board. The last two blocks, SEQ PGA and GLUE PGA, are identical to the ones of the ECAL/HCAL FE electronics and are described in reference [128].

All registers holding permanent information are radiation protected in static mode by triple voting and, during data transfers, by Hamming code.

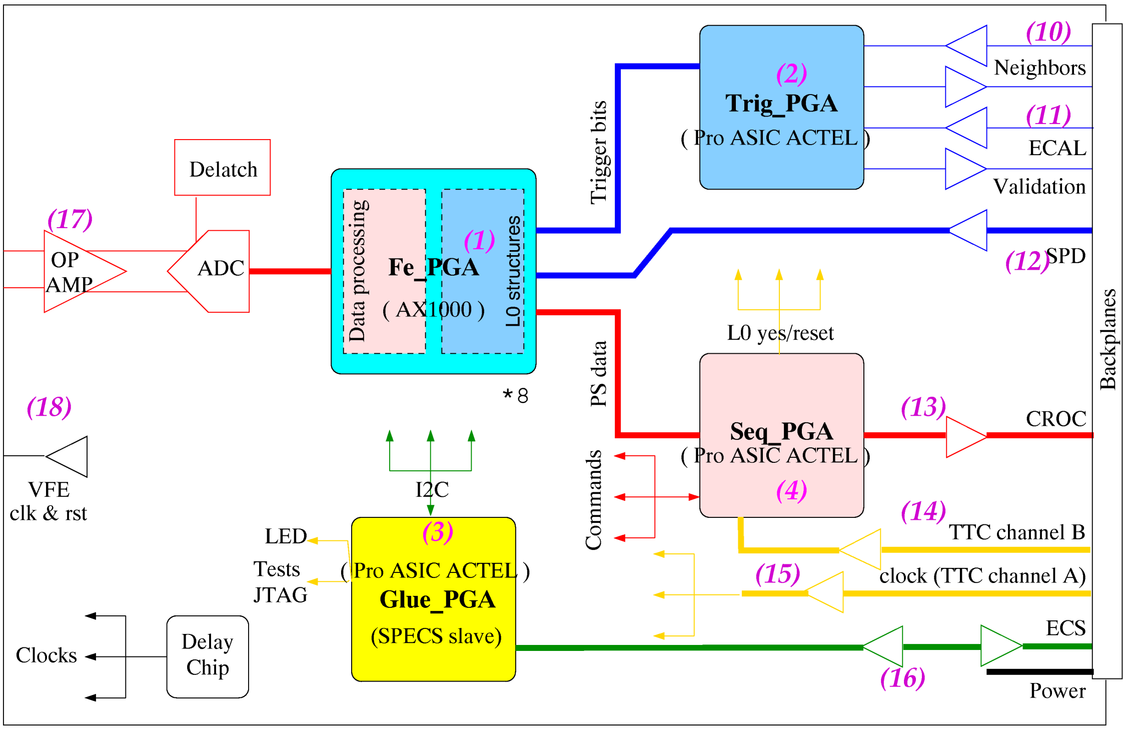

Figure 6.43: Schematic of the front-end board for the PS.

6.2.8 Monitoring and high voltage system

The calorimeter High Voltage (HV) and LED light intensity control systems share a common control board, the HV-LED-DAC board, that interfaces them to the Experiment Control System (ECS).

The High Voltage system

All calorimeter subdetectors are equipped with Hamamatsu photomultipliers. Eight thousand R7899-20 tubes are used for ECAL and HCAL and two hundred 64 channels multi-anode R7600-00-M64 for the SPD/PS detectors. All PMTs passed quality checks on dedicated test benches before installation on the detectors. The quality requirements included a better than 5% linearity and better than 3% gain stability as a function of rate, a low dark current and, for the SPD/PS PMTs, pixel-to-pixel uniformity of better than 1 to 3 (minimum to maximum) and crosstalk of less than 2%.

The HV system for the PMTs (figure 6.44) is based on a Cockroft-Walton (CW) voltage converter located on the base of each PMT and controlled by HV-LED-DAC control boards located in a few boxes distributed over the detector periphery and connected to the (ECS) by a SPECS [160] serial bus. For the SPD and PS the CWs and control boards are located in a VME crate on top of the ECAL and the HV is distributed to the PMTs with cables. The maximum HV is 1500 V for ECAL and HCAL and 800 V for SPD and PS. The CW base [161] is a reoptimized and radiation hard version of the one used in the HERA-B experiment [162]. It is implemented on a 25 mm x 60 mm CW board and consists of 22 multiplication stages, a control operational amplifier, an

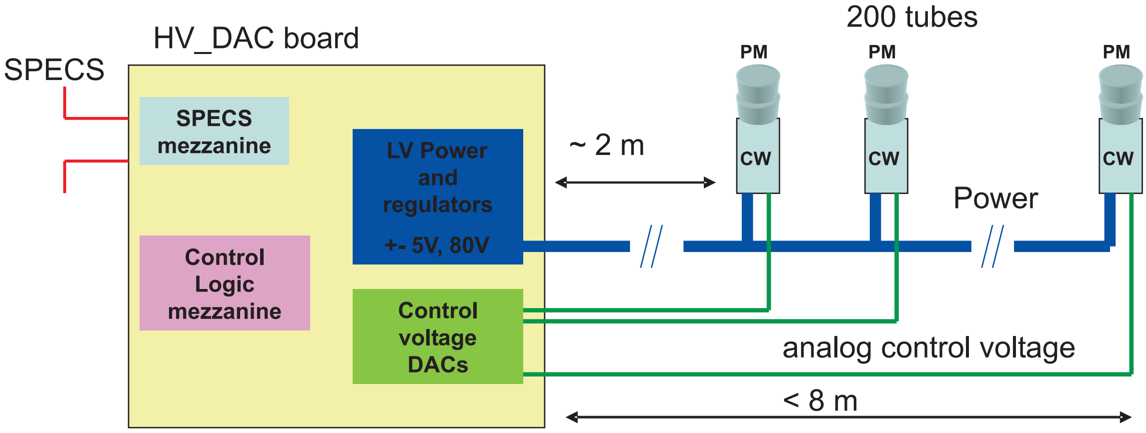

Figure 6.44: An overview of the High Voltage system of the calorimeter.

oscillator of 50 kHz and fast transistor switches. It features individual and precise gain adjustment of each PMT, effective operation at high background anode current, low power dissipation and only low voltage ($\pm$ 6V) power supplies. It requires, in addition, 100 V which is converted locally to a high voltage in the 100–2000 V range selectable through a 0 to 5V control voltage supplied by the control board. This conversion, being made locally for ECAL and HCAL, minimizes the number of high voltage cables and connectors. The characteristics of the CW are a gain drop of less than 2% for anode currents as high as 12 μA, a voltage ripple of less than 200 mV, a spread of output voltages of about 1% and a power consumption of less than 130 mW. Each HV-LED-DAC board can control 200 CWs and consists of a mother board and four mezzanine cards. A SPECS slave mezzanine is used for interconnection to the ECS system. The 200 PMTs are controlled by five 40-channel HV control signal generating cards using 12-bit DAC integrated circuits. A control logic board equipped with a radiation tolerant FPGA ACTEL APA075 provides an interface between the ECS and the 200 DAC signal generating integrated circuits. This board also allows automated monitoring and ramp-up of the high voltage. The fourth mezzanine card generates a 16 channel LED intensity control signal.

The LED monitoring system

The energy calibration of each cell of the ECAL calorimeter is obtained during data-taking by a variety of methods, such as monitoring their response to electrons, π^0's and minimum ionizing particles. ECAL and HCAL stability is monitored using LEDs, in order to obtain the best energy resolution essential for both triggering and reconstruction issues. The concept of the sytem is outlined in figure 6.45. Each cell of the four subdetectors is illuminated by an LED. They are triggered by LED drivers (labeled LED in figure 6.45) and their intensity controlled by the HV-LED-DAC boards. Multichannel LED Trigger Signal Boards (LEDTSB) perform the overall control and adjust the timing. For SPD and PS an individual LED is located on each tile and illuminates the PMT through the scintillator. Groups of 16 LEDs are controlled by 770 LED drivers located on the supermodules which are fired by 100 trigger channels.

On ECAL, LEDs are located in light-tight boxes situated above and below the calorimeter.

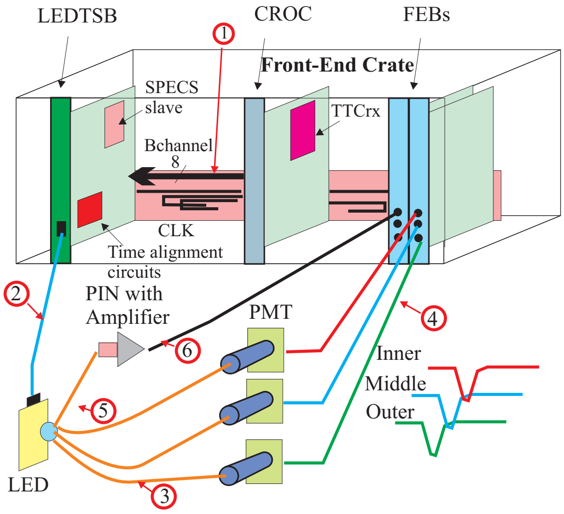

Figure 6.45: A sketch of the LED monitoring of the calorimeter.1: FE crate backplane over which the monitoring trigger request is transmitted, 2: LED trigger pulse cable, 3: Clear fibre to cell, 4: PMT signal cable, 5: Clear fibre to PIN diode, 6: PIN signal cable.

Each LED illuminates 9 or 16 cells via clear fibres routing the light to a connector at the front of each cell, and from there via a second clear fibre traversing the module and conducting the light directly through the light mixer to the PMT. Each LED also illuminates a PIN diode for monitoring the stability of the LED light output. There are 456 LEDs, each controlled by the LED driver, and 124 PIN diodes so that the LEDs sharing a PIN can be fired at different times.

Each HCAL module is equipped with two LEDs each illuminating every cell in the module. Since the PMTs in a module have different gains, which depend on the average momentum of the particles they are detecting, the light output of the two LEDs is set in the ratio of 1:4. Clear fibres bring the light of both LEDs to each PMT via its light mixer. One PIN diode monitors the stability of each LED. The 2 LEDs in each of the 52 modules illuminate 16 or 40 cells and are controlled by 104 LED drivers.

A LED monitoring sequence is initiated by the Readout Supervisor (RS) upon request and transmitted to the LEDTSBs via the CROCs and the FE crate backplane. The LEDTSBs are located in the front-end crates on the calorimeter platforms and each controls 64 LED drivers. A total of 686 LED drivers in the system therefore require 12 LEDTSBs. A correspondence between LEDs or groups of LEDs fired by each LEDTSB is preprogrammed in the LEDTSB FPGA. This allows a different pattern of the 64 drivers to be fired in each of 64 consecutive triggering sequences, thus providing maximum flexibility. The LED firing time is adjusted in the LEDTSB in steps of 1 ns so as to arrive at the first cell of the readout pipeline, 16 clock cycles (400 ns) after the RS pulse. It emerges 4 μs later from the pipeline in time for the calorimeter trigger.

The LED trigger boards are decoupled with air transformer, are edge triggered, and use fast on board pulse shapers. They provide a pulse of less than 25 ns to fit within an LHC bucket and with a shape compatible with that generated by a particle.

The light intensity of the LEDs is controlled via ECS by the HV-LED-DAC boards which are located in areas of low radiation. A wide range of intensities is implemented to monitor the linearity of the PMTs.

2008 JINST 3 S08005

For each LED monitoring sequence a subset of each of the subdetectors is illuminated. A given group of channels is fired at a rate of 20–30 Hz, resulting in an overall monitoring rate of 1 kHz. For each trigger 3–5% of the channels contain data.

These data are read out and transferred to a monitoring farm, consisting of a dedicated node of the processing farm where they are analyzed to check the stability of the calorimeters. Should any channel be observed to be drifting in gain an alarm is generated. Depending on the type of alarm, the run is paused or a suitable correction to the HV computed and applied via the ECS system.

The LED system is also used to detect malfunctioning cells and bad cable connections. It also allows a first relative timing of the cells.

6.3 Muon System

Muon triggering and offline muon identification are fundamental requirements of the LHCb experiment. Muons are present in the final states of many CP-sensitive B decays, in particular the two *gold-plated* decays, $\mathrm{B}_\mathrm{d}^0 \to \mathrm{J}/\psi(\mu^+\mu^-)\mathrm{K}_\mathrm{S}^0$ and $\mathrm{B}_\mathrm{s}^0 \to \mathrm{J}/\psi(\mu^+\mu^-)\phi$ [2]. They play a major role in CP asymmetry and oscillation measurements, since muons from semi-leptonic b decays provide a tag of the initial state flavor of the accompanying neutral B mesons. In addition, the study of rare B decays such as the flavour-changing neutral current decay, $\mathrm{B}_\mathrm{s}^0 \to \mu^+\mu^-$, may reveal new physics beyond the Standard Model [163].

The muon system provides fast information for the high-p_T muon trigger at the earliest level (Level-0) and muon identification for the high-level trigger (HLT) and offline analysis.

6.3.1 Overview

The muon system [164–166], shown in figure 6.46, is composed of five stations (M1-M5) of rectangular shape, placed along the beam axis. The full system comprises 1380 chambers and covers a total area of 435 m^2. The inner and outer angular acceptances of the muon system are 20 (16) mrad and 306 (258) mrad in the bending (non-bending) plane respectively. This results in an acceptance of about 20% for muons from inclusive b semileptonic decays.

Stations M2 to M5 are placed downstream the calorimeters and are interleaved with iron absorbers 80 cm thick to select penetrating muons. The minimum momentum of a muon to cross the five stations is approximately 6 GeV/c since the total absorber thickness, including the calorimeters, is approximately 20 interaction lengths. Station M1 is placed in front of the calorimeters and is used to improve the p_T measurement in the trigger. The geometry of the five stations is projective, meaning that all their transverse dimensions scale with the distance from the interaction point.

The detectors provide space point measurements of the tracks, providing binary (yes/no) information to the trigger processor (see section 7.1) and to the DAQ. The information is obtained by partitioning the detector into rectangular *logical pads* whose dimensions define the x, y resolution.

The muon trigger is based on stand-alone muon track reconstruction and p_T measurement and requires aligned hits in all five stations. Stations M1–M3 have a high spatial resolution along the x coordinate (bending plane). They are used to define the track direction and to calculate the p_T of the candidate muon with a resolution of 20%. Stations M4 and M5 have a limited spatial resolution, their main purpose being the identification of penetrating particles.

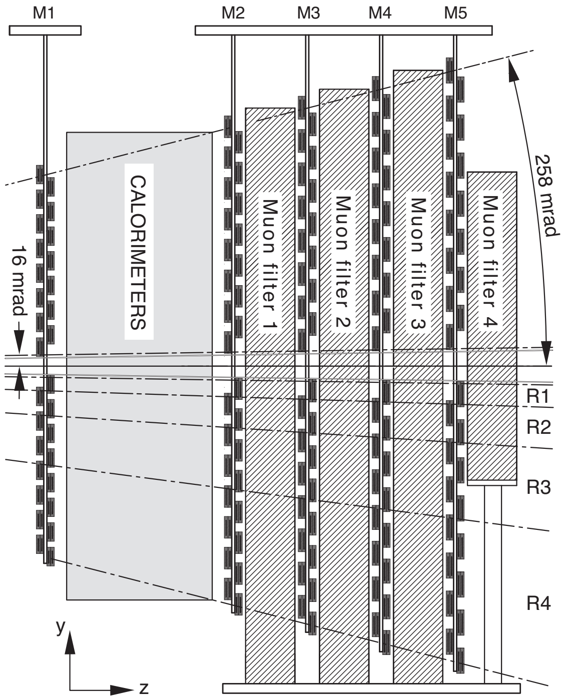

Figure 6.46: Side view of the muon system.

Appropriate programming of the L0 processing unit (see section 7.1.2) allows the muon trigger to operate in the absence of one station (M1, M4 or M5) or with missing chamber parts, although with degraded performance (worse p_T resolution).

The layout of the muon stations is shown in figure 6.47. Each Muon Station is divided into four regions, R1 to R4 with increasing distance from the beam axis. The linear dimensions of the regions R1, R2, R3, R4, and their segmentations scale in the ratio 1:2:4:8. With this geometry, the particle flux and channel occupancy are expected to be roughly the same over the four regions of a given station. The (x,y) spatial resolution worsens far from the beam axis, where it is in any case limited by the increase of multiple scattering at large angles. The right part of figure 6.47 shows schematically the partitioning of the station M1 into logical pads and the (x,y) granularity. Table 6.5 gives detailed information on the geometry of the muon stations.

Simulation

A complete simulation of the muon system was performed using GEANT4. Starting from the energy deposits of charged particles in the sensitive volumes, the detector signals were created and digitized taking into account detector effects such as efficiency, cross-talk, and dead time as well as effects arising from pile-up and spill-over of events occurring in previous bunch crossings [167].

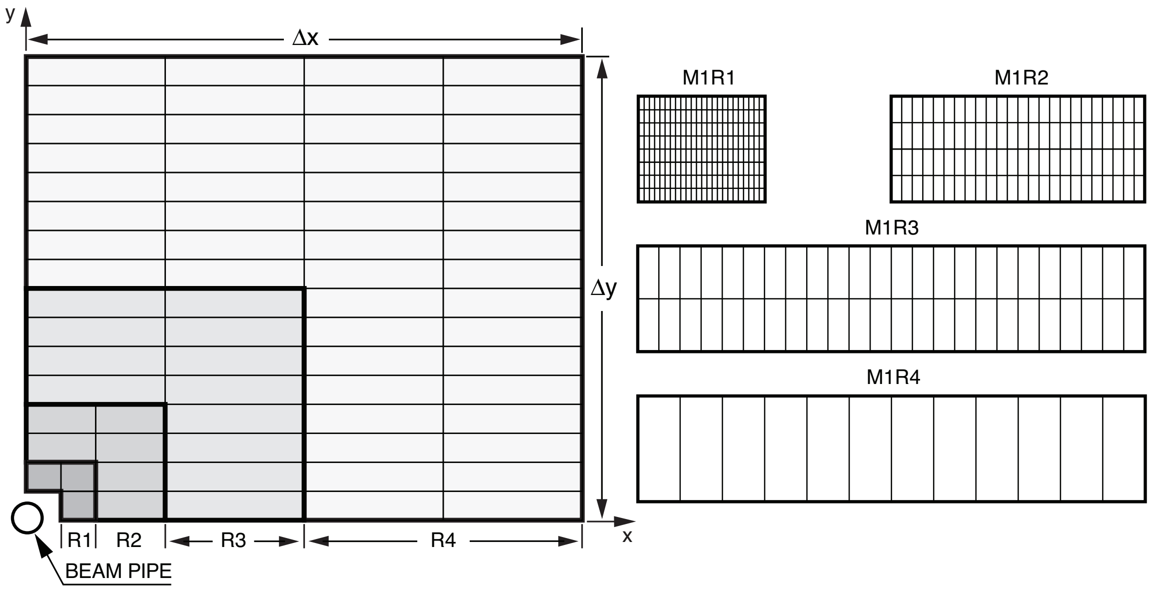

Figure 6.47: Left: front view of a quadrant of a muon station. Each rectangle represents one chamber. Each station contains 276 chambers. Right: division into logical pads of four chambers belonging to the four regions of station M1. In each region of stations M2-M3 (M4-M5) the number of pad columns per chamber is double (half) the number in the corresponding region of station M1, while the number of pad rows per chamber is the same (see table 6.5).

A realistic simulation of the detector occupancy requires the detailed description of the cavern geometry and of the beam line elements and the use of very low energy thresholds in GEANT4. The CPU time needed for such a simulation would be prohibitive for the stations M2–M5 interleaved with iron filters. The strategy chosen to overcome this problem was therefore to generate once for all a high statistics run of minimum bias events with low thresholds. The distributions of hit multiplicities obtained were parametrized and then used to statistically add hits to the standard LHCb simulated events. The latter were obtained by running GEANT4 at higher thresholds and with a simplified geometry of the cavern and the beam line [168]. Simulated events have been extensively used to evaluate the rates in the various detector regions in order to establish the required rate capabilities and ageing properties of the chambers and to evaluate the data flow through the DAQ system [169]. At a luminosity of 2×10^{32} cm^{-2} s^{-1} the highest rates expected in the inner regions of M1 and M2 are respectively 80 kHz/cm^2 and 13 kHz/cm^2 per detector plane. In the detector design studies, a safety factor of 2 was applied to the M1 hit multiplicity and the low energy background in stations M2-M5 has been conservatively multiplied by a factor of 5 to account for uncertainties in the simulation.

Detector technology

The LHC bunch crossing rate of 40 MHz and the intense flux of particles in the muon system [169] impose stringent requirements on the efficiency, time resolution, rate capability and ageing characteristics of the detectors, as well as on the speed and radiation resistance of the electronics.

Table 6.5: Basic information for the five stations M1–M5 and the four regions R1–R4. All dimensions in cm. z: distance of the stations from the IP; Δx and Δy: dimensions of a quadrant in each station (see figure 6.47). Rows R1-R4: granularity of the different regions of the muon detector as seen by trigger and DAQ. Number of logical pads per chamber (in brackets) and size of the logical pads, along x and y. In parentheses: size of the logical pads projected onto station M1.

	M1	M2	M3	M4	M5
z	1210	1527	1647	1767	1887
Δx	384	480	518	556	594
Δy	320	400	432	464	495
R1	$[24 \times 8]$ 1×2.5	$[48 \times 8]$ 0.63×3.1 (0.5×2.5)	$[48 \times 8]$ 0.67×3.4 (0.5×2.5)	$[12 \times 8]$ 2.9×3.6 (2×2.5)	$[12 \times 8]$ 3.1×3.9 (2×2.5)
R2	$[24 \times 4]$ 2×5	$[48 \times 4]$ 1.25×6.3 (1×5)	$[48 \times 4]$ 1.35×6.8 (1×5)	$[12 \times 4]$ 5.8×7.3 (4×5)	$[12 \times 4]$ 6.2×7.7 (4×5)
R3	$[24 \times 2]$ 4×10	$[48 \times 2]$ 2.5×12.5 (2×10)	$[48 \times 2]$ 2.7×13.5 (2×10)	$[12 \times 2]$ 11.6×14.5 (8×10)	$[12 \times 2]$ 12.4×15.5 (8×10)
R4	$[12 \times 1]$ 8×20	$[24 \times 1]$ 5×25 (4×20)	$[24 \times 1]$ 5.4×27 (4×20)	$[6 \times 1]$ 23.1×29 (16×20)	$[6 \times 1]$ 24.8×30.9 (16×20)

Multi-wire proportional chambers (MWPC) are used for all regions except the inner region of station M1 where the expected particle rate exceeds safety limits for ageing. In this region triple-GEM detectors are used [166].

The trigger algorithm requires a five-fold coincidence between all the stations, therefore the efficiency of each station must be high enough to obtain a trigger efficiency of at least 95%, within a time window smaller than 25 ns in order to unambiguously identify the bunch crossing.[24] The necessary time resolution is ensured by a fast gas mixture and an optimized charge-collection geometry both for the MWPC and the GEM detectors. Moreover, the chambers are composed of four or two OR-ed *gas gaps* depending on station. In stations M2–M5 the MWPCs are composed of four gas gaps arranged in two sensitive layers with independent readout. In station M1 the chambers have only two gas gaps to minimize the material in front of the electromagnetic calorimeter. In region M1R1 two superimposed GEM chambers connected in OR are used.

To simplify the synchronization procedure and improve time alignment, the readout electronics is equipped with a 4-bit TDC which allows a fine time measurement of the signals with respect to the 25 ns machine clock. The fine time tuning is perfomed by selecting the hits belonging to penetrating tracks.

In addition, the use of two layers with independent HV supplies and the flexibility of the readout provide a high degree of redundancy built into the system.

[24]In the following, the system has been characterized assuming a conservative 20 ns window.

Table 6.6: Readout methods used in the muon chambers.

Readout type	Region
MWPC	
Wire pads	R4
Mixed wire-cathode pads	R1-R2 in M2-M3
Cathode pads	everywhere else
GEM	
Anode pads	M1R1

Readout

To satisfy the requirements of spatial resolution and rate capability that vary strongly over the detectors, different technical solutions are employed for the MWPC in different stations and regions.

All the chambers are segmented into *physical pads*: anode wire pads or cathode pads in the MWPCs and anode pads in the GEM chambers. Each physical pad is read out by one front-end (FE) electronics channel. The FE electronics is based on custom radiation-hard chips especially developed for the muon system. The input stage can be wired to handle either signal polarity: negative for anode pads, positive for cathode pads.

The electronics includes flexible logical units performing the OR of a variable number of FE channels following the requirements of the readout. The readout methods used in different detector regions are summarized in table 6.6.

The R4 regions contain most of the chambers and the spatial resolution required there is relatively modest. Therefore the simplest and safest technology was adopted: the physical pads are a group of adjacent wires connected together to the same FE channel. The length of the anode wires defines the spatial y resolution, all the wires being aligned vertically. The requirement on the resolution limits the vertical size of the chambers to $20--30\,$cm, and results in a large number of chambers.

Cathode pads (anode pads for GEM) are obtained by etching the desired pattern in the cathode (anode) planes. As can be seen from figure 6.47 all pads in R3 chambers can be accessed directly from the upper and lower sides. On the other hand, the chambers belonging to R1 and R2 have a chessboard pad structure so that a multilayer printed circuit board is used to bring the signals outside.

To keep the noise and the dead-time of the FE channels to an acceptable level, the rate of a given pad and its electrical capacitance must be limited. This implies that in most chambers the size of the physical pads (either wire or cathode pads) must be smaller than required by spatial resolution. In these cases up to four adjacent physical pads are OR-ed by the FE electronics to build a logical pad. However, in regions R1-R2 of stations M2-M3 the required spatial resolution in x imposes logical pads which are too small to be practically built. For those chambers a mixed readout has been adopted: a narrow wire-strip to define the x resolution, and a larger cathode pad to define the y resolution, together defining are the logical channels seen by the trigger and DAQ. Logical pads are then obtained as an AND between wire and cathode pads (figure 6.48).

2008 JINST 3 S08005

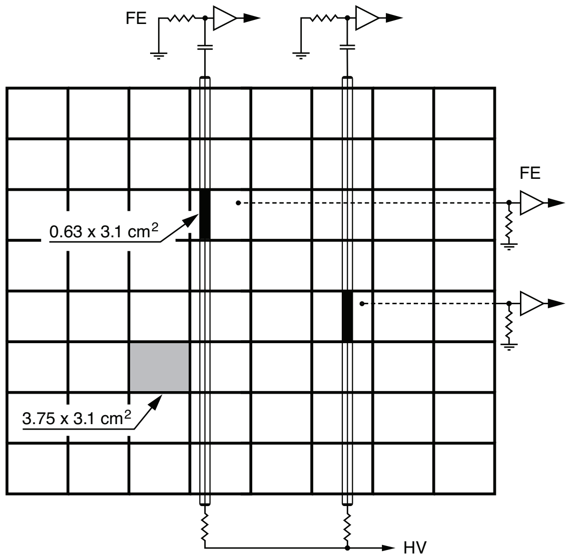

Figure 6.48: Scheme of the mixed wire-cathode pads readout in one M2R1 chamber. Two wire-pad and two cathode-pad readout channels are shown. The coincidence between crossing vertical wire-pads and the cathode physical pads defines the logical pads, shown in black.

In the M1 station, where the foreseen channel occupancy is high, the signals from the logical pads are sent directly to the trigger and DAQ. In most of the other regions, in order to reduce the number of output optical fibres, several contiguous logical pads are further OR-ed to build larger *logical channels* in the form of vertical and horizontal strips. The logical pads are then reconstructed by the coincidence of two crossing strips. This operation is performed in the Level-0 Trigger Processor (see 7.1) and in the DAQ TELL1 boards (see 8.2).

Figure 6.49 shows the partitioning of a quadrant of stations M2 and M3 into *sectors* containing the crossing strips. The sector size is adapted to the trigger processing elements that work on a fixed number of logical pads belonging to a projective tower over the five stations.

The full muon system comprises 122112 physical channels ORed into 25920 logical channels which are transmitted via optical links to the Level-0 trigger and DAQ electronics. Appropriate combinations of logical channels in the Level-0 and High-Level Trigger provide the 55296 logical pads used for the muon tracking.

The specifications of the MWPCs and GEMs and their performance are summarised in the following sections.

6.3.2 Wire chambers

Design

The LHCb muon system comprises 1368 Multi Wire Proportional Chambers. Prototype studies [170–176] showed that a time resolution of about 5 ns can be achieved in a gas gap with a wire plane of 2 mm spacing, symmetrically placed in a 5 mm gas gap, using fast, non-flammable, gas mixtures of $Ar/CO_2/CF_4$ with 40% Ar and variable concentrations of CO_2/CF_4. Finally the

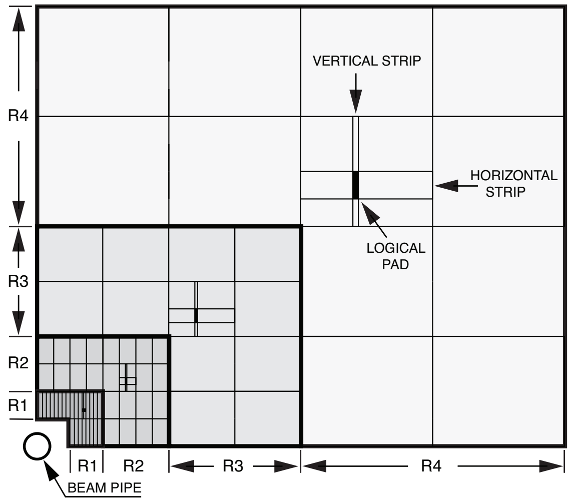

Figure 6.49: Front view of one quadrant of stations M2 and M3 showing the partitioning into sectors. In one sector of each region a horizontal and a vertical strip are shown. The intersection of a horizontal and a vertical strip defines a logical pad (see text). A Sector of region R1 (R2, R3, R4) contains 8 (4, 4, 4) horizontal strips and 6 (12, 24, 24) vertical strips.

Table 6.7: Main MWPC parameters.

Parameter	Design value
No. of gaps	4 (2 in M1)
Gas gap thickness	5 mm
Anode-cathode spacing	2.5 mm
Wire	Gold-plated Tungsten 30 μm diameter
Wire spacing	2.0 mm
Wire length	250 to 310 mm
Wire mechanical tension	0.7 N
Total no. of wires	$\approx 3 \cdot 10^6$
Operating voltage	2.5–2.8 kV
Gas mixture	Ar / CO_2 / CF_4 (40:55:5)
Primary ionisation	$\simeq 70\,e^-$/cm
Gas Gain	$\simeq 10^5$ @ 2.65 kV
Gain uniformity	$\pm$20% typical
Charge/MIP (one gap)	$\simeq$ 0.6 pC @ 2.65 kV

mixture $Ar/CO_2/CF_4(40:55:5)$ was adopted. By OR-ing the signals from two adjacent gas gaps the resulting *double gap* has an efficiency better than 95% in a 20 ns window at a gas gain of $G \simeq 10^5$. This gain is achieved at a voltage of 2600–2700 V [177]. Prototype tests with intense beams (100 kHz/cm^2) confirmed the prediction that space-charge effects are negligible at the rates expected for the experiment [178].

The main parameters of the MWPC detectors are summarized in table 6.7. Detailed simulations [179] based on GARFIELD [180] were performed to optimize the design and to establish

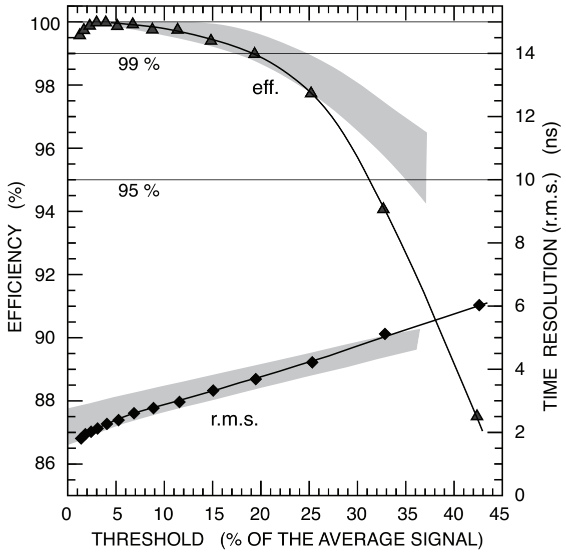

Figure 6.50: MWPC double-gap efficiency and time resolution vs. discriminator threshold for a prototype chamber. Solid lines: experimental results. The MonteCarlo simulation is shown in grey; the band accounts for different track angles.

the geometrical tolerances for the chamber construction. The primary ionisation was simulated by HEED [181] and drift and diffusion by MAGBOLTZ [182]. The design of the pad readout was optimized with SPICE [69] in order to keep the cross-talk between pads below 5%. The maximal deviations of the construction parameters was established under the assumption of a maximum variation of gas gain of $\pm 20\%$.

Figure 6.50 shows the good agreement of a MonteCarlo simulation for double-gap efficiency and time resolution versus FE threshold and the values measured on for a chamber prototype.

In stations M2–M5 a chamber is made of four equal gas gaps superimposed and rigidly stacked together with the gas flowing serially through all the gaps. Two contiguous gas gaps have their corresponding readout electrodes (either wire or cathode pads) hard-wired together in OR to form a double gap layer. The readout electrodes of the resulting layer are in turn connected to separate FE channels. As already mentioned, the M1 chambers contain only two gas gaps. These two gaps form the two layers which are readout independently. In order to maximize operation flexibility each gap has its own HV line and can be powered or switched off independently of the others.

Figure 6.51 shows an exploded schematic view of a chamber. The structural elements of the chamber are the panels, 9 mm thick, made of an insulating core sandwiched between two conducting planes. The conducting planes inside the chamber form the cathodes while the two external planes are grounded and act as an electrical shield. The panels are stacked using 2.5 mm thick PCB bars glued to the panels and superimposed to create the 5 mm gas gap. The wires are soldered and glued to the wire fixation bars while other bars seal the gap along the periphery. The 5 mm gap is ensured by several precision dowels inserted in the bars.

A cross section of a chamber is shown in figure 6.52. A U-shaped brass channel running around the chamber edges is soldered to the outer conductive planes to complete the chamber Faraday cage. The front-end boards, the LV voltage regulators and the HV filters are mounted

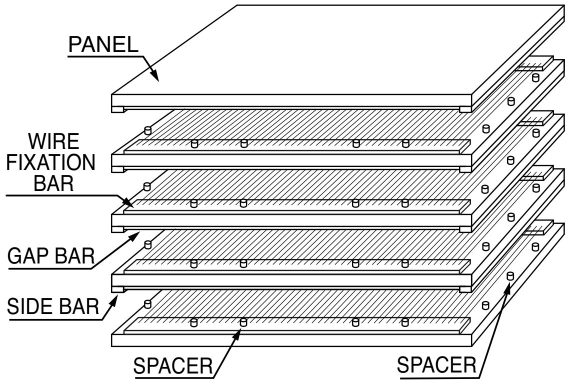

Figure 6.51: Exploded schematic view of a chamber showing the various elements.

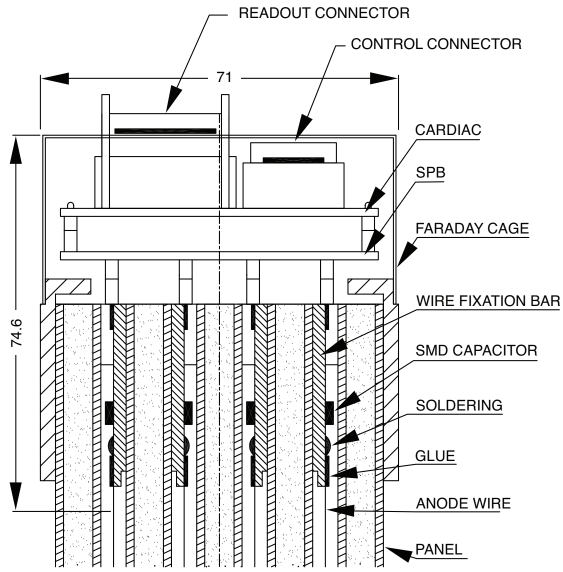

Figure 6.52: Cross section of a wire chamber showing the four gas gaps and the connection to the readout electronics. SPB: Spark Protection Board; CARDIAC: FE Electronics Board. In this case the hardwired OR forming the two Double Gaps (see text) is achieved in the SPB.

inside the Faraday cage to minimize electrical pickup. The HV is brought in through a custom-made multipin connector and multiconductor cable. LVDS shielded cables are used for signal transmission and control.

The general design and construction is the same for all chambers and is discussed in detail in [183].

Chamber construction

Given the large number of chambers, the production was distributed among six production sites. A great effort went into ensuring that all those sites had equivalent facilities and tooling, albeit with some flexibility. The same stringent quality criteria and test protocols were adopted throughout to ensure a constant quality of the produced chambers.

Figure 6.53: Panels mounted onto the winding machine frame ready to start wiring. The two combs which guide the wire are also visible. Below the panel in the foreground there is a second one attached to the underside of the frame. The two panels are wound simultaneously.

Panels The panels are the basis of the chamber mechanical structure. A panel consists of two copper clad fire-resistant fibreglass epoxy laminates (FR4), interleaved with a structural core. The panels are individually wired and then assembled to form the complete chamber.

The panel precision and its planarity define the gap quality. Therefore it is very important to achieve tight tolerances and stability in time, coupled with adequate robustness. In addition the panels must be light and stiff and easily adapted to mass production. The choice for the structural core was a polyurethane foam core for stations M2–M5 and a light honeycomb core for station M1 where a lower material budget is mandatory.

The panels were produced industrially. For the M2–M5 chambers precision machined molds were used to inject the polyurethane foam into the FR4 sandwich. Three molds of different sizes produced all the panels. For M1 chambers the core was made from a light NOMEX® sheet purchased with precise tolerance on thickness, and glued between the two FR4 foils. The pressure during gluing was assured by a vacuum bag. So the planarity of the panels is due to the quality of the honeycomb core and of the flatness of the assembly table.

The wire fixation bars (figure 6.51) were glued to the panels before the wiring process using an epoxy adhesive.[25] The gluing was performed on a special table which ensured the exact height of the bars above the panel itself.

Wiring Specially built automatic winding machines were used in all the production sites to rapidly perform panel wiring. The machines could wind one or two panels simultaneously in about one hour for the largest chambers. The panels were fixed to a rigid frame, and grooved dowels (combs) were installed parallel to the panels long sides (figure 6.53). To achieve the required precision on wire pitch, the wire spacing was determined by the combs while the wire height with respect to the cathode-plane was adjusted by precision bars mounted to the frame. The winding machines were equipped with brake motors or electronic devices to keep the mechanical wire tension constant.

Once the winding was completed, the wires were glued and soldered. The wires were glued to the wire fixation bars using epoxy adhesive before soldering. This procedure guarantees that the

[25] Adekit A140 epoxy, Axon Technologies, USA.

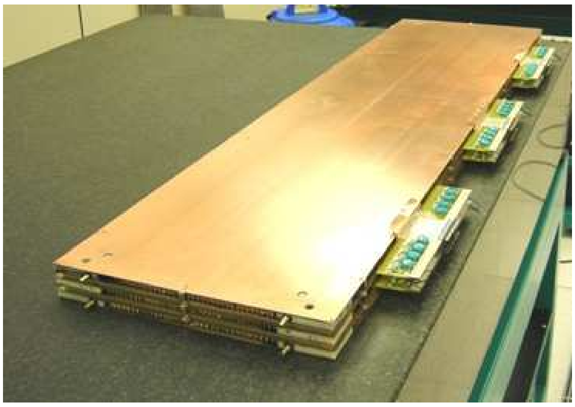

Figure 6.54: A M1R4 chamber completely assembled before the installation of the Faraday cage. The three honeycomb panels are visible. On the corners of the panels there are plastic inserts with internal channels for gas circulation. The gas nipples are inserted in the top and bottom panels. Decoupling HV capacitors, resistors and connectors for the FE boards are mounted on the printed cicuit boards on the right.

wires are kept in place with a fixed height with respect to the cathode plane. The gluing also keeps the wire tension to its nominal value.

Due to the large number of solder joints in the construction of the chambers, the use of an automated and reliable method was desirable. Automatic soldering stations [183] both with conventional soldering heads and with laser heads were employed.

Final assembly In the final assembly of the chamber the panels were superimposed and glued together using cylindrical precision spacers for alignment (see figure 6.51). The glue[26] ensures the chamber gas tightness. In the chambers of region R1 in stations M2–M3 and of region R2 in stations M1–M3, no glue was used and gas tightness was ensured by O-rings made of natural rubber. This allows to open the chambers easily if needed. Screws were used to keep together the panels. Finally the brass channels forming the Faraday cage were soldered to the outer copper cladding of the panels. Figure 6.54 shows an assembled M1R4 without Faraday cage.

Quality control and testing

Uniform quality of the chambers produced in the various sites was ensured by stringent quality tests of the individual chamber components and of the assembled chambers [184–186]. All the panels were individully measured at production and then shipped to the production sites where they were checked once more before assembly. Despite the tight tolerances the yield of good panels was 90%.

Once the panels were produced, the pitch and the mechanical tension were measured for all wires. The wire pitch was determined with an automated device based on two digital cameras [186]. The distribution of the measured wire pitch has an r.m.s. of 16 μm. Only a very small number of wires with pitch value outside tolerance (± 0.1 mm) had to be replaced.

[26] Adekit A145 and Araldite 2011 epoxy, Huntsman Advanced Materials, Switzerland.

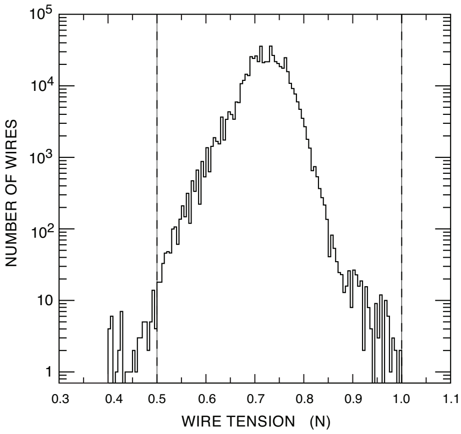

Figure 6.55: Distribution of the mechanical tensions of the wires as deduced from a measurement of the wire mechanical resonant frequency. The mean value of the tension is 0.73 N with an r.m.s. of 0.091 N. The wires having a tension outside the interval $0.5-1$ N (dashed lines) were replaced.

To determine the wire mechanical tension automated systems were developed [187, 188] which measures the mechanical resonant frequency of each wire. The distribution of the wire tension measured on the above mentioned sample is reported in figure 6.55.

The checks on the assembled chambers consisted of a gas leak test and a HV test at 2800–2900 V using the standard gas mixture. The chamber gas leakage was determined by monitoring the decrease in time of an initial overpressure of 5 mbar. The method [186] had a sensitivity of about 0.01 mbar/hour well below the maximum gas leakage rate accepted of 2 mbar/hour.

The uniformity of the gas gain in the gaps was systematically checked using radioactive sources mounted on automated tables which performed an (x,y) scan over the complete chamber surface [185, 186, 189]. Figure 6.56 shows the gain measurement on a sample of 184 chambers.

All the above checks were performed without the readout electronics installed.

Finally all chambers, fully equipped with the front-end electronics, underwent a final test with cosmic rays prior to installation and the electronic noise was checked once more when the chambers were mounted in the experiment. The maximum accepted noise rate was 1 kHz per FE channel, a value which has no impact on the trigger system.

In addition, all the chambers for the regions exposed to the largest particle flux, were conditioned at the CERN Gamma Irradiation Facility (GIF) [190] to ensure their stable functionality under high radiation.

Important information about the individual components and the final chamber was stored in a database. This allows to retrieve at any time the results of all quality control measurements and will aid in understanding possible problems.

Aging properties

Extensive aging tests were performed on prototypes at the CERN GIF and at the Calliope[27] facility. The goal of the tests was to prove that the performance of these chambers is not deteriorated by

[27]ENEA-Casaccia Research Centre, Rome.

2008 JINST 3 S08005

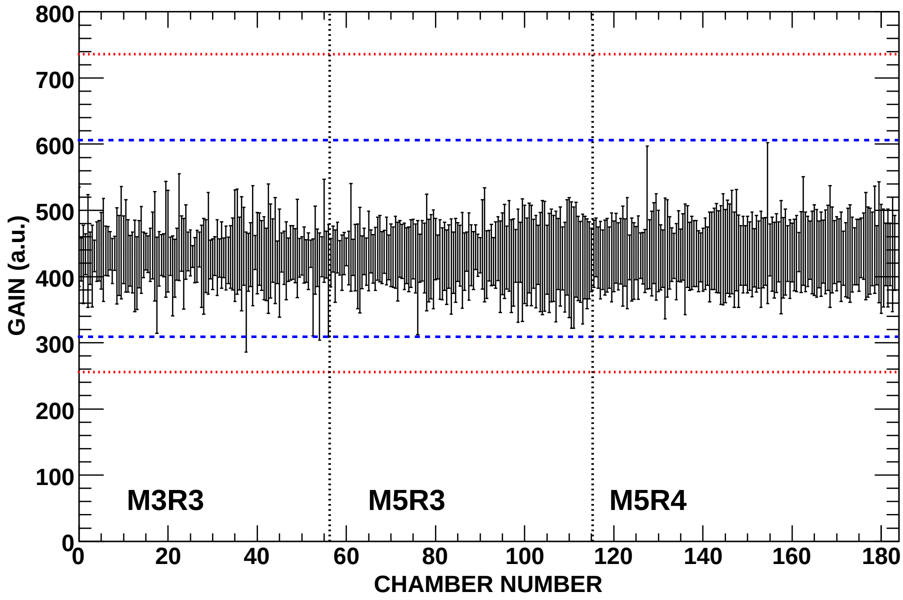

Figure 6.56: Gain uniformity measured for a sample of 184 chambers. The bars are proportional to the total gain spread of a double gap. The horizontal lines indicate the allowed acceptance intervals for good (in blue) and spare (in red) chambers.

the large radiation dose expected in the experiment in ten years of operation (10^8 s) at the nominal luminosity of 2×10^{32} cm^{-2} s^{-1} . In these tests the gain loss was measured against a non-irradiated reference chamber or gas gap.

In the test performed at the GIF facility at CERN, a four gap MWPC was irradiated for six months, accumulating a charge of 0.25 C/cm without detecting any gain loss [191].

In an accelerated test during 30 days of irradiation at the ^{60}Co source of Calliope, we monitored the currents in five four-gap MWPCs: four test chambers and a reference one [176, 192]. The chambers were operated at a voltage of 2.75 kV, corresponding to a gas gain of $1.8 \cdot 10^5$ [177], twice the value that will be adopted in the experiment. The largest integrated charge collected on a chamber wire was 0.44 C/cm. This corresponds [169] to about 7 years (10^7 s/year) of operation of the most irradiated chamber (in M1R2) at a luminosity of 2×10^{32} cm^{-2} s^{-1} , assuming a safety factor of 2. No gain loss or other significant effect was detected.

6.3.3 GEM chambers

In the innermost region R1 of the station M1, the most stringent requirements for the detector is a rate capability of up to 500 kHz/cm^2 of charged particles. Due to the large particle flux in this region the chambers must also be especially radiation hard such that no ageing effects will be visible in 10 years of LHCb operation. This is difficult to achieve in wire chambers unless the gain is decreased, at the price of a worse signal-to-noise ratio.

After an extensive R&D program triple-GEM chambers with active area of 20×24 cm^2 were selected for M1R1. Each of the 12 chambers consists of two triple-GEM detectors superimposed and forming the two sensitive layers, which are then logically OR-ed.

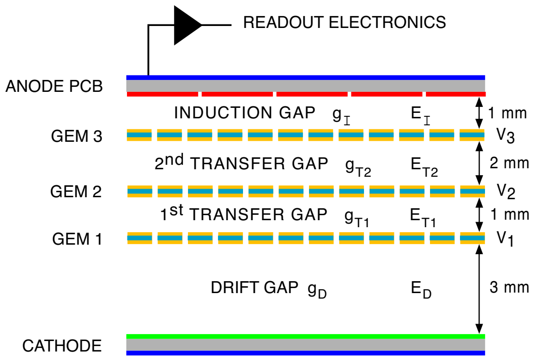

Figure 6.57: Schematic cross section of a triple-GEM detector showing the most relevant elements and dimensions (see text).

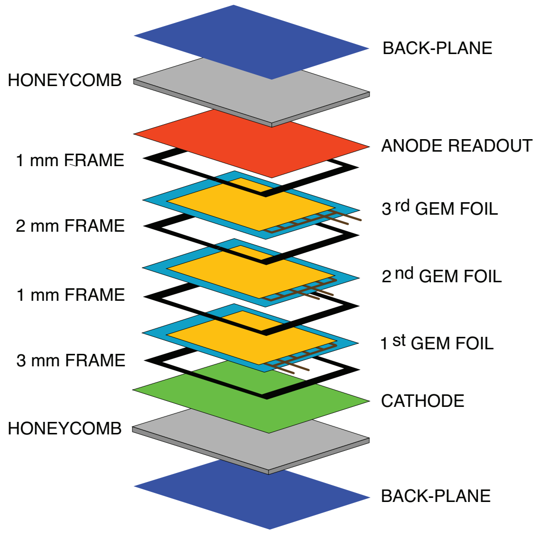

Figure 6.58: Exploded view of a triple-GEM detector.

Design

The triple-GEM detector, which consists of three gas electron multiplier (GEM) [193–195] foils sandwiched between anode and cathode planes, can effectively be used as tracking detector with good time and position resolution. A cross section of the detector, showing the different elements and their physical dimensions, is shown in figure 6.57. An exploded view is presented in figure 6.58.

The ionisation electrons, produced in the drift gap between the cathode and the first GEM foil, are attracted by electric fields through the three GEM foils where they are multiplied. Once they cross the last GEM foil they drift to the anode in the induction gap, giving rise to an induced current signal on the pads.

Prototype tests have shown that the fast $Ar/CO_2/CF_4(45:15:40)$ gas mixture allowed to achieve a time resolution better than 3 ns, to be compared with the time resolution of $\sim$10 ns obtained with the standard Ar/CO_2 (70:30) gas mixture [196].

Another improvement in time performance has been obtained by optimizing the detector geometry. Mechanical considerations indicate that a minimum distance of 1 mm should be kept between GEM foils. The size of the drift gap g_D is large enough to guarantee full efficiency for charged tracks. The first transfer gap g_{T1} is kept as small as possible to avoid that primary electrons produced in the same gap give rise to a signal over threshold. The second transfer gap g_{T2} is larger than the first one to let the diffusion spread the charge over more holes and then lower the discharge probability. The induction gap g_I is kept as small as possible to maximize the signal fraction integrated by the amplifier.

The best values of the gap fields and of the voltage across the GEM foils were determined experimentally by optimizing time resolution versus discharge probability and are typically E_D = 3.5 kV/cm, E_T = 3.5 kV/cm and E_I = 5 kV/cm and V_1 = 440 V, V_2 = 430 V, V_3 = 410 V. The anode pad printed circuit board is such that the pad to pad distance is 0.6 mm and the pads are surrounded by a ground grid of 0.2 mm thickness to suppress cross-talk.

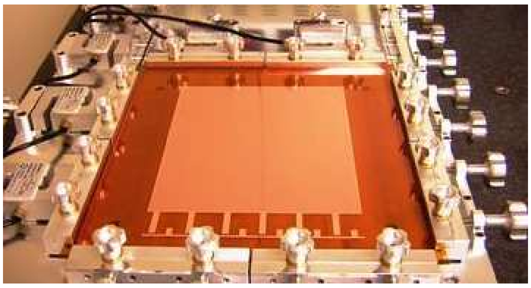

Figure 6.59: Stretching of a GEM foil.

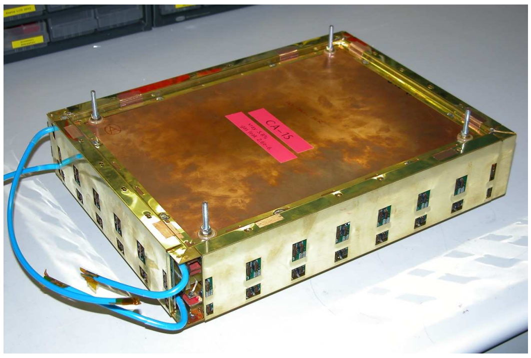

Figure 6.60: GEM chamber fully assembled with the 24 FE electronics boards. The cutouts in the Faraday cage allow the insertion of the cable connectors.

Measurements on prototype chambers made of two detectors in OR showed an efficiency better than 96% in a 20 ns window at a gain of $6 \cdot 10^3$. The pad cluster size upper limit of 1.2 and the discharge studies suggested a maximum working gain of about $2 \cdot 10^4$ [195].

Chamber construction

All the critical steps in chamber assembly were carried out in class 1000 clean rooms or under class 1000 huts, with controlled temperature and humidity conditions. The huts were used for all operations involving GEM foils.

The GEM foils, 50 μm thick Kapton with two-sided Cu cladding of 5 μm, have an active area of 202×242 mm^2 and were manufactured by the CERN-EST-DEM workshop. The holes have a bi-conical structure with external (internal) diameter of 70 (50) μm and a pitch of 140 μm. In order to limit the damage in case of discharge, one side of the GEM foil is divided into six sectors, of about 33 mm $\times$ 240 mm. The separation between sectors is 200 μm. Each individual foil was visually inspected for defects and for leakage current. Then the foils were stretched with a mechanical tension of about 1 kg/cm with a special device visible in figure 6.59.

After the GEM stretching, a fibreglass frame was glued on the GEM foil using a Ciba 2012 epoxy. Both cathode and readout pad electrodes, realized on standard 1.0 mm thick printed circuit board, were respectively coupled with a 1.0 mm fibreglass foil by means of an 8 mm thick honeycomb structure, The back-panel with a 12 μm copper layer deposition on its external side is used as a Faraday cage for the detector. The stiff cathode and pad panels act as support plates for the whole detector. These panels house two gas inlets and two gas outlets, made with machined Stesalit inserts.

All fibreglass parts that are in contact with the sensitive volume of the detector, were visually inspected in order to eliminate any residual spikes or broken fibres. They were then cleaned in an ultrasonic bath with de-mineralized water and dried in an oven at a temperature of 80°C during one night.

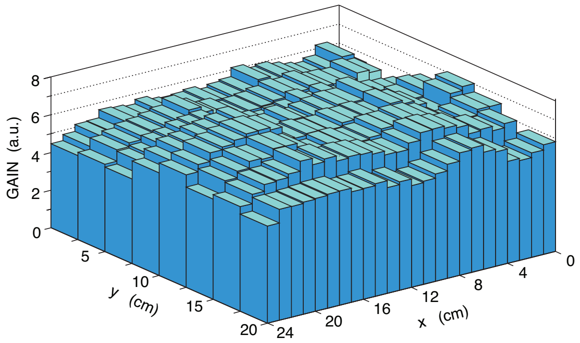

Figure 6.61: Response uniformity of a GEM chamber measured with an X-ray gun. The RMS gain variation over the 24×8 pads is typically less than 10%.

The detectors were built on a high-precision reference plane by piling up and gluing together the component parts in the following order (see figure 6.58): cathode panel; the first GEM foil (GEM1) glued on a 3 mm thick fibreglass frame; the second GEM foil (GEM2) glued on a 1 mm thick frame; the third GEM foil (GEM3) glued on a 2 mm thick frame and then the last 1 mm thick frame followed by the pad panel. All the gluing operations were performed using Araldite AY103 epoxy and HY991 hardener. The aging properties of both glues have been studied during irradiation tests [197, 198]. A complete chamber is shown in figure 6.60.

Quality control and testing

Several quality checks were performed on individual detector components before chamber assembly. Since the cathode and anode panels are the main mechanical structure of the detector, they were checked for planarity. Measurements over the whole panels showed that the deviation from the average plane was of the order of 50 μm (r.m.s).

The quality of GEM foils was checked by performing various tests. A preliminary optical inspection was performed with a microscope to check for photolithographic imperfections. If the GEM foil passed the visual inspection, a high voltage test was performed. Such a test was done in a gas tight box, flushed with nitrogen too keep the relative humidity at $\sim$25% level. The foil was accepted if the leakage current was less than 1 nA at 500 V.

After construction, the detector gas leak rate was measured. This measurement was performed by inflating the detector to an overpressure of $\sim$10 mbar together with another gas-tight chamber used as reference, and recording the overpressure decay. The typical gas leak rate of a detector is of the order of few mbar/day. At the gas flow forseen in the experiment (80 cm^3/min) this leakage rate will result in an acceptable humidity level lower than 100 ppm.

A gain uniformity test, performed with an X-ray gun, checked both the mechanical tolerance and the response uniformity of single detectors. A typical result is presented in figure 6.61. The current signals induced on each of the 192 pads of each detector were corrected for temperature and pressure variations. The current deviations from the average were all below 20% with a typical RMS $< 10\%$. Finally, a cosmic ray test was performed on all chambers fully equipped with front-end electronics.

2008 JINST 3 S08005

Discharge and aging properties

The use of the non-standard $Ar/CO_2/CF_4(45:15:40)$ gas mixture required the demonstration of high robusteness of the GEM to discharges and ageing effects. In fact the choice of the electric field in the detector gaps and the unbalanced configuration of the voltages applied to the GEM foils ($V_1 > V_2 > V_3$, see figure 6.57) are the result of a minimization of discharges produced by alpha particles. More than 5000 discharges were integrated with neither breakdown nor performance losses using alpha particles and a high intensity low momentum pion/proton beam. These measurements demonstrated that GEMs in M1R1 can operate safely. The large fraction of CF_4 in the gas required that a global irradiation test of the final chamber be performed to check the compatibility between the construction materials and the gas mixture. For this reason a test was performed at the Calliope facility with an intense gamma ray flux from a ^{60}Co source. In this test, a charge of 2.2 C/cm^2 on the anode pads and GEM3 foil was integrated. This is the charge foreseen for more than 10 years running if the GEMs are operated with a gain of $\sim$6000 and a safety factor of 2 is applied. The performance of these chambers was measured in a test beam before and after irradiation and no damage or performance losses were detected [197, 198].

6.3.4 Muon System mechanics

All muon stations, including the iron filters, are separated into two halves which can move on rails away from the beampipe for maintenance and installation. The chambers, mounted on support walls, can also move with respect to the iron filters which are normally located close to the beampipe. Iron plugs minimize the free space between the beampipe and the iron filters to reduce small-angle background.

For M2–M5 two large support structures built from iron beams accomodate the suspensions for the four chamber support walls and have platforms for the electronics racks and gas systems. Cable chains are used to connect the cables, fibers, gas pipes and water cooling pipes with the outside. Station M1 has independent support structure and the related racks are located on the floor of the cavern. Cable chains are used in M1 to carry the 1200 cables to the racks.

The walls are designed to support the weight of the half-stations with minimal thickess and are built of aluminium sandwich plates. M1 wall is thinner to minimize material in front of the electromagnetic calorimeter. This is possible since the weight of M1 chambers is reduced thanks to the use of only two gaps and honeycomb panels. The material budget of the M1 station is 0.26 X_0 on average with the chambers and the FE electronics contributing 0.16 X_0 and the mechanics, cables and gas pipes contributing the rest.

Alignment

The position of the chambers must be adjusted in order to minimize chamber overlaps which would introduce ambiguities. Moreover, since the muon trigger relies on the projectivity of the stations, a precise relative space alignment has to be performed, in particular in the inner region where an accuracy of about 1 mm is required.

The chambers are mounted with screws on angle brackets fixed to the supporting walls. The walls were first precisely aligned by adjusting the overhead suspensions, then each chamber was

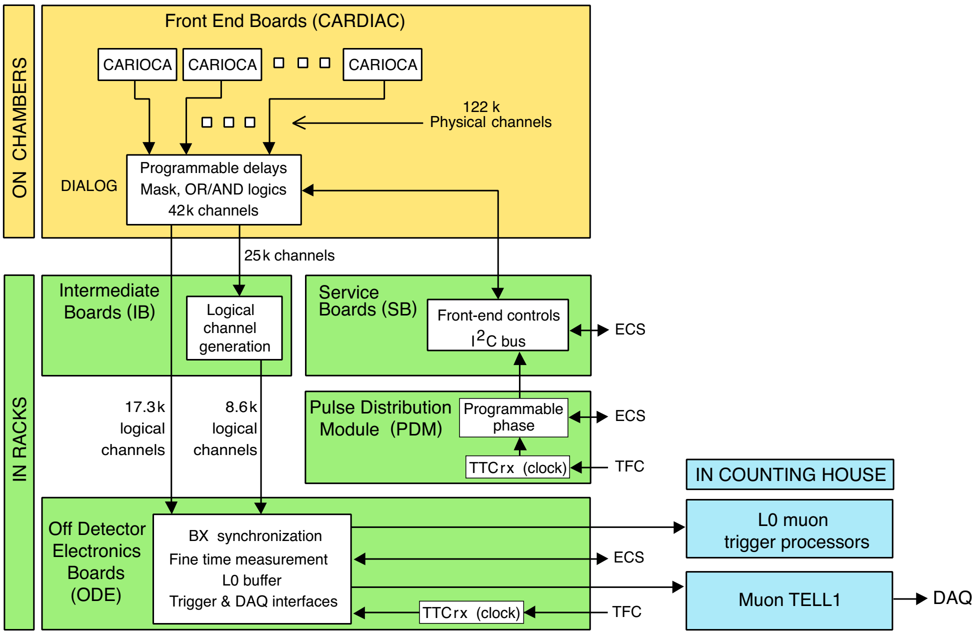

Figure 6.62: Simplified scheme of the Muon electronics architecture.

aligned relative to the wall. The position was adjusted vertically using spacers and horizontally via the slotted holes in the brackets. For horizontal and vertical alignment, the reference points were the support wall edge close to the beampipe and the top edge, respectively. Finally, the equipped walls were precisely aligned together using as reference each half-station, the centre of the beampipe. The reproducibility of the measurements is $\mathcal{O}(1)$ mm and the reproducibility of the position after moving the walls is of the same order.

6.3.5 Electronics

Figure 6.62 shows schematically the architecture of the Muon readout electronics. The task of the electronics is twofold: prepare the information needed by the Level-0 muon trigger and send the data to the DAQ system. The main steps are:

i. the front-end CARDIAC boards perform the amplification, shaping and discrimination of the ≈ 120 k chamber signals. The time alignment to within 1.6 ns of the different channels needed to correct for different cable lengths and different chamber behaviour is also done in this step. This is mandatory since the Muon Trigger is fully synchronous with is also done in this step, the LHC cycle.

ii. The ≈ 26k logical-channel signals are generated by suitable logical ORs of the physical channels. This step is performed on the FE boards and on special Intermediate Boards (IB), when the logical channel spans more than one FE board.

iii. The Off Detector Electronics (ODE) boards receive the signals from the logical channels. They are tagged with the number of the bunch crossing (BX identifier) and routed to the trigger processors via optical links without zero suppression.

iv. The fine time information, measured by the TDC on the ODE boards, is added and the data are transmitted via optical links to the TELL1 board and from the TELL1 to the DAQ system.

As far as possible, step ii. is performed on the chambers front-end boards in order to minimize the number of LVDS links exiting the detector. The other steps are performed on dedicated electronics boards mounted on racks on the left and right sides of the muon stations M2–M5 which also accomodate the LV and HV power supplies. Since the racks are installed on the same structure which supports the stations, cable chains for the chambers could be avoided. For station M1 the electronics racks are placed under the RICH and, as mentioned above, are connected via cable chains to the chamber walls.

Radiation issues

The Muon electronics must operate reliably for more than 10 years in a hostile environment. The FE boards in the regions close to the beampipe are exposed to very high radiation doses: in M1 the maximum total ionising dose (TID) foreseen in 10 years is 5000 Gy. This decreases by only a factor 3 for M2. The maximum neutron and hadron fluences are in the range of $10^{13}/\,\mathrm{cm}^2$. Therefore, all the ASICs used in the FE Electronics were produced using radiation-hard technology.

The radiation dose is considerably less on the detector periphery where the electronics racks are located. TID values of up to 10 Gy in 10 years are expected in the electronics racks.[28] These doses nevertheless dictate the use of radiation tolerant components or a proper qualification of commercial components.

For complex logic design, two kinds of FPGA both from the ACTEL family are used. The A54SX family was chosen first for good radiation immunity and was used in the Intermediate Boards (IB). A more advanced type of FPGA from the flash-based ProASICPLUS APA family, was chosen in the design of ODE, PDM and SB boards. Based on ACTEL flash technology, ProASICPLUS devices offer reprogrammability and nonvolatility in a high density programmable logic product. The ProASICPLUS is also suitable in a high radiation environment thanks to the radiation hardness of its flash cells.

Commercial off-the-shelf electronics (COTS) was used for glue logic and signal conversion. All chip were validated with respect to the radiation environment.

Dedicated ASICs

The large number of channels in the muon system, the flexibility necessary to adapt the readout scheme to the different regions, the necessity to synchronize all the channels in a 20 ns window, the high radiation expected in M1 and in the inner regions led us to develop three dedicated rad-hard ASICs (CARIOCA, DIALOG and SYNC) using IBM 0.25 micron technology. All chips provide and accept logical LVDS data.

Front-end board

The chamber readout is performed via front-end boards (CARDIAC) [199] plugged directly onto the chambers. Each CARDIAC has 16 inputs and 8 outputs, and is equipped with two CARIOCA

[28] this value includes a safety factor of 2.

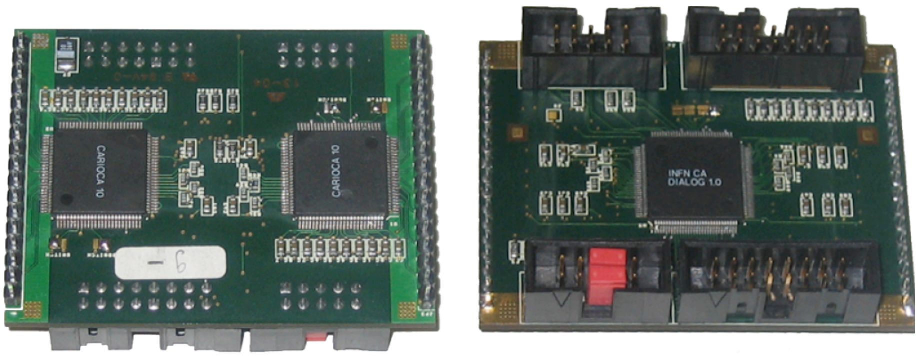

Figure 6.63: Top and bottom views of the CARDIAC board, showing the two CARIOCA chips and the DIALOG chip.

chips and one DIALOG chip, as shown in figure 6.63. A special diode circuit protects the front-end amplifiers from sparks and is mounted on a separated board.

The CARIOCA [200–202] is a front-end amplifier-shaper-discriminator chip with eight channels whose input polarity is selectable. The front-end current preamplifier can handle well the large spread in detector capacitances encountered in the muon chambers (from 20 pF for the M1R1 to 220 pF for the M5R4 chambers). The peaking time is $\sim$10 ns at the lowest detector capacitance. The input impedance is 50 Ohm which is important to reduce internal pad-pad cross-talk. The chip includes tail cancellation and baseline restoring. The dead time of a fired channel, almost independent of the pulse height, is in the range 50–60 ns.

The CARIOCA has separate thresholds for all the channels in order to overcome the problem of channel-to-channel uniformity in the internal discriminators. Equivalent noise is about 2000 electrons at 0 capacitance, and increases as (42–45) e/pF. Power consumption is about 45 mW/ch.

The DIALOG [203, 204] chip has 16 inputs to receive the outputs from two CARIOCA chips, and performs the logical OR of corresponding pads in the two layers of a chamber to form logical channels. The DIALOG is equipped with adjustable delays for every input allowing the various input signals to be aligned with a step of 1.6 ns. In addition, the DIALOG also allows setting the CARIOCA thresholds and can mask individual channels. It also contains features useful for system set-up, monitoring and debugging. Triple-voting and auto-corrected registers are used to increase single event upset immunity.

The CARDIAC boards are enclosed inside the chamber Faraday cage, together with radiation-tolerant voltage regulators (LH4913) which supply the necessary 2.5 V to the boards. The R4 chambers use only three CARDIAC boards and one regulator each, while the M1R2 chambers require 24 CARDIAC boards and six regulators each.

Given the large number of readout channels the muon system comprises nearly 8000 CARDIACs. All the boards were tested after assembly, and had to pass successfully a thermal cycle to be accepted. Once mounted on the chamber the characteristics of each board, in particular with respect to noise, were measured again.

A special version of the CARIOCA chip, with lower threshold and longer shaping time because of the lower gas gain, CARIOCAGEM [202], has been produced for use on the GEMs. The tail cancellation is suppressed considering the purely electron signal in the GEM case. A more compact CARDIAC card has also been designed, given the tight space available in the R1 region.

SB and PDM boards

The front-end boards are managed by the Service Boards (SB) [205] that handle the setting of the thresholds in the CARIOCA chip, as well as the adjustable delays, the channel masking and the setting of the AND/OR logics in the DIALOG chip. Each SB houses four ELMB [206] modules based on an 8-bit microcontroller (Atmel ATMega128) whose firmware was customized to permit I^2C communication with the CARDIACs via twelve serial links. Each SB can control up to 192 CARDIAC boards. The full system comprises 156 SBs, managing the approximately 8000 CARDIAC boards of the muon system. Most of the calibration and test procedures of the front-end are implemented in the ELMB firmware and are performed directly by the SBs.

A Pulse Distribution Module (PDM) resides in each of the 10 crates containing the service boards. The PDM is based on an ELMB and houses one TTCrx chip which generates low-jitter pulses in a chosen phase relation with the LHC machine clock. The pulses are then distributed to the service boards by means of a custom back plane. This facility is crucial for the time alignment of the muon system.

IB board

Whenever the generation of the logical channels is not possible at the DIALOG level, an additional logical layer is needed. This happens in regions R2, R3 and R4 of stations M2 to M5. The needed layer, the Intermediate Board (IB), implements the necessary logic on three ACTEL A54SX16A anti-fuse FPGAs. Anti-fuse technology offers good tolerance against high radiation doses. The IB has been tested successfully with up to 68.5 Gy without failures. The system comprises 168 IB boards which are installed in the electronics racks.

ODE board

The ODE board [207] contains the Level-0 pipelines and DAQ interface. It synchronizes signals and dispatches them to the Level-0 trigger. Each ODE receives synchronous TFC signals by way of a TTCrx chip [113]. On-board clock de-jittering and distribution is managed by a QPLL chip [208]. A total of 152 ODE installed on the same racks as the IBs, are used.

Each board receives up to 192 logical channels and outputs data to the Level-0 muon trigger and to the DAQ system. The incoming signals are assigned the appropriate BX identifier and are sent to the Level-0 muon trigger directly via twelve 1.6 Gb/s optical links, each served by one GOL chip [209]. In parallel, the data are sent to the Level-0 pipelines, where they reside for 4 μs before receiving the *L0-accept* signal. Upon reception of a trigger, data are written into the L0 derandomizer, a FIFO programmable to a maximum depth of 16 data words. The derandomizer allows the data to be read out at a regular rate of 1.1 MHz with a safe margin with respect to the L0 average trigger rate of 1 MHz. Its programmable depth allows it to cope with instantaneous bursts of up to 16 consecutive triggers. Finally the data are formatted and sent to the TELL1 boards. The LVDS receivers, the Level-0 pipelines, the Level-0 derandomizer and the 4-bit TDC for fine time alignment are integrated into a single component, the SYNC chip [204]. The chip incorporates a number of error-detection features, allowing remote control and diagnosis of possible malfunctions on the boards. The other main board components (board controller, Level-0 buffer and DAQ interfaces) are based on one FPGA.[29] Each ODE board also contains a CAN node, based on one Embedded Local Monitor Board (ELMB) [206], for board control via the ECS.

Channel mapping to the Level-0 trigger is organized by grouping the logical channels in three different ways. This is accomplished placing the SYNC chips on daughter-boards of three different sizes, containing 2, 4 or 6 chips, while the ODE mother board is always the same. In the three cases 12, 8 or 6 links respectively are active on the daughter board. The design of the ODE board has been very challenging because it must cope with several, and sometime contradictory, requirements. Due to the limited space available, the board has a high channel density (192 differential inputs into a 6U card), and should provide a good level of flexibility and at the same time match the different trigger sector topologies. High signal integrity is also mandatory to guarantee high quality optical transmission. For radiation tolerance, a triple modular redundancy technique has been used whenever possible to increase single event upset immunity.

Muon TELL1 features

Upon reception of a trigger, the data from the detector logical channels are transmitted from the ODE to the TELL1 and from the TELL1 to the DAQ system. The description of the TELL1 board is given in section 8.2. The muon-specific TELL1 board, performs standard control of event synchronization, as well as zero suppression and is also programmed to reconstruct the logical pads as the intersection of two crossing logical channels of the stations M2 to M5. This information is added to the event data to speed up the muon identification algorithm used in the HLT trigger. The muon system requires 14 TELL1 boards (four in the M1 and M2 stations and 2 in the M3, M4, and M5 stations). These numbers are determined by data flow and connectivity requirements as well as the required ECS partitioning.

6.3.6 LV and HV systems

The Low Voltage and High Voltage systems are based on radiation-tolerant power supplies. They are installed in the pit on racks on both sides of the muon stations M2–M5 and in the radiation safe area under the RICH. Eight LV power supplies[30] are used for the CARDIAC boards and ten for the off-detector electronics boards.

The HV cabling for the wire chambers is designed to supply independently all the gaps, i.e. potentially about 5000 channels. Two distinct power supply systems are used. The first system, developed by PNPI and the University of Florida for CMS, is based on 36-channel modules and powers the R4 and R3 chambers in M2-M5. Some of the gaps of R4 chambers are connected in parallel in groups of four via patch panels. In this way the number of independent HV channels is reduced from 3840 to 1920. The gaps connected in parallel always belong to different chambers to minimize the loss of efficiency in case, e.g., one gap should become shorted. The second system is a commercial one based on 32-channel modules.[31] It powers the chambers more exposed to

[29] ACTEL flash ProASICPLUS FPGA (APA450PQG208).

[30] MARATON low voltage power supply system for hazardous hostile environment; W-IE-NE-R, Plein & Baus GmbH, Burscheid, Germany.

[31] CAEN Easy 3000 and A3535P.

2008 JINST 3 S08005

radiation and drawing larger currents, and for this reason all the 1152 channels can be individually controlled and monitored.

Both HV systems have been tested for radiation resistance (hadrons, total dose and neutrons) and are apt to satisfy LHCb requirements for 10-year operation with a 10-fold safety factor.

The GEM detectors require several voltages to operate. To achieve maximum flexibility and safety a customized system [210] was designed, which allows independent settings for all of the GEM electrodes for a total of 168 channels. This system is entirely installed in the counting house.

6.3.7 Experiment control system

The control of the muon detectors is carried out with a distributed system where the processing capacity is shared among the system nodes. CANBus was chosen because of its features of multi-master protocol with real-time capability, error correction, long distance communication and low noise. CAN nodes based on ELMBs are present in the ODE, SB and PDM boards. The implementation of calibration and test procedures in the ELMB firmware, as is the case for the SBs, maximizes the parallelism of the system and minimizes the traffic on the CANBus which is only used to communicate the results of the procedures.

All the physical channels which cannot be accessed via DAQ can be monitored via ECS while running the experiment to measure noise level and detecting dead channels. More complex procedures such as noise measurements at several thresholds to detect faulty FE channels will be performed offline, The pulse system (PDM) will allow for checks of the time alignment of the full detector.

The ECS software (see section 8.4) was developed in PVSS following the general experiment guidelines and exploiting the tools provided by the LHCb PVSS framework. The muon ECS is partitioned in two independent left-right halves and is organized in hierarchycal topological structures. Each device of the muon system, like SBs, ODE Boards, HV and LV power supplies, is seen as a Finite State Machine with well defined states and interactions with other machines.

Ten PCs running PVSS programs are used to manage all the CARDIAC, ODE and SB boards. Six are used to control the HV and LV power supplies and one to monitor the environment pressure and temperature. The entire hierarchy is controlled by two PCs, one for the left and one for the right side of the muon system.

6.3.8 Gas system

The gas system has been designed in collaboration with the CERN Gas Group. Due to the rather large gas volume of the MWPCs (8.3 m^3), a recirculation system is used with a planned regeneration rate of about 90%. A pump in the return line allows the gas to be compressed before entering the gas building at the surface, where the mixing and purifying units are located. The purifier in the recirculation circuit contains two cleaning agents: a molecular sieve to keep the water contamination below the level of 100 ppm, and activated copper as a reducing agent for oxygen impurities, which should be kept below the 50 ppm level. A humidity and an oxygen meter allow for measurement of the impurity concentration before or after the purifier. Due to the small gas volume of only 10 litres, a vented system is used for the GEM chambers.

2008 JINST 3 S08005

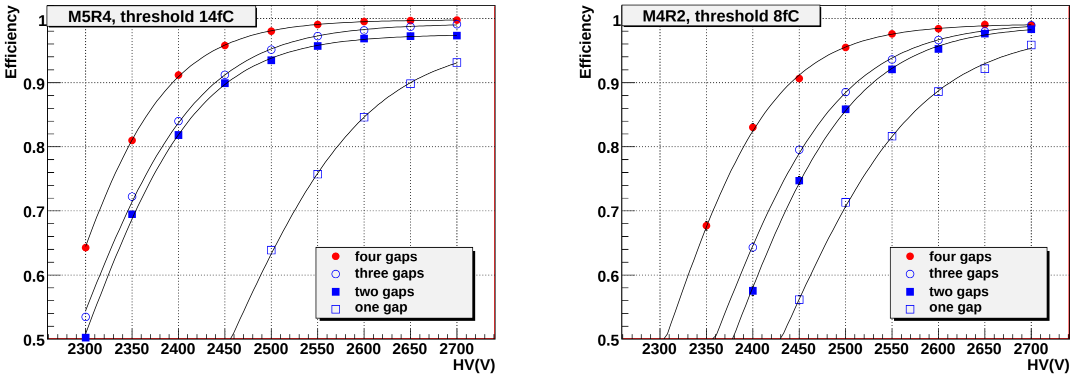

Figure 6.64: Plateau curves showing the efficiency in a 20 ns window for an anode-readout chamber (left) and a cathode-readout chamber (right). The four curves refer to different number of gaps being operated (see text). The threshold values in fC are also indicated, a lower value being used for cathode readout.

The flow rate varies across the detector surface from one volume exchange per hour, for the regions exposed to the largest irradiation (inner regions of station M1), to two volume exchanges per day for the outer regions of stations M4 and M5. Six distribution circuits are used: two for M1, two for M2–M3 and two for M4–M5. They are equipped with gas flow meters for the inputs and outputs of each supply line.

While the 12 GEM chambers have individual supply lines, only 180 supply lines are used for the 1368 MWPCs. To maintain still a parallel gas supply for each chamber, which is required to ensure an optimal performance of each individual chamber, several distributors serving 5–8 chambers have been installed on the support walls. In order to equalize the gas flow through the chambers connected to each distributor, capillaries with an impedance of about 1 mbar are introduced at the input of each chamber.

6.3.9 Performance

MWPC

Extensive tests were performed on prototypes and final MWPCs both in test beams and with cosmic rays at the production sites to measure the chamber performance. All measurements were conservatively done using a 20 ns time window.

Whereas MWPCs are expected to operate normally with four gaps in OR (two in case of M1 chambers), it is possible that a chamber will be operated with fewer gaps. Figure 6.64 shows the efficiency as a function of the applied voltage for the largest chamber with anode readout (M5R4) and for one chamber with cathode readout (M4R2). The curves are given for the standard four-gap OR configuration, but also for three-gap configuration (one double-gap fully working and the second with one gap shut off), for two gaps read by the same front-end and finally for the single-gap case. The curves show clearly the large improvement obtained by adding gaps, but also that,

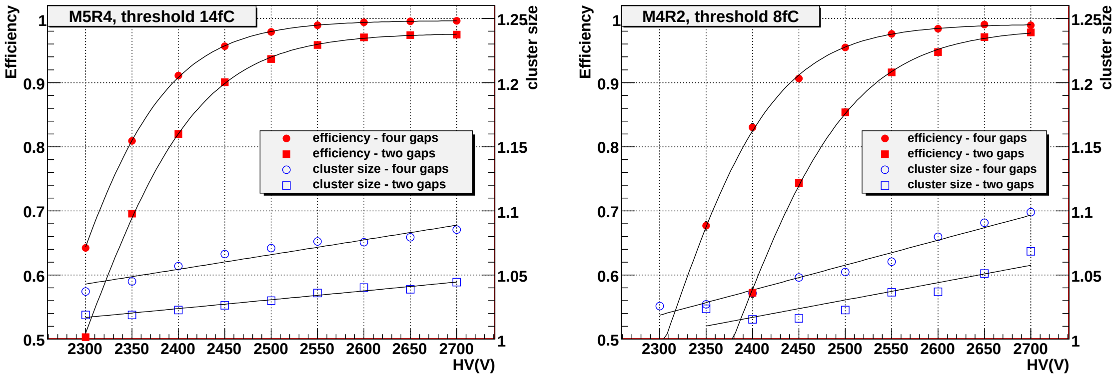

Figure 6.65: Efficiency and cluster size in a 20 ns window for the four-gap and double-gap configurations vs. HV. Anode readout-type chamber (left) and cathode readout-type chamber (right).

in case one gap should be shut off during the data taking, the redundancy built into the chambers will make the loss in performance negligible.

Another important parameter is the cluster size, i.e. the average number of pads fired by a crossing particle. The cluster size affects directly the space resolution and the p_T measurement in the Level-0 trigger since the yes-no readout does not allow an interpolation between adjacent pads. A non-negligible contribution to the cluster size comes simply from the geometry given the fact that inclined tracks can cross two adjacent pads belonging to different gaps. Another contribution comes from the chamber itself: inductive and capacitive cross-talk in the chamber and in the electronics. The design criteria requires that the intrinsic cluster size should be less than 1.2. This is well satisfied as can be seen in figure 6.65 which shows the cluster size distribution for the M5R4 and M2R4 chambers measured with perpendicular tracks [211]. Cosmic rays have also been used to check the gas gain uniformity on final chambers [212].

The rate capability of the MWPCs was studied at the CERN GIF [213] test beam. The detection efficiency of the chamber exposed to the intense gamma flux was measured with a 100 GeV muon beam. The chamber performance was studied for several detector gap configurations and different values of the background rate from the source.

No effect was detected at the maximum gamma rate allowed at the GIF where a current density of 28 nA/cm^2 was measured at a high voltage of 2.75 kV. This value is about the one expected in the chamber with the highest occupancy in the nominal conditions of running. This is in agreement with the results of the simulations [179] which show that space charge effects due to accumulation of ions are expected only at much higher currents.

GEM chambers

Triple-GEM detectors with the final FE electronics were tested both in a dedicated 40 MHz test beam and with cosmics in the lab.

Efficiency and cluster size in a 20 ns window, as a function of gain, are shown in figure 6.66 for a chamber composed of two triple-GEM detectors. Thanks to the longer shaping time of the CARIOCAGEM with respect to the standard CARIOCA chip the beginning of the efficiency plateau

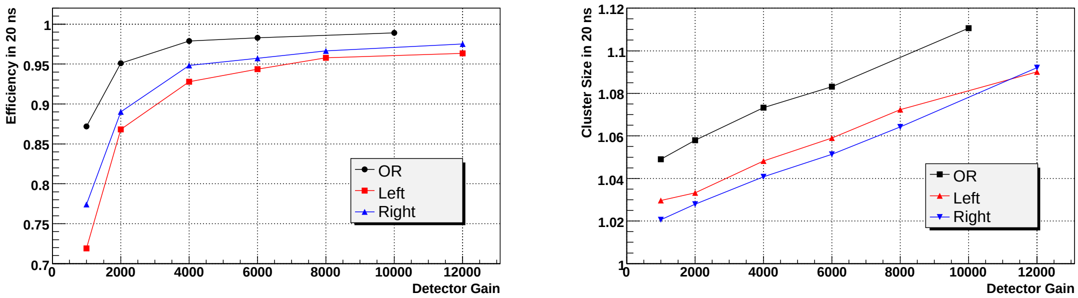

Figure 6.66: Efficiency and cluster size in a 20 ns window vs. gain for a chamber composed of two triple-GEM detectors. The curves show the data for the single detectors and for the OR of the two.

has moved from a detector gain of 6000 to 4000. This allows to operate the chambers with an integrated charge decreased by 30% and in safer conditions with respect to discharges.